Semiconducting Two-Dimensional Nanomaterials for Optoelectronic Devices

Sangyeon Pak

St Hugh’s College

University of Oxford

A thesis submitted in fulfilment of the requirements for the degree of
Doctor of Philosophy in Engineering Science

Trinity Term 2018

Semiconducting Two-Dimensional Nanomaterials for Optoelectronic Devices

Sangyeon Pak, St Hugh's College, University of Oxford

Abstract

The emergence of transition metal dichalcogenides (TMDCs) monolayers which exhibit a variety of structural and electronic configurations has attracted significant attention as the monolayers have been found to possess unique characteristics that are not observed in their bulk forms. These materials have sufficiently wide electronic bandgaps (E_g = 1~2 eV) with a direct band gap nature, which makes them suitable for electronic and optoelectronic applications. Their atomically-thin configuration coupled with the presence of covalent bonds between the transition metal atoms and the chalcogenide atoms ensure that the materials are highly flexible and transparent. As a result, TMDC monolayers have potential in applications such as flexible and transparent optoelectronic devices.

In this thesis, TMDC monolayers are studied ranging from the synthesis of these materials to their implementation in optoelectronic device applications. The aim of this research is to enhance our understanding of the electronic and optoelectronic behaviour of these layers and to demonstrate the feasibility of using TMDC monolayers in next-generation device applications. The initial goal is to synthesise large-sized single crystals using chemical vapour deposition, where the nucleation density can be controlled through solution-processing and the loading of an extremely small amount (0.01 mg) of transition metal oxide precursors. It is shown that the nucleation density can be dramatically decreased so that large grain sizes up to 500 μm can be obtained in the TMDC monolayer film. Using this approach, the synthesis of MoS_2/WS_2 heterostructures is shown to be possible using a one-step process, which results in a clean interface without much mixing of the precursors.

Following a discussion of the synthesis process, my DPhil thesis then focuses on chemical doping of the surface of the monolayers and the role of strain engineering on the tuning of the physical, optical, and electrical properties of the TMDC monolayers. It was found that the carrier density of an MoS_2 monolayer could be modulated and that properties such as the photoresponsivity, detectivity, and photoresponse time can be controlled through changes to the energy band structure. Also, strain engineering of TMDC monolayers and hetero-bilayers is successfully demonstrated. The excitonic behaviour of an MoS_2/WS_2 hetero-bilayer, when subjected to a small mechanical strain (up to 0.7 %), is experimentally observed for the first time, and the effect of interlayer coupling on the wavelength of the photoluminescence peak as well as changes in the photoluminescence intensity are demonstrated.

Lastly, the thesis considers specific optoelectronic applications of TMDC monolayers. These optoelectronics applications include: a (1) 2D/QD vertical heterojunction phototransistor with an enhanced photoresponse time of 950 μs and photoresponsivity of 6120 A/W and a (2) two-terminal MoS_2 flexible photodetector with surface functionalisation that decreases the response time to 0.7 s. The results and performance of the materials and devices presented in this thesis show particular promise for next-generation, flexible and transparent device applications.

Acknowledgements

The DPhil research project would not have been accomplished without the guidance, support and advice of my supervisors, colleagues, families and friends. I would like to thank my supervisors and advisors, Prof. Stephen M. Morris, Prof. Jung Inn Sohn, Prof. SeungNam Cha, and Prof. Jong Min Kim, for their unwavering patience, guidance and support. I really appreciate the chance my supervisors gave me to become a student at the University of Oxford and appreciate the opportunity to work under their invaluable guidance throughout my DPhil. I am immensely grateful to their sincere efforts to guide and encourage me to step forward in research and motivate me to make my DPhil experience productive.

I would also like to thank the following people in Oxford:

Juwon Lee, who carried research with me in the field of 2D materials, for his considerate support and helpful discussion that have been immensely useful for my research throughout the DPhil project.

Yuljae Cho, John Hong, and Paul Giraud, who were DPhil students during my DPhil studies, for being the best and congenial colleagues.

Dr. Sanghyo Lee, Dr. Geon-Hyoung An, and Dr. Bo Hou, who are current postdocs, for their sincere support and advice for my research.

Dr. Young-Woo Lee, Dr. A-Rang Jang, Dr. Byung-Sung Kim, Dr. Jong Bae Park, and Dr. Dae-Hwan Jung, who are previous postdocs, for their meaningful discussions and advices.

Prof. Hansu Kim, Dr. Yong-Hae Kim, and Prof. Tae-Lim Choi, who were academic visitors, for their time spending with me and giving advice.

Dr. Jongchul Lim, Dr. Sungho Nam, Prof. Jae Eun Jang, Prof. Hyeon Suk Shin, and Prof. Hyunsik Im for their help with material analysis and device-related work.

Furthermore, I kindly acknowledge the European Research Council for the financial support of my DPhil study and the Department of Engineering Science and St Hugh’s College at the University of Oxford for their continuous support.

Most importantly and lastly, I would like to express my deepest gratitude to my parents, Daewon Pak and Hongeun Kim, as well as my brother, Daniel Sangwoo Pak, for their love and moral support.

Table of Contents

List of Figures

List of Tables

Chapter 1. Introduction

1.1. Context and motivation

In their bulk form, a plethora of van der Waals layered materials have been studied and utilized for a very long time.[1] For instance, graphite has been widely used as a dry lubricant by virtue of its layered nature, which is attributed to a combination of tightly bound in-plane bonds and weak van der Waals interactions in the out-of-plane direction.[2] In 2004, scientists at the University of Manchester (UK) were able to isolate a monolayer of graphene from graphite for the first time by a mechanical exfoliation process involving scotch tape.[3] This remarkable breakthrough was the beginning of a new class of materials, which were two-dimensional (2D) in nature, where individual layers are only one, two or three atoms thick.

2D materials are typically less than a nanometre-thick; however, despite being so thin they are very strong and are generally held together with strong covalent bonds in the form of atomic planes. Graphene exhibits many extraordinary and unique properties not found in its bulk counterpart. To list a few, these include high transparency (> 97 % in visible spectrum), robustness against mechanical stresses, and extremely high carrier mobility up to 200,000 $cm^2V^{-1}s^{-1}$.[4, 5] These properties in turn have enabled the development of layered materials with a wide range of physical, electrical and optical properties for creating novel devices, particularly for next-generation flexible and wearable electronics/optoelectronics applications. However, as graphene does not exhibit an electronic band gap naturally, there are fundamental limitations in terms of realizing high on/off ratios of the channel current for switching devices and highly sensitive and wavelength selective photon detection.

In this regard, transition metal dichalcogenide (TMDC) monolayers have garnered considerable interest from the scientific community as TMDCs are semiconductors with a sufficiently wide electronic bandgap (E_g = 1~2 eV for 2D TMDCs), which makes them highly suitable for electronic and optoelectronic applications.[1] As depicted in Figure 1-1, these materials form layered structures in the form of X-M-X, where metal atoms (M) are sandwiched between two layers of chalcogen atoms (X). Similar to graphene, the intralayer M-X bonds in TMDCs are strong covalently bonded in nature, whereas weak van der Waals forces couple each layer together. Also, they can be assembled vertically or laterally so that distinct 2D monolayers can be integrated into van der Waals heterostructures with structurally abrupt heterojunction interfaces for high performance and high-speed devices.

TMDC monolayers offer fundamental advantages in terms of their optoelectronic applications: this includes (1) tuneable bandgap, (2) strong light-matter interaction, even when scaled down to atomically thin layers or those that are a few nanometre in size, (3) facile methods to tune their electrical properties owing to their high surface-to-volume ratio, (4) better flexibility and transparency compared to their bulk counterparts, and (5) the possibility of scaling down the devices as well as the integration with various substrates. A number of these two-dimensional semiconducting materials as well as their heterostructures offer various opportunities for boosting light-matter interaction and provide a platform for further scientific discoveries as well as promising technologies for nanoscale optoelectronics devices across an extensively wide range of the electromagnetic spectrum.

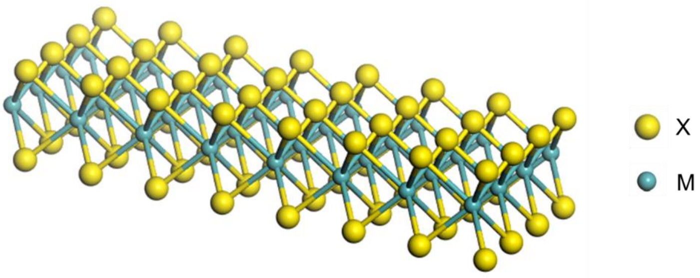

Figure 1-1. Atomic structure of TMDC monolayers in the form of MX_2

The main objectives of the work in this thesis are as follows:

i. To synthesize and characterize high-quality, single crystalline TMDC monolayers and their heterostructures in order to study their properties and their integration in optoelectronic devices;

ii. To investigate the fundamental physical properties of TMDC monolayers and to control their physical, optical, and electrical properties via stress-strain engineering and surface chemical doping;

iii. To develop various optoelectronic devices utilizing TMDC monolayers and investigate their optoelectronic performance;

iv. To explore different device design strategies so as to boost their optoelectronic performance.

1.2. Layout of the thesis

This thesis begins with a literature review, which summarizes the current conventional wisdom regarding the structures, properties, and recent device applications involving TMDC monolayers (Chapter 2). This information was used as the cornerstone for my research. Subsequently, the basic experimental techniques employed in this work including the chemical vapour deposition (CVD) synthesis system, device fabrication and TMDC characterization are introduced in Chapter 3. Details of the experimental and theoretical methods that have been used by my collaborators are not included in this chapter and they can be found in the corresponding published papers.

My experiments start with the synthesis of TMDC monolayers and heterostructures using atmospheric pressure CVD (APCVD) on SiO_2/Si substrates in Chapter 4, followed by the corresponding experimental results and the development of novel growth techniques. The work presented in this chapter has been published as an article in *Advanced Materials* 2017, **29**, 1702206. The synthesized TMDC monolayers and heterostructures synthesized in Chapter 4 are then used in the experiments and studies presented in Chapters 5,6, and 7. Chapter 5 demonstrates surface functionalisation of an MoS_2 monolayer to modulate the carrier densities through either n or p-doping, including the characterization of the electrical and photoresponse behaviour of n-doped and p-doped MoS_2 monolayers. Chapter 6 then considers the effects of strain on the properties of TMDC crystals. The modulation of their optical and vibrational properties is demonstrated experimentally. The work in this chapter has been published in *Nano Letters* 2017, **17**, 5634-5640.

Based on the understandings gained in the previous Chapters, potential optoelectronic device applications of an MoS_2 monolayer are then studied in detail in Chapter 7. New device strategies for enhancing the performance of the MoS_2 phototransistor are introduced including the development of MoS_2/QD phototransistors and a MoS_2 flexible photodetector. The work in this chapter has been published in *ACS Applied Materials & Interfaces* 2018, **10**, 38264-38271. The final chapter summarizes the key research findings and achievements for each Chapter and considers future opportunities and challenges for optoelectronic devices based on TMDC crystals.

Chapter 2. Background

2.1. Introduction to TMDC monolayers

Two-dimensional transition metal dichalcogenides (TMDCs) are an emerging class of materials that possess properties that are highly attractive for various fundamental scientific studies. This is because they exhibit unique properties that are not shown in their bulk forms, and they are particularly attractive for electronics and optoelectronics applications at the nanoscale. For the past few years, there has been considerable interest in these materials, as can be seen from the exponentially increasing number of publications, which have been triggered largely by the demonstration of a high-mobility transistor utilizing a monolayer MoS_2 channel[6] as well as the discovery of strong photoluminescence[7] in an MoS_2 monolayer. These remarkable features are due, in part, to the transition from an indirect to direct band gap on downsizing from the bulk to monolayer form.

TMDCs cover a diverse catalogue of chemical formulas. Specifically, TMDCs are materials that are classified by the general chemical formula, MX_2, where M represents a transition metal atom from groups 4-7 and 8-10, and X is a chalcogen (S, Se or Te), as shown in Figure 2-1.[8] Group 4-7 TMDCs are predominantly layered structures, whereas group 8-10 TMDCs are usually non-layered in terms of their architecture. These group 4-7 TMDC materials form layered structures in the form of X-M-X, where metal atoms are sandwiched between two layers of chalcogen atoms.

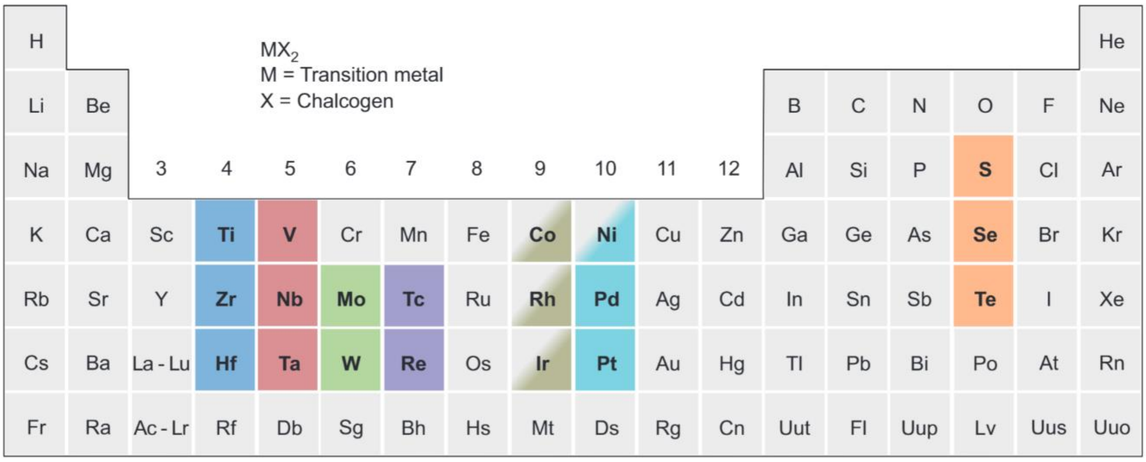

Figure 2-1. The periodic table showing the broad range chemistry of TMDC materials. Figure reprinted (adapted) with permission from ref[8]. Copyright 2013 Springer Nature Limited.

TMDCs also exhibit a rich variety of electronic properties ranging from insulators such as HfS_2, semiconductors such as MoS_2 and WS_2, to semi-metallic and metallics such as WTe_2 and NbS_2.[8] The richness in the electronic properties also implies that they have wide selection in terms of the band gap energy, which is particularly beneficial for wavelength selective photodetection and other optoelectronic devices. The band gap energies of TMDC monolayers are depicted in Figure 2-2.[9] TMDC monolayers show attractive features when they exist in a monolayer form. Their physical and chemical properties dramatically change when scaled down from bulk to monolayer form owing to the change in interlayer coupling and the degree of quantum confinement. The band structure of semiconducting TMDCs, for example, transforms from an indirect to a direct band gap when decreasing the thickness from bulk to single layer. Photodetectors fabricated from these direct bandgap monolayer show a high photoresponsivity that can be more than 10^3 A/W.[10] Similarly, field-effect transistors made from TMDC monolayers also show high room temperature mobility with a high on/off current ratio, by allowing a large degree of electrostatic control over the electrical conductivity, which arises from the atomic thickness that is smaller than the screening length.[11]

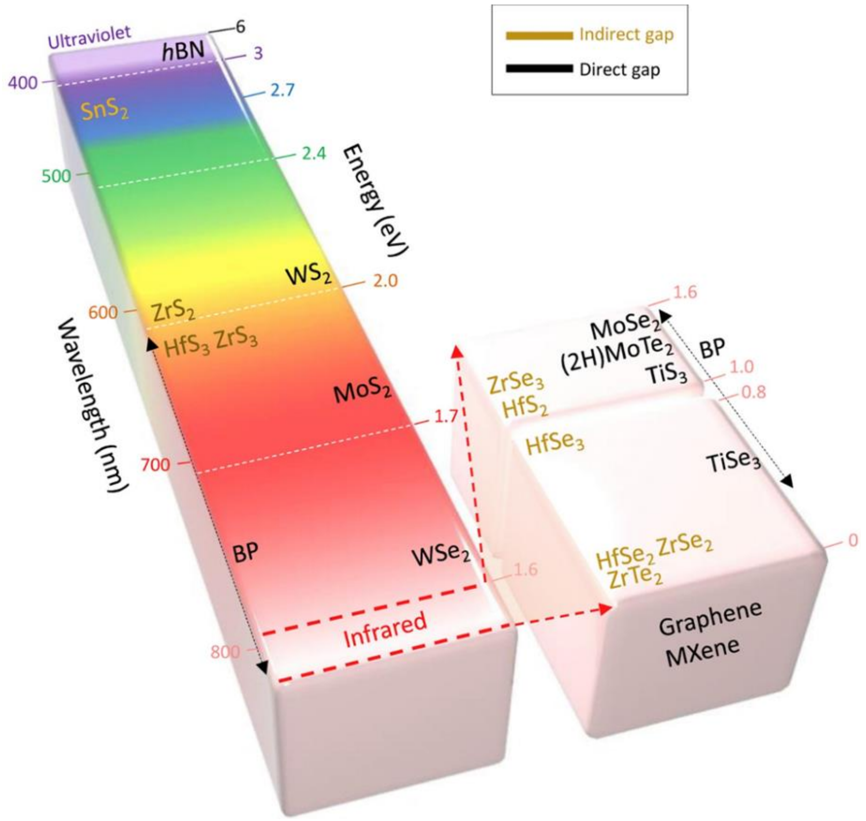

Figure 2-2. The bandgap of 2D TMDC materialsvarying from zero bandgap to a wide electronic bandgap. Figure reprinted (adapted) with permission from ref[9]. Copyright 2016 Elsevier Ltd.

The change in the physical and chemical properties of TMDC monolayers stems from the degree of quantum confinement in that parameters thought to be constant in bulk semiconductors are instead dependent on the dimensions of the material.[12] 2D materials confine the electron motion in two-dimension as the thickness of the material becomes extremely small, meaning that the carriers are placed in the infinitely high potential wells. Generally, quantum confinement is approximated by using a particle-in–a-box model and by solving the time-independent Schrodinger's equation. The confinement leads to a change in the Density of States (ρ) within the bands as the number of charge carriers is given by $N_{2D} = \frac{2\pi k^2}{(2\pi)^2}$ rather than $N_{3D} = \frac{8\pi k^3}{3(2\pi)^2}$, which is the case for 3-dimensional materials. In these expressions, $k = \left(\frac{2mE}{\hbar^2}\right)^{\frac{1}{2}}$. For 2D materials then density of states then becomes[12]

$$\rho_{3D}(E) = \frac{1}{2\pi^2}\left(\frac{2m^*}{\hbar^2}\right)^{\frac{3}{2}} E^{\frac{1}{2}} \rightarrow \rho_{2D}(E) = \sum_{i=1}^{n} \frac{m^*}{\pi\hbar^2} H(E - E_i) \qquad (2.1)$$

where H is the Heaviside step function. The density of states for electron motion in the plane of the 2D layer turns out to be constant with energy, and the density of states for a given subband is a "step". The confinement also leads to a change in the bandgap and the band-edge position, whilst the density of states affects the electronic states and optical properties of TMDC monolayers, which is discussed in Section 2.5.

The plethora of low-dimensional semiconducting TMDC materials provides opportunities for new scientific discoveries and the development of new technologies when either two different TMDC monolayers are combined to create a van der Waals heterostructure or alternatively materials having different dimensions are combined to form hybrid structures.[13, 14] Two-dimensional TMDCs are ideal for forming heterostructures as they do not consist of dangling bonds, which implies that they can be easily integrated with any material, providing a clean interface. The investigation of this new type of heterostructure is becoming a particularly attractive research area due to the many interesting phenomena that appear to occur at the heterostructure interface such as ultrafast transfer of charge[15-17], as well as their integration in next-generation electronics and optoelectronics devices with high performance, high speed, and high power performance.[18]

The purpose of this chapter is to introduce and review of these structures, their properties, and potential device applications of TMDC monolayers, with a particular focus on MoS_2 monolayers.

2.2. Crystal structure of TMDC monolayers

Bulk TMDCs exhibit a layered structure. In the layered structure, each layer has a thickness of 6~8Å with a hexagonally packed layer of metal atoms that are covalently bonded to two layers of chalcogen atoms.[8] The layers are coupled by weak out-of-plane van der Waals forces, allowing the layers to be easily detached along the layer surface and the surface of the layer is therefore free of dangling bonds.[19-21]

In their bulk form, it is reported that TMDC can arrange in to three different types of layered crystal structure; these are the octahedral structure (1T phase) and trigonal prismatic structures (2H and 3R phases) as presented in Figure 2-3.[22, 23] The 2H and 3R phases are more energetically favourable than the 1T phase, and thus more frequently observed in nature or found as chemical synthetic products. The 2H and 3R phases have the same intralayer coordination configuration; however, they have a different stacking sequence (AbA BaB for 2H phase and AbA CaC BcB for 3R phase) associated with an interlayer coupling. The two different stacking sequences can be distinguished by looking at the atoms from the top, where two layers are fully eclipsed by Mo (S) atoms sitting on S (Mo) atoms in the 2H phase, while the S atoms in the middle layer sit under the hollow of the hexagonal centre of the top layer in the 3R phase. In the monolayer form of TMDC, only two types of polymorphs are found and these are the trigonal prismatic and octahedral phases, which can be distinguished using high-resolution scanning transmission electron microscopy.[24]

The crystal structures of TMDCs show different properties: for example, the 1T phase of TMDC compounds exhibit metallic-like properties whereas the 2H and 3R types are semiconductors. Depending on the application, the crystal structure of TMDC compounds can be appropriately utilized. Practically, several groups have succeeded in transforming 2H-MoS_2 into 1T-MoS_2 by intercalation with alkali metal ions and electron beam irradiation to trigger a phase transition, which destabilized the original 2H phase.[25-27] From the point of view of electronic and optoelectronics applications, the 2H and 3R phase are much more interesting and can be easily implemented as they are semiconductors with stable crystal structures. Therefore, to date, the 2H and 3R phase have dominated the research studies in the area of TMDCs.

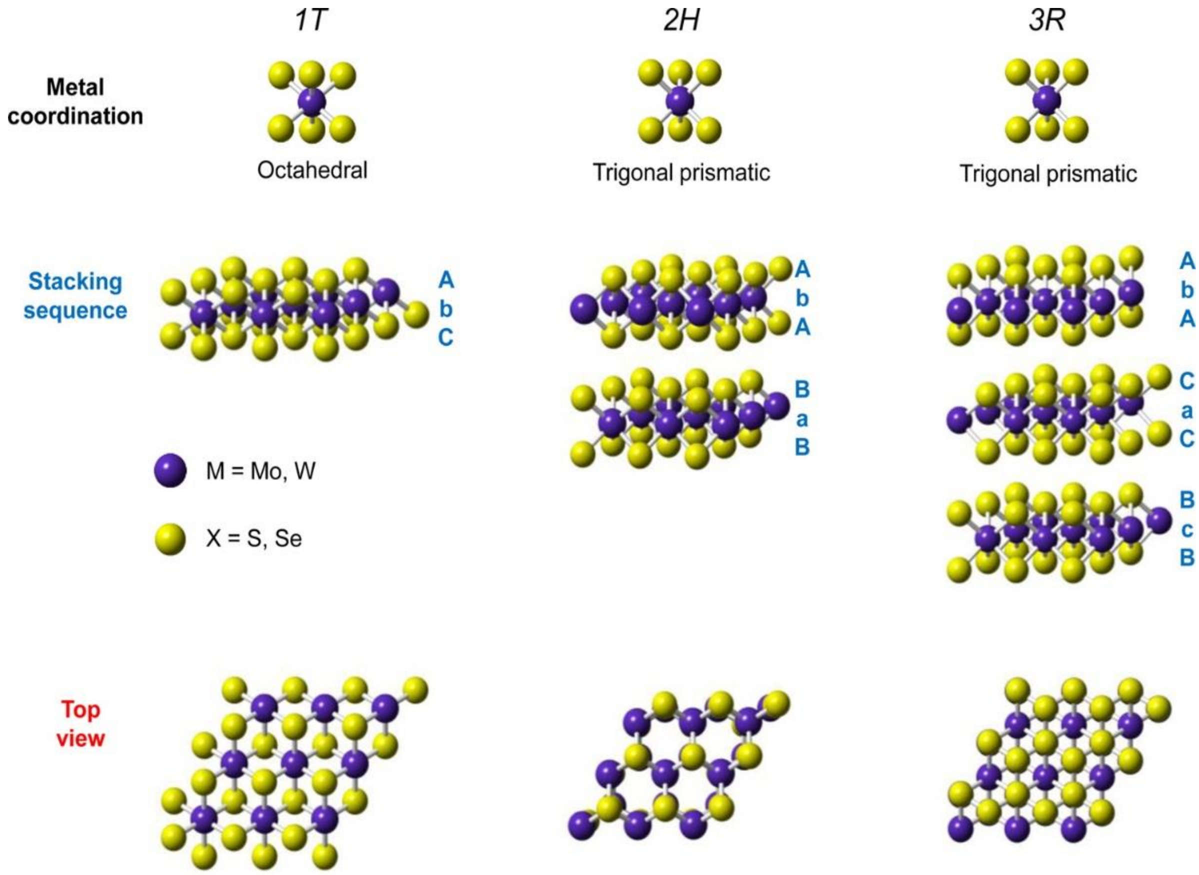

Figure 2-3. Different crystal structures and stacking sequencesof TMDC structural unit cells. Figure reprinted (adapted) with permission from ref[22]. Copyright 2015 American Chemical Society.

2.3. Vibrational properties of TMDC monolayers

The vibrational properties of TMDC materials can be easily detected using Raman spectroscopy, which is a spectroscopic technique that is used to observe the vibrational modes based upon the interaction of laser light and phonons. In this case, the energy of the incident laser photons is shifted either up or down. When monochromatic light illuminates a TMDC sample, the majority of the light is elastically scattered, which has the same energy as the excitation light source, and the elastic scattered radiation (Rayleigh scattering) is then filtered out. However, there is a small proportion of the light that is inelastically scattered (Raman scattering), which originates from the interactions between the vibrational energy levels of the TMDC sample and the incident electromagnetic waves. As a result of this interaction, there is a shift in the energy of the inelastically scattered light and this gives rise to the so-called Raman spectrum, which can be used to identify and quantify TMDC materials.

Raman spectroscopy can be particularly useful in providing information about changes in the van der Waals interactions, the doping level, and the strain present in the lattice of a TMDC material. This is because the vibrational modes of the constituent atoms are easily affected by such changes[28-30] and are usually observed through the changes in the frequency and intensity of the Raman vibrational modes of the TMDC materials. It is known that there are two distinct high-frequency Raman active vibrational modes for MoS_2, which are the E^1_{2g} and A_{1g} modes (Figure 2-4a).[31] The E^1_{2g} mode originates from the in-plane vibration of two S atoms in opposite directions with respect to the Mo atom that is placed in between the S atoms, whereas the A_{1g} mode is related to the out-of-plane vibration of the S atoms in the opposite directions while surrounding the Mo atom. As a result, the two vibrational modes are significantly influenced by their surroundings and the layer thickness of MoS_2. In general, both the E^1_{2g} and A_{1g} modes are expected to stiffen as the number of layers increases because the interlayer van der Waals interactions increase with the number of layers, inducing stronger restoring force between the atoms.[29, 31, 32] However, as seen in Figures 2-4a,b, experimental results demonstrate that while the A_{1g}

mode is stiffened (blue-shifted) with an increase in the number of layers, the E^1_{2g} mode is softened (red-shifted).[31]

The anomalous behaviour of the E^1_{2g} mode with respective to the number of layers is believed to be due to stacking induced changes in the intralayer bonding and/or Coulombic interlayer interactions that become stronger as the number of layers increases. As a result, this anomalous behaviour means that the difference in the Raman frequencies between the two modes can be used to identify the number of layers. For example, for a MoS_2 monolayer, the frequency difference is experimentally determined to be 19 cm^{-1}, while a difference of 21 cm^{-1} is observed for a bilayer, which increases to 25 cm^{-1} for bulk MoS_2 (Figure 2-4c).[28, 31-33] Consequently, Raman spectroscopy has become the most powerful tool to detect the number of layers in TMDC materials, although the thickness can be directly obtained using atomic force microscopy (AFM).

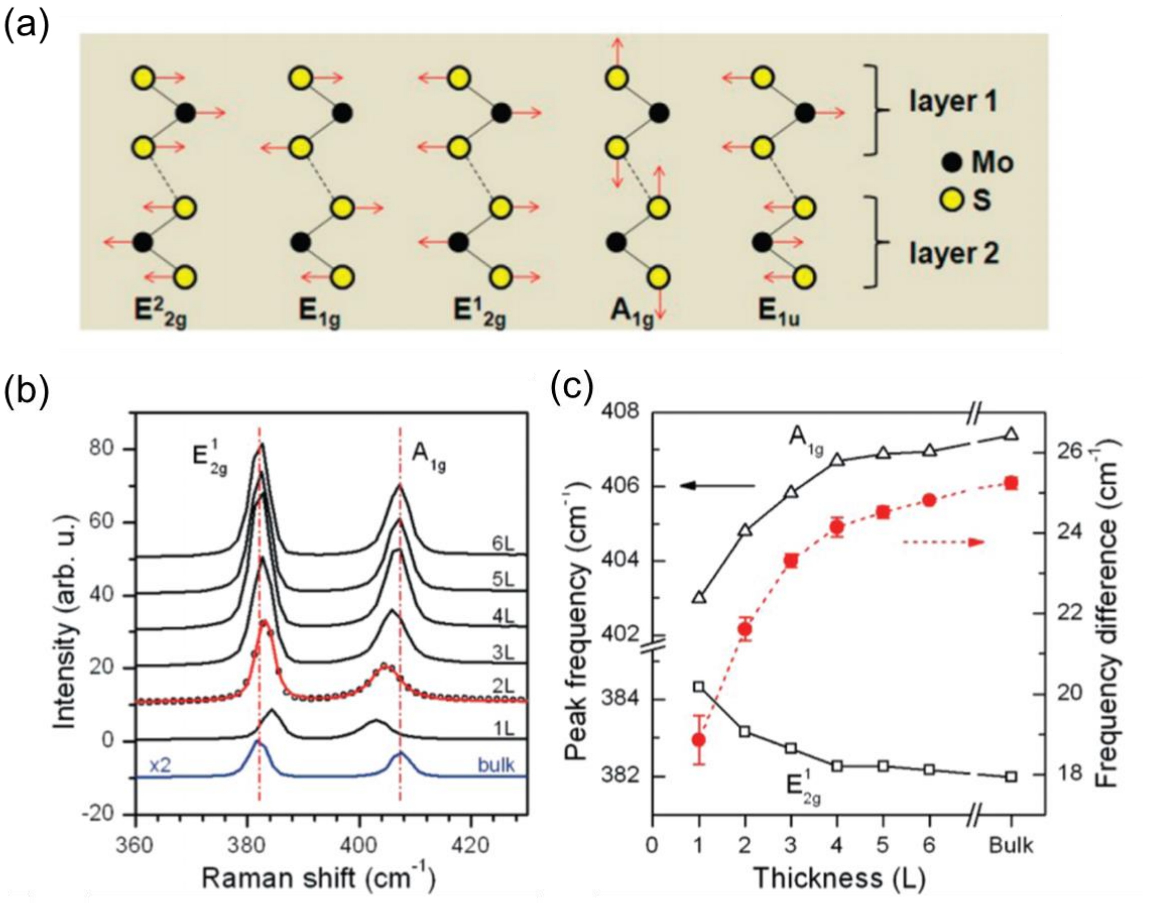

Figure 2-4. Raman active vibrational modes of MoS_2. a) Illustration of the four Raman-active modes and the one IR-active mode (E_{1u}) of MoS_2. b,c) Changes in the E^1_{2g} and A_{1g} modes as a function of the number of layers of MoS_2. Figure reprinted (adapted) with permission from ref[31]. Copyright 2010 American Chemical Society.

2.4. Electronic band structure of TMDC monolayers

An understanding of the electronic band structure is highly important for TMDC monolayers as they show a thickness-dependent evolution in the electronic band structure as well as various phenomena associated with the optical and electrical processes that are important for realizing electronic and optoelectronic devices.

The fundamental band structure of bulk 2H is theoretically calculated using density functional theory as shown in Figure 2-5.[7] It shows that for bulk MoS_2, the conduction band minimum (CBM) is located midway between the Γ and K point, while the valence band maximum (VBM) is positioned at the Γ point, possessing indirect band gap characteristics with a band gap of ~ 1.2 eV.[34] However, according to theoretical calculations, a change in the electronic band structure is predicted when bulk MoS_2 is thinned down to a single monolayer. The DOS at the VBM at the Γ point and at the CBM at the K point is largely determined by the $4d_z{}^2$ orbitals of the Mo atom,[35] and as the number of layers increases, the $4d_z{}^2$ orbitals have a stronger interaction between the layers, leading to a change in the energy states. While the local CBM and VBM at the K point (direct band gap) remain unchanged, the CBM at the midway between the Γ and K points and the VBM at the Γ point gradually shift upwards and downwards, respectively, as the thickness decreases to a monolayer, and the local CBM and VBM at the K point result in a direct band gap of ~ 1.9 eV in the MoS_2 monolayer. As seen in Figure 2-5, there is a transition from an indirect band gap (bilayer) to a direct bandgap (monolayer) on decreasing the number of layers; this is implied by the upshift(downshift) of the energy level of Γ_{VB} and ΓK_{CB}, and therefore, the $K_{VB\text{-}CB}$ point becomes the smallest bandgap. A similar indirect-to-direct band gap transition is also observed in other TMDC materials such as $MoSe_2$, WS_2 and WSe_2 when the number of layers decreases to a monolayer.[36-38] Such an indirect-to-direct bandgap transition is associated with quantum confinement effects that become dominant when the thickness becomes significantly small. Also, the changes in coulombic interlayer interaction and orbital hybridisation between the p_z orbitals of the sulphur atoms and the d-orbitals of the Mo atoms are known to be responsible for the transition.[39]

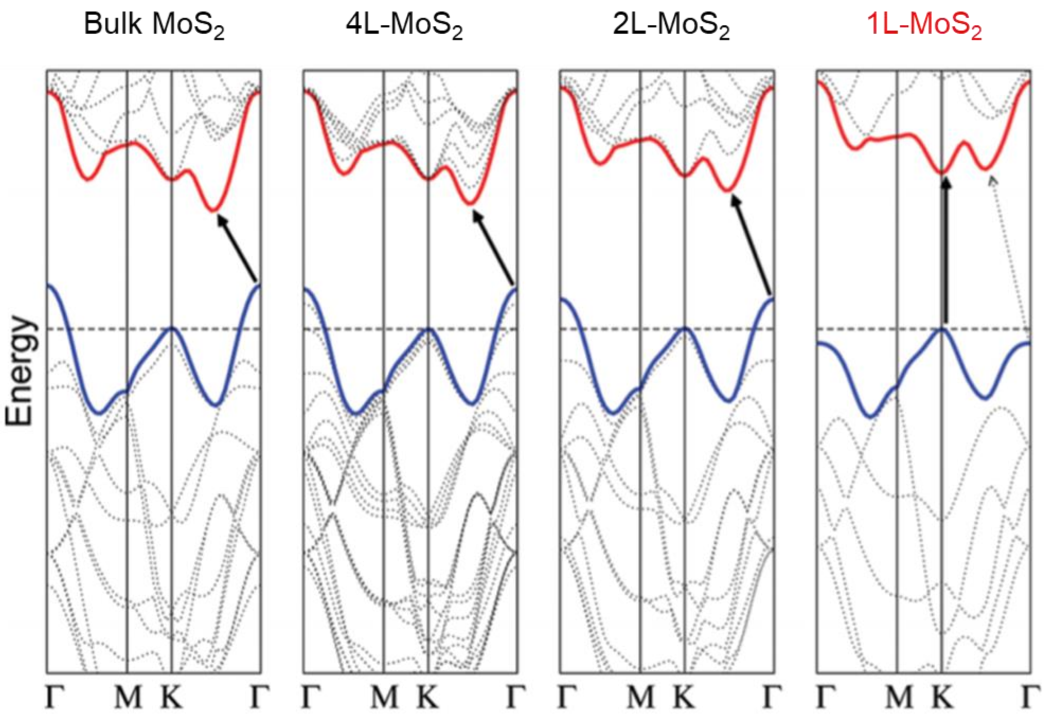

Figure 2-5. Calculated electronic band structure of MoS_2 from bulk to monolayer form.The transition from an indirect to direct band gap is found to occur at the K point when the MoS_2 is thinned down to a single monolayer. Figure reprinted (adapted) with permission from ref[7]. Copyright 2010 American Chemical Society.

The direct band gap nature observed in TMDC monolayers is accompanied by the emergence of strong photoluminescence (PL) emission corresponding to the direct optical band gap energy. For the case of MoS_2, PL of significant intensity is only observed when in monolayer form, while very low PL emission is observed for MoS_2 consisting of layers of 2 or more as shown in Figure 2-6.[40] Also, for MoS_2 with layers of 2 or more, very weak indirect band gap emission can be observed having different indirect gap energies, confirming the thickness dependent evolution of the CBM and VBM at the Γ-K point and K point, respectively. It is worth noting that the emission energy measured using PL spectroscopy corresponds to the optical bandgap, which is the difference between the fundamental band gap energy and the binding energy of the excitons. It is known that the binding energy of excitons is 0.1 eV in the bulk and increases to 1.1 eV in the monolayer, and it is the higher binding energy in the monolayer form that is responsible for the strong PL intensity.[41] Due to the large binding energy, excitons remain stable even at room temperature, exhibiting high measured PL intensities.[42, 43] The PL quantum yield of MoS_2 monolayer is therefore found to be $>10^4$ greater than the quantum yield of its bulk counterpart as shown in the inset of Figure 2-6a.

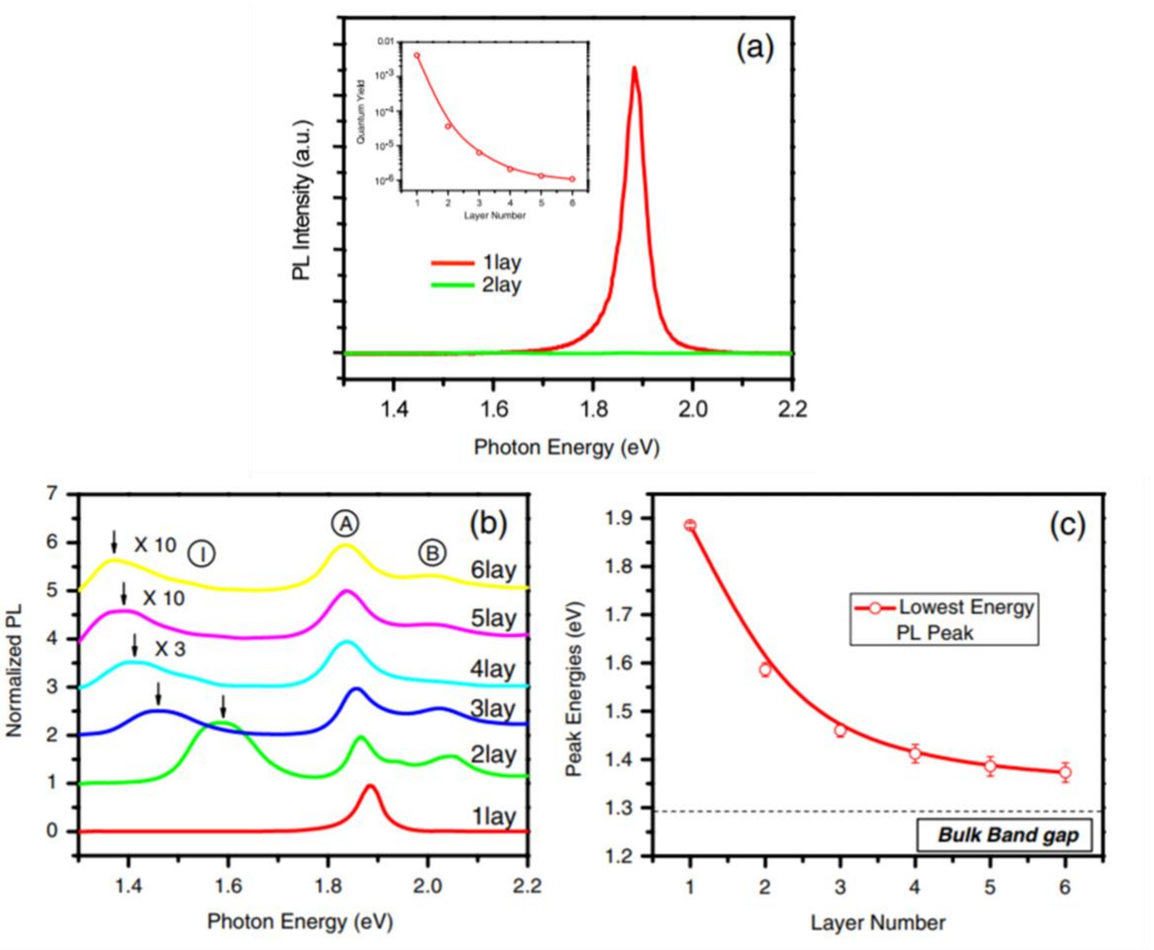

Figure 2-6. Layer thickness-dependent PL of MoS_2. a) PL spectrum taken from monolayer and bilayer MoS_2. There is an emergence of strong PL emission from a MoS_2 monolayer, confirming the transition from indirect to direct optical band-gap in the monolayer. b) Normalized PL spectrum of MoS_2 with varying layer thickness. c) Peak energy in the PL with respect to the number of layers. Figure reprinted (adapted) from ref[40]. Copyright 2010 American Physical Society.

The PL intensity, as well as its wavelength corresponding to the peak PL intensity that is observed for a MoS_2 monolayer, appears to vary across the literature.[44-46] This is because the PL profile of TMDC monolayers is easily affected by the surrounding environment such as the underlying substrates and whether there are any adsorbed gas molecules on the surface of the TMDC crystals, which has a high surface-to-volume ratio. In this sense, the surrounding environment significantly affects the PL emission characteristics through doping/strain.[44, 45, 47, 48] Depending on the doping level, the relative intensity between the negatively charged excitons (trions) and the neutral excitons changes. Because the peak associated with the trions is located at a lower energy than that of the excitons, the doping concentration in MoS_2 can significantly influence the emission peak wavelength and intensity. Besides doping concentration in MoS_2, the lattice strain imparted on the TMDC crystal during high temperature CVD synthesis can also significantly affect the PL properties of TMDC monolayers.[49] Therefore, depending on the growth conditions or the sample preparation method (e.g. exfoliation or CVD), the lattice strain can be different, and the bandgap can be varied with the amount of strain present in the atomic crystals, as seen in Figure 2-7c.

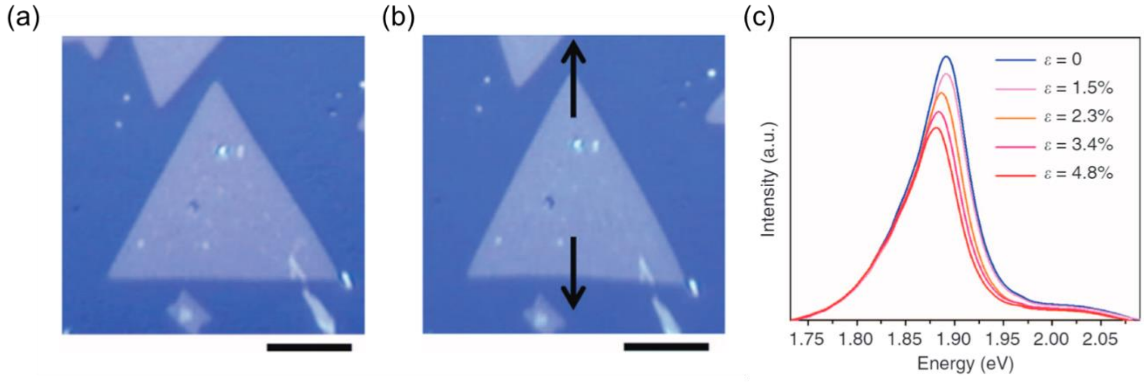

Figure 2-7. PL emission of a MoS_2 monolayer with respect to a tensile strain. Optical images of MoS_2 monolayer under a) no strain and b) tensile strain. Scale bar: 6 μm. c) Change in the PL emission wavelength and intensity of a MoS_2 monolayer with respect to the application of a tensile strain. Figure reproduced (adapted) with permission from ref[49]. Copyright 2014 Springer Nature Limited.

2.5. Device applications of TMDC monolayers

Investigations on the electronic properties of bulk TMDC materials has been carried out over many decades.[50] However, the research field has not received much attention until very recently when graphene layers were successfully isolated in 2004.[3] With sizable band gaps, high in-plane mobility, high thermal stabilities, lack of dangling bonds, and high mechanical stability make these materials particularly suitable for transistor and photodetector applications.

2.5.1. Field-effect transistors

One of the most important applications of semiconductors is transistors in digital logic circuits. The first demonstration that showed the potential of a single-layered MoS_2 transistor was reported in 2011, where Radisavljevic *et al.* showed n-type conduction, high field-effect mobility of at least 200 $cm^2V^{-1}s^{-1}$, and a room-temperature current on/off ratio exceeding 10^8 as shown in Figure 2-8.[6] The device consisted of a top gate with a 30 nm of HfO_2 layer that acts as the high-*k* dielectric and passivation layer, leading to a low subthreshold swing (SS) of 74 mV/decade owing to the mobility improvement. These findings suggested that semiconducting TMDC monolayers can be used as an electronic switch in digital integrated circuits, utilizing a gate potential to control the conductivity of the semiconducting channel material. Ideally, the Metal-oxide-semiconductor FETs (MOSFETs) switch would have zero current flowing through the channel material in the OFF state and no resistance in the ON state, with the capability of instant transition between the OFF/ON states. It has been theoretically predicted that monolayer MoS_2 transistors can reach significant on/off ratios of 10^{10} due to the large band gap and abrupt switching (SS~ 60 mV/decade).[51, 52] Therefore, monolayer MoS_2 transistors can be attractive for future low power applications as well as low cost electronic applications, given that monolayer MoS_2 has a high thermal stability, transparency, flexibility, and is relatively inexpensive.[51]

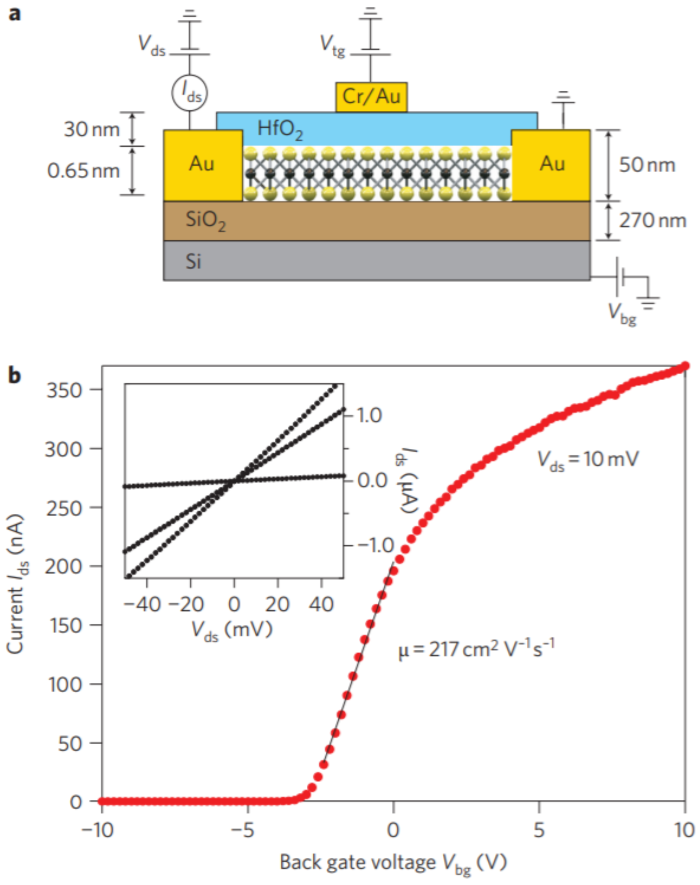

Figure 2-8. A single-layer MoS_2 transistor. a) The device schematic and b) transfer curve measured from the device. The inset of b) shows the output curve of I_{ds} as a function of V_{ds} acquired for V_{bg} values of 0, 1, and 5 V. Figure reproduced (adapted) with permission from ref[6]. Copyright 2011 Springer Nature Limited.

In addition to engineering the mobility by employing a high-k dielectric layer, the contact resistance can also further improve the mobility of TMDC FETs.[53-58] Schottky barriers can exist at the metal-semiconductor interface at the source and drain electrodes and can adversely impact the carrier transport in the TMDC materials, limiting their field-effect mobilities from reaching the intrinsic mobility. For this, Das *et al*. systematically studied different metal contacts on multilayer MoS_2 FETs. As shown in Figure 2-9, four different metals were employed as source-drain contacts for this study. These include high work function metals including nickel (Φ_{Ni}=5.0 eV) and platinum (Φ_{pt}=5.9 eV) and low work function metals including titanium (Φ_{Ti}=4.3 eV) and scandium (Φ_{Sc}=3.5 eV). While some p-type conduction was expected initially for the high work function metals, all four contacts exhibited n-type FET characteristics, suggesting a pinning at the interface. The Schottky barrier heights extracted from the temperature-dependent *I-V* transfer characteristics and the Richardson's plot (extracting slope from the linear region) were 30, 50, 150, and 230 meV and the field effect mobility values of 184, 125, 36, and 21 $cm^2V^{-1}s^{-1}$ were measured for Sc, Ti, Ni, and Pt, respectively. Also, the field effect mobility from a Sc-contacted FETs reached the highest value of 700 $cm^2V^{-1}s^{-1}$ when further high-k dielectrics were employed. These results suggest that the contact resistance is important for achieving high mobility in TMDC materials.

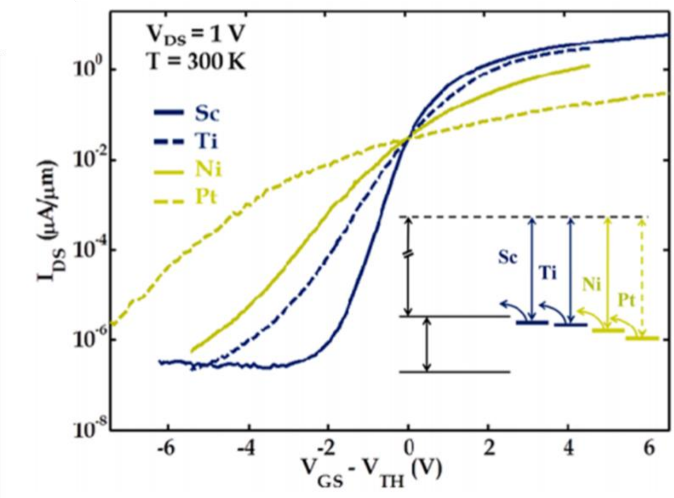

Figure 2-9. Transfer curves of multi-layered MoS_2 with different metal contacts. Figure reproduced (adapted) with permission from ref[54]. Copyright 2013 American Chemical Society.

As a result of the extremely high surface-to-volume ratio, the FETs made from TMDC monolayers generally show a large hysteresis. This is because TMDCs are very sensitive to external influences introduced by the bottom and top interfaces. At the bottom interface between the TMDCs and the substrates, roughness and/or functional groups can play a significant role in determining the carrier transport as well as the charge transfer doping. To mitigate the effects of the bottom interface, Withers *et al*. have demonstrated an improvement using an hexagonal boron nitride (h-BN) layer that prevents extrinsic factors such as charge traps in the SiO_2 layer.[59] The charge traps in the oxide dielectrics are known to cause hysteresis in the TMDC FETs and small values of the charge carrier mobility.[60-62]

The top interface can also affect carrier transport in TMDC FETs. When measured under ambient condition, absorbed H_2O and O_2 molecules are known to withdraw electrons from the channel and lower the carrier density. As shown in Figures 2-10c,d, the hysteresis in the transistor can be minimized under vacuum or can be maximized when the humidity in air is increased.[63] Because the adsorbed molecules generally act as p-doping molecules, passivating the top surface with dielectric layers can increase the mobility and decrease the hysteresis in the measurements.[60, 61]

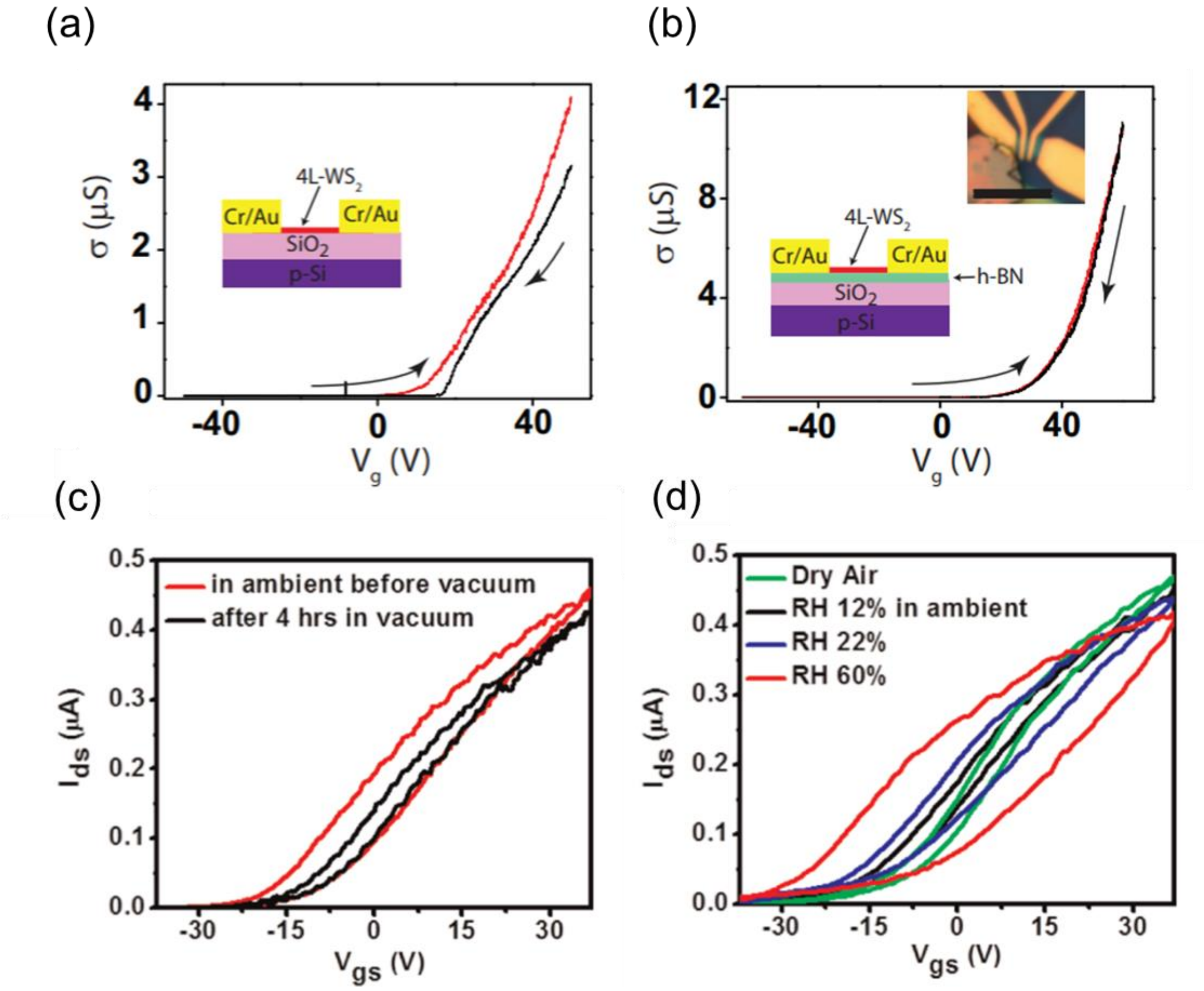

Figure 2-10. Effect of bottom and top interface on TMDC FETs. Hysteresis of multi-layered WS_2 transistors with bottom a) SiO_2 and b) h-BN interfaces. Effect of c) a vacuum environment and d) humidity on the hysteresis behaviour of MoS_2 FETs. Figures a,b) reproduced (adapted) with permission from ref[59]. Copyright 2014 Springer Nature Limited. Figure c,d) reproduced (adapted) with permission from ref[63]. Copyright 2012 American Chemical Society.

2.5.1. Photodetectors

TMDC monolayers are also very promising materials for optoelectronic device applications: electronic devices that generate, detect or control light.[1, 64] Optoelectronic devices that are flexible and transparent are becoming especially important in various applications such as solar cell arrays, wearable electronics and transparent displays. In this sense, TMDC monolayers with a direct semiconducting band gap, atomically-thin dimensions, and flexible/stretchable properties make these materials highly suitable for next-generation flexible and transparent optoelectronics.

Among the many forms of optoelectronic devices, photodetection is an essential element for imaging and sensing and this has been the most widely studied using TMDC monolayers. Down to a few atomic layers, TMDC crystals exhibit band gaps in the range of 1 to 2 eV, which are desirable for infrared to visible light detection.[13] Also, TMDC layers are considered promising for solar cells as they possess strong optical absorbance even for the atomic layer thicknesses as well as band gaps suitable for absorbing the solar spectrum.

The mechanisms that enable photodetection and contribute towards photocurrent generation generally involve either the photoelectric[65] or photo-thermoelectric effects.[13, 66] The photoelectric effect involves the separation of photogenerated electron-hole pairs when an electric field is present. This includes the photoconductive effect, which describes photoinduced changes in the channel resistance (due to photogenerated carriers under an external electric field), and the photovoltaic effect, which is when a built-in electric field is created from the semiconductor-semiconductor junction or metal-semiconductor junction.[67-69] Photo-thermoelectric effect occurs, on the other hand, when there is a temperature gradient across a semiconductor channel arising from light-induced heating.[70] The temperature difference leads to a voltage difference via the Seebeck effect, generally initiated by a focused laser spot with dimensions smaller than the channel dimensions, and this effect is very small compared to the photoelectric effect.[65] Therefore, we focus on the photoelectric effect as the main source of photocurrent in TMDC photodetectors.

A Phototransistor is the configuration that is typically employed in photodetectors made from TMDC monolayers. This device structure utilizes the same metal-semiconductor-metal configuration as an FET and operates under an applied source-drain bias as well as a gate-source bias under light illumination. Figure 2-11a shows the typical phototransistor architecture employed for studying TMDC monolayers.[71] Here, the SiO_2/Si substrate was used as a back-gate configuration, while the MoS_2 channel and source/drain electrodes were deposited on top of the substrate. In the work by Lopez *et al.*[71], the MoS_2 phototransistor was operated under different gate voltages as shown in Figure 2-11b. Under equilibrium conditions, the energy band diagram representing the electrodes and the MoS_2 monolayer exhibits a flat fermi-energy level, although there is a slight bending of the valence and conduction energy levels due to contact between the electrodes and the MoS_2 channel, which can be attributed to unavoidable fermi-level pinning at the interface. The phototransistor can be operated either in an On state ($V_g > V_{th}$) or Off state ($V_g < V_{th}$) depending on the gate voltages applied. When in the Off state, the Schottky barriers are high, and the photocurrent that is generated under illumination is the dominant channel current. As shown in Figure 2-11d, when in the On state, the Schottky barriers are lowered and thus thermionic and tunnelling currents can also contribute to the photocurrent. Generally, a high sensitivity is acquired during the Off state due to the lower dark current, and a high photoresponsivity is acquired during the On state due to the thermionic and tunnelling currents that add to the photocurrent.[10, 72]

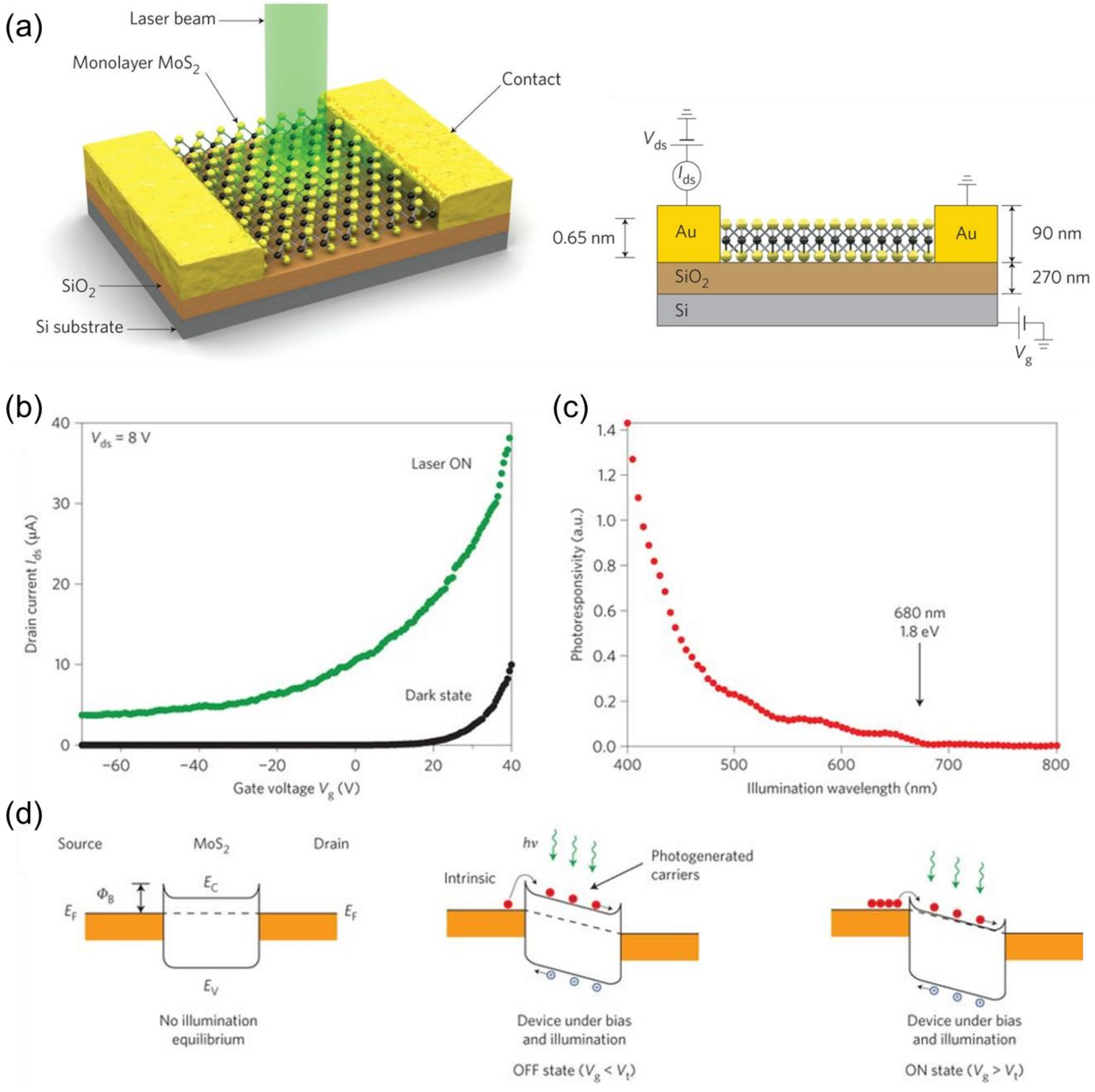

Figure 2-11. Phototransistor made from an MoS_2 monolayer. a) Schematic of the MoS_2 phototransistor. b) Photocurrent generation under various gate voltages. c) Photoresponsivity as a function of the illumination wavelength. d) A schematic illustration of the band diagram of an MoS_2 monolayer photodetector taking into account gate-voltage induced changes in the Schottky barriers. Figure reproduced (adapted) with permission from ref[71]. Copyright 2014 Springer Nature Limited.

Phototransistors made from CVD-grown MoS_2 monolayers are particularly sensitive to adsorbates in ambient air. By virtue of the large surface-to-volume ratio, the photoelectronic response of an MoS_2 phototransistor is affected by adsorbed air molecules, which act as p-type dopants. Zhang *et al.*[10] reported the effect of air molecules on the electrical and photoelectrical characteristics as shown in Figure 2-12. As seen in Figure 2-12a, the air molecules act as a p-type dopant which decreases the electrical conductance of MoS_2. This effect is also shown in the time-domain photoelectrical measurement where the decay time of the MoS_2 phototransistor measured in ambient air is shorter than the decay time measured in vacuum. This is because the adsorbed air molecules act as recombination sites where photogenerated electrons can recombine with holes trapped by the air molecules.[73] The recombination is also dominant under laser illumination. As seen in Figures 2-12c,d, photocurrent generation is decreased when measured in air compared to the photocurrent measured in vacuum, leading to lower values of photocurrent as well as the responsivity.

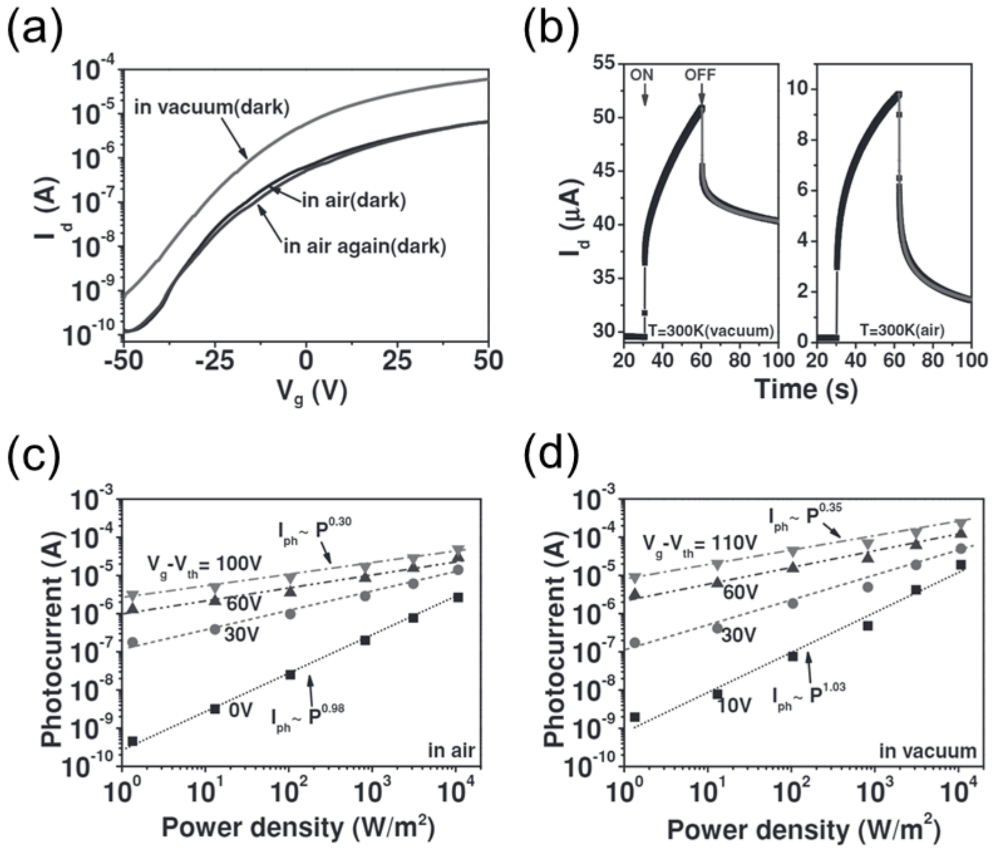

Figure 2-12. Effect of adsorbed air molecules on the photoresponse characteristics of MoS_2 phototransistors. a) Transfer curve, b) time-resolved photocurrent, and gate-bias dependent photocurrent measured in c) ambient air and d) vacuum environment. Figure reproduced (adapted) with permission from ref[10]. Copyright 2013 WILEY-VCH Verlag GmbH & Co. KGaA, Weinheim.

Chapter 3. Experimental techniques

The purpose of this chapter is to introduce the experimental setups and characterisation techniques that have been used to obtain results presented in the subsequent chapters of this thesis. I will explain in some detail the experimental apparatus that has been fundamental to my research on 2D TMDC monolayers. In particular, I will provide detailed information on the chemical vapour deposition (CVD) system used to form the monolayers, the processes employed to fabricate devices such as FETs and phototransistors, and the characterisation techniques such as Raman, PL, and AFM that have been used to analyse the resulting transition metal dichalcogenide (TMDC) monolayers that have been synthesized in this work.

3.1. CVD synthesis system

At present, one of the most promising and effective ways to achieve high quality and large area TMDC monolayers is through chemical vapour deposition. Even though top down approaches exist, such as exfoliation using scotch tape or electrochemical exfoliation, uniform layer thickness control still remains extremely difficult using these methods. CVD, on the other hand, offers an alternative route for producing 2D materials with a monolayer thickness and large-area. Also, the electrical and optoelectronic performance of TMDC devices are strongly influenced by the crystal quality (e.g. grain boundaries and defects) of TMDC monolayers. Therefore, synthesising highly crystalline monolayers using a CVD process is highly important in order to effectively utilise TMDC monolayers for practical applications.

The CVD process involves heating the source materials to the point of evaporation in a reaction chamber (planarGROW-2M) before the evaporated species are then carried off by inert gases such as argon and nitrogen. Following this, the evaporated species are then reacted to form a chemical compound on a target substrate. For the growth of TMDC materials, MO_3 (M = Mo or W) powders are generally used as the transition metal precursors along with sulphur or selenium powders. The CVD system used for the production of either MoS_2 or WS_2 monolayers is composed of four parts: (1) a 2-inch-diameter outer quartz tube with a 1-inch-diameter inner quartz tube, (2) a tubular furnace for heating, (3) a gas delivery system, and (4) a gas exhaust system (Figure 3-1). The 1-inch quartz tube was used simply for ease of tube cleaning as well as uniformity of the gas flow. In this system, the furnace is placed in the middle of the quartz tube and the temperature is controlled via the control panel (HANYOUNG NUX_PX7). The gas delivery and exhaust systems are placed at both ends of the quartz tube, where the insertion of gas is controlled by a mass flow controller (MFC, ATOVAC_GMC1200) which can precisely control the flow rate (0-1000 sccm) of the argon gas. In turn, the gas exhaust system is connected to a scrubber system. An alumina boat containing sulphur powders is placed upstream of the furnace while another boat containing MoO_3 precursors is placed in the middle of the furnace with a target substrate placed on the boat with it being faced down. Two potential growth/nucleation mechanisms[74] can occur when a CVD process is used to fabricate TMDC monolayers: (i) deposited MoO_{3-x} molecular clusters are reduced into MoS_{2-x} clusters on the SiO_2/Si substrate, leading to an initial growth process and continuous edge growth and (ii) MoO_3 molecules can be transported onto the SiO_2/Si substrate surface where they are sulfurized rapidly to form $MoO_{3-x}S_y$ nanoparticles, which then act as the nucleation sites for growth along the lateral and vertical directions. The two mechanisms can exist simultaneously during the CVD growth process, although one might dominate over the other depending on the reaction temperature, amount of precursors, flow rate, and etc.

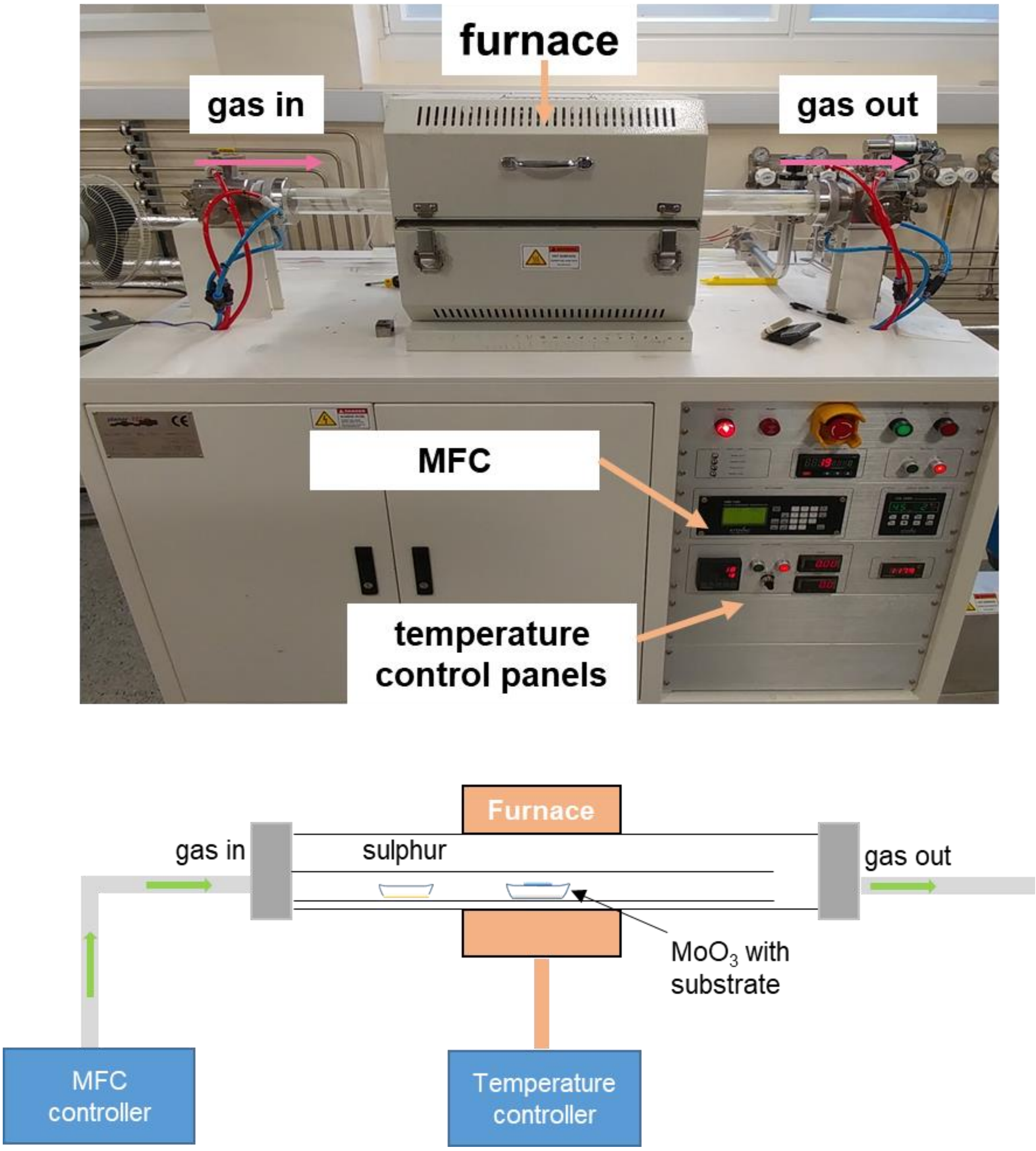

Figure 3-1. A photograph and schematic diagram of the CVD setup for the growth of TMDC monolayers.

3.2. Device fabrication

In order to fabricate a field effect transistor (FET), the source and drain electrodes should be patterned so that the metal can be selectively deposited. In this regard, photolithography and electron-beam lithography are most widely used for microscale or nanoscale FETs with the channel consisting of TMDC monolayers. Electron-beam lithography uses a focused electron beam to expose an electron-sensitive polymer resist film whereas photolithography uses ultraviolet light to expose a photoresist film using a photomask that allows light to pass through selected regions. E-beam lithography enables the patterning of electrodes below 1 μm, while photolithography enables the patterning at several micrometre scale. In both techniques, electron beam and UV light induce changes in the molecular structure and solubility of the resist. The exposed film then becomes soluble in developing agents known as the "developer". There are two types of resist: positive and negative resist. A positive resist refers to one that becomes soluble under UV light exposure and is developed under a developer. A negative resist refers to one that becomes crosslinked and remains un-developed by a developer after exposed to UV light.

For the photolithography process, a positive photoresist, MICROPOSIT S1813 G2, was used. The resist was spin coated onto a substrate for 1 minute at 4000 rpm to achieve a uniform film thickness of 1.5 μm. The photoresist is then baked at 115 ˚C for 1 minute. Using an EVG 620 mask aligner, a Cr-coated mask was contacted to the substrate and exposed with UV light (365 nm, 40 mW/cm^2). The exposed patterns were then developed with MICROPOSIT MF-321 for 50 seconds and finally rinsed with water. The device fabricated using photolithography and the mask design is shown in Figure 3-2.

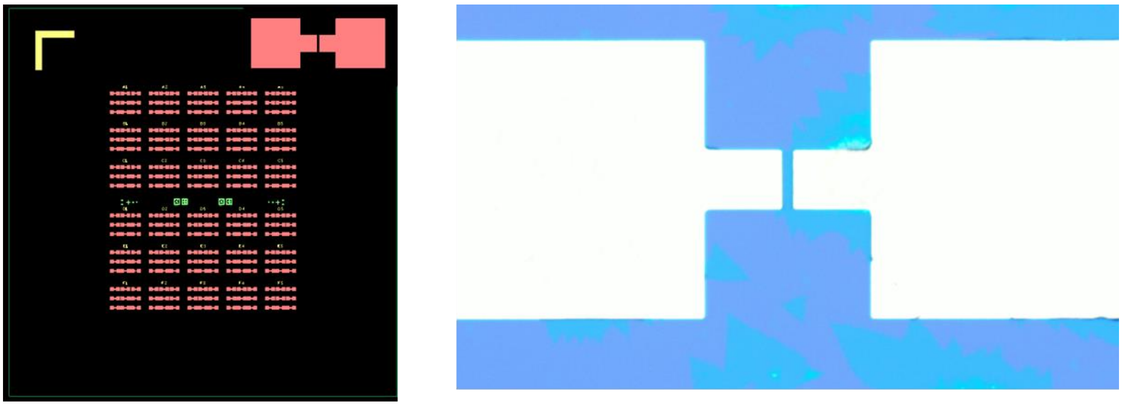

Figure 3-2. The images of photomask and the fabricated MoS_2 device**.**

For electron-beam lithography, on the other hand, Poly(methyl methacrylate) (PMMA 495K A4, MicroChem) was used as the electron-beam sensitive resist. PMMA was spin-coated onto the substrate for 45 seconds at 4000 rpm and baked at 180 ˚C for 90 seconds to reach a final film thickness of 180 nm. The sample was then exposed with an electron beam using Raith e_LiNE Plus for patterning the source and drain electrodes. Device patterns were drawn using computer-aided design (CAD) software (AutoCAD, Autodesk) as seen in Figure 3-3. A beam current of ~ 20 nA and a dose of ~ 100 $\mu C/cm^2$ were used for the electron beam writing. The exposed PMMA film was developed using a mixture of MIBK and isopropanol (1:3) for 45 seconds and then it was rinsed with isopropanol.

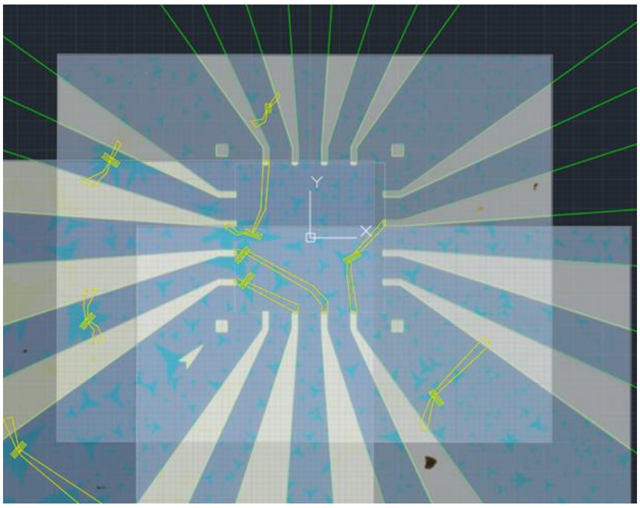

Figure 3-3. The image of an e-beam pattern design using Autocad software.

After patterning the source and drain electrodes using photolithography or e-beam lithography depending on the device design or targeting device dimensions, a thin layer of metal (e.g. Ti and Au) was then evaporated to be used as source and drain electrodes. A thermal evaporator was used to heat metal sources at Thin Film facility, department of physics at the University of Oxford. After deposition of metal layers, the resist was removed by a standard lift-off process using acetone for up to 2 hours. The electron beam writing was carried by Mr. Paul Giraud in NST group.

3.3. Raman and PL spectroscopy

Raman and photoluminescence (PL) spectroscopy were employed in order to investigate and determine the number of layers, lattice strain, doping level, and quality of the CVD-grown TMDC crystals. Both Raman and PL spectra were obtained using a Horiba JY LabRam

ARAMIS imaging confocal Raman microscope (x50). In the Raman microscope, a spectrometer is coupled to an optical microscope, enabling a high magnification (×50) and visualisation of the TMDC samples as well as a micrometre-sized laser spot for detecting the Raman and PL signals over a micrometre-sized area. For the measurements in this thesis, an excitation laser wavelength of 532 nm was used with a laser spot size of 1 μm^2. The Raman microscope is fitted with a piezo stage that is able to position the TMDC samples accurately in the x-y-z directions. For the spectrometer, there are two types of grating that can be selected, which are 600 gr/mm (grooves per millimetre) and 1800 gr/mm. These gratings quantify the resolution of the detected signal, and either a low resolution (600 grating) or high resolution (1800 grating) grating can be selected depending upon the resolution required. Typical linewidths in a Raman spectrum are between 1 and 10 cm^{-1}, and therefore the 1800 grating was used, while the 600 grating was sufficient for PL measurements.

Raman spectra were normally taken over the range from 200 to 600 cm^{-1} as the vibrational modes of TMDC monolayers are known to be located within this range. An acquisition time of 1-5 seconds and an accumulation number of 2 in a form of averaging were used to achieve a good signal-to-noise ratio as well as to avoid thermal damage to the TMDC crystals. PL spectra, on the other hand, were taken over the range of 540 to 800 nm with the same acquisition time and accumulation number used for the Raman spectra. Typical exitonic peaks of TMDC monolayers are known to exist within the wavelength range from 580 to 680 nm. 2D mapping of the Raman and PL spectrum can also be employed by conducting multi-point spectra collection across the x-y dimensions and the spectra was collected in a fixed step size. A typical acquisition time for mapping was 0.3-0.5 seconds with step sizes of around 1 μm. If the step size was too large, then this can cause degradation in the mapping resolution, while a step size that is too small can result in an extremely long acquisition time for the mapping measurements.

3.4. Atomic force microscopy

Atomic force microscopy (AFM) is one of the most accurate methods for determining the thickness and surface morphology of TMDC crystals. The as-grown TMDC monolayers on the SiO_2/Si substrate can be directly used for measuring the thickness between the substrate and TMDC crystals in order to quantify the number of layers. AFM characterisation was performed using a Veeco Dimension 3100 AFM in a tapping mode with a doped silicon cantilever (TESPA-V2, BRUNKER, spring constant of 42 N/m and resonant frequency of 300 kHz). In the tapping mode, a cantilever is driven to oscillate up and down with a constant frequency and amplitude, which is achieved using a piezo-element. As the oscillating cantilever starts to intermittently contact the surface of the crystals, the oscillation of the cantilever is necessarily reduced due to energy loss caused by the tip contacting the surface. The reduction in the amplitude is used to identify and measure surface features. The oscillation amplitude of the tip is measured by the detector. Using this tapping mode, both a topographic and phase image can be obtained. The topographic image provides a measure of the changes in amplitude of oscillation while the phase image provides information on the phase shift relative to a driving oscillator, which changes when the probe tip encounters a different material composition. For most of the AFM measurements, a topographic image is shown to quantify the height of the TMDC crystals and consequently the number of layers.

The AFM topographic images are shown in later chapters. AFM measurements presented in this thesis were carried out by Dr. Yuljae Cho of the Nanoscience and Technology group.

3.5. Transmission electron microscopy

Transmission electron microscopy (TEM) measurements were conducted at Ulsan National Institute of Science and Technology (UNIST) in South Korea by Prof. Hu Young Jeong. The TEM measurement was conducted using an aberration-corrected FEI Titan Cube TEM (FEI Titan G2 60-300) under an accelerating voltage of 80 kV.

TEM is a microscopy technique that uses high energy electrons, and the electron beam is accelerated and focused onto a sample. The beam transmits through the sample to form magnified images of very thin samples down to atomic resolution. TEM is an undoubtedly useful and powerful technique to characterise morphology, crystal structure, defects, and chemical composition of TMDC materials at the atomic scale. Using the TEM, operational modes enables the acquisition of phase contrast high-resolution TEM (HRTEM) images and scanning TEM (STEM) images of TMDC monolayers (presented in Section 4.2.2). HRTEM imaging relies on phase differences through diffraction as the electrons pass through the sample. In STEM, condenser lenses are employed to focus electrons into an atomically-small beam size (typically 0.05 – 0.2 nm) so that the electron beam scans the atoms of the TMDC sample and scattered intensity is recorded to from an image.[75] Annular dark field (ADF) STEM images are directly interpretable for TMDC monolayers and heterostructures because the contrast reflects the atomic number and the specimen thickness. Therefore, in Chapters 4 and 6, ADF STEM images were taken to give reliable information on the atomic interface and stacking orientation.

3.6. Electronic and opto-electronic measurements

All electrical measurements (e.g. transfer curves and output curves) presented in this thesis were performed using a Keithley 4200-SCS Parameter Analyzer that was synchronized with a Cascade Microtech Probe Station (EPS150) and was located inside a Cascade Microtech Shield Enclosure, which blocks the system from ambient light and noise present in the surrounding environment as shown in Figure 3-4. Source and drain pads for the devices were contacted using micrometre-sized tungsten probe tips and measured under ambient conditions. Using the Keithley Parameter Analyzer, it is possible to apply DC voltages to the source, drain, and gate pads and read current that is passed through the electrodes. The model enables analysis of semiconductor devices with high precision and sub-femtoamp resolution.

Opto-electrical measurements were also performed inside the shield chamber where dot laser modules of either 450 nm or 850 nm wavelengths (STAR450F5, LDM850/3LJ, ROITHNER LaserTechnik) were positioned using a magnetic positioner that can position the lasers accurately on the device. 450 nm laser modules were used to measure the photocurrent of MoS_2 because the laser energy is larger than the bandgap of MoS_2 monolayer, whereas the 850 nm laser module was used to measure the MoS_2/QDs hybrid structure in Chapter 7. The power of the laser sources was measured using a digital optical power and energy meter (Thorlabs, PM100D, power range from 100 pW to 200 W). For time-resolved photocurrent measurements, the probes of the probe station were connected to a Stanford Research Systems SR 570 current preamplifier and Lecroy HD4000 high definition oscilloscopes, and the photocurrent signals were obtained using the Lecroy HD4000 oscilloscopes.

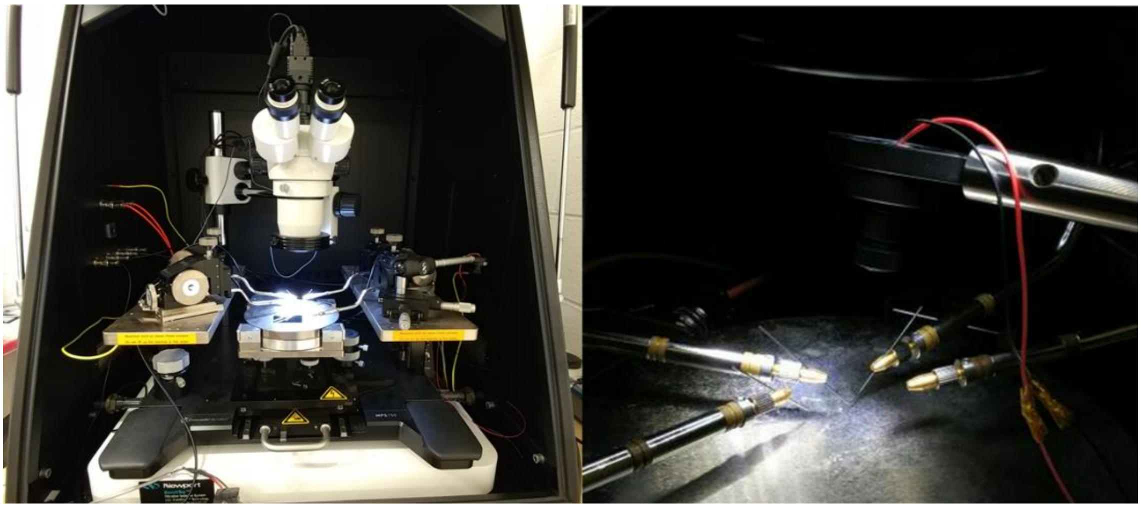

Figure 3-4. Photograph showing the electrical and optoelectrical measurement setups.

Chapter 4. CVD synthesis of TMDC monolayers

4.1. Introduction

This chapter introduces a strategy developed by me and a colleague to synthesize high quality and large crystalline transition metal dichalcogenide (TMDC) monolayers and their corresponding heterostructures. TMDC crystals synthesized using the unique approach developed in this study were then used in the studies on the various fundamental properties of TMDCs and device applications which are presented in the following chapters.

It is known that the electrical and optoelectronic properties of TMDC devices are strongly influenced by the presence of grain boundaries and defects.[57, 76-78] To utilize TMDC monolayers for device applications, it is therefore important to synthesize large-sized crystals and highly crystalline TMDC monolayers. There are many studies focused on developing scalable synthetic routes for production of TMDC monolayer films.[8] These studies include thermolysis,[79, 80] pulsed laser deposition,[81, 82] sulfurization of coated transition metal or transition metal oxide films[83, 84], and chemical vapour deposition (CVD).[85-87] Among the different synthetic processes, CVD is perhaps the most promising and practical method for synthesizing highly crystalline TMDC monolayers that possess good electrical and optical properties.[88] Even though CVD is an effective method to grow uniform and highly crystalline TMDC monolayers, there still remain challenges with regards to the growth of uniform and large-scale crystals that are suitable for practical device applications.

From the early reports of growing TMDC monolayers using CVD, solid transition metal oxide powders (e.g. MoO_3) have been used as the precursors.[76] In this approach, a SiO_2/Si substrate is placed faced down on the alumina boat containing the metal oxide precursors so that the metal oxide powders can violently react with the sulphur/selenium precursors that are to be synthesized on the substrate.[87] With this powder-based approach, however, it is not easy to obtain a uniform film of a TMDC monolayer due to the difficulty of controlling the nucleation density, arising from the high number of kinetic reactions that take place at high temperatures (700-900 ˚C) as well as the nonuniform distribution of precursor powders. As a result, clean MoS_2 monolayers are grown only in specific regions where the MoO_3 vapour concentration is low. Another approach has been suggested which involves placing the SiO_2/Si substrate far from the MoO_3 precursors.[89, 90] However, MoS_2 crystals synthesized using this approach show position-dependent crystal sizes and quality. It is therefore desirable to develop a new synthetic approach involving CVD that allows for the fabrication of uniform and large-scale TMDC monolayers with a high degree of crystallinity.

In this chapter, a novel method for synthesizing large-area TMDC monolayers with large-sized single crystal grains is proposed. This is achieved by significantly lowering the vapour concentration of the transition metal oxide precursors via control of a solution-processed precursor. Large-sized MoS_2 and WS_2 monolayers were synthesized using this approach by controlling their nucleation density and the quality of their crystals was confirmed using the various characterisation techniques described in the previous chapter.

Furthermore, it is demonstrated that by using this approach, it is also possible to synthesize MoS_2/WS_2 heterostructures that exhibit a clear heterostructure interface.

4.2. MoS_2 monolayer

4.2.1. MoS_2 synthesis

The synthesis of MoS_2 monolayers was performed using MoO_3 and sulphur as the precursors, as described in Chapter 3. In order to reduce the nucleation density of MoS_2 on the substrate, it is important to induce a low supersaturation state from the vapour reactants. To do so, the MoO_3 concentration must be relatively low, and therefore, MoO_3 was dissolved in ammonium hydroxide, NH_4OH, (2 mg/ml). 50 μL of the dissolved precursor solution was then dropped into the alumina boat using an adjustable-volume pipette and dried at 300 ˚C for 10 minutes on a hot-plate. The weight of MoO_3 was calculated to be 0.01 mg. Note that the weight of the MoO_3 precursor is 2-3 orders of magnitude lower than that of the solid precursors typically employed in the literatures.[87, 91] A 2 cm x 2 cm SiO_2/Si substrate was cleaned and surface treated with oxygen plasma for 10 minutes before being placed on the alumina boat with its face turned upside down. 50 mg of sulphur powders was then loaded into another alumina boat, which was then located in the upstream of the furnace, whereas the alumina boat containing the MoO_3 and the substrate were placed in the middle of the furnace as shown in Figure 4-1.

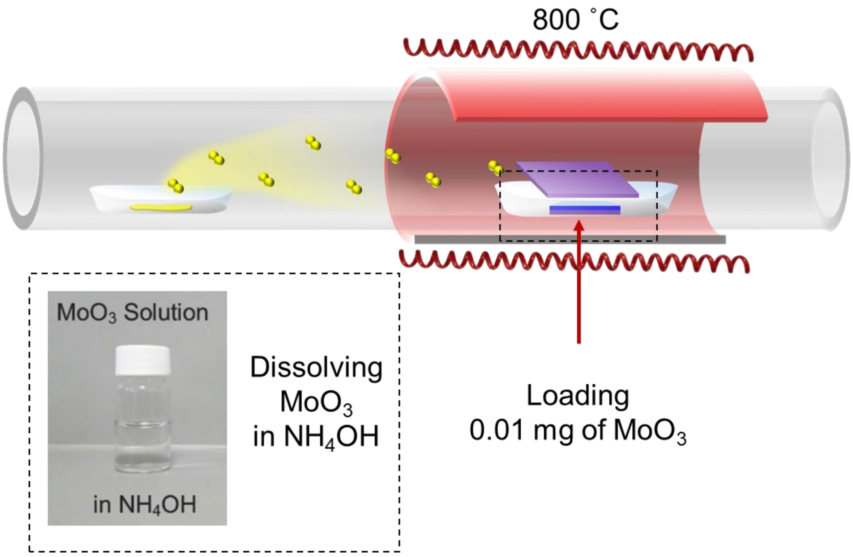

Figure 4-1. A schematic illustration of the CVD synthesis of an MoS_2 monolayer.

The CVD process is performed inside a quartz tube with a furnace placed in the middle of the tube. Before each experiment, the alumina boat and quartz tube were annealed at 1000 ˚C for over 1 hour in order to completely remove any precursor residues. The furnace chamber was heated to 300 ˚C and was purged with argon gas in order to remove water and oxygen in the chamber. The CVD process was performed at atmospheric pressure with a continuous flow of pure argon gas. The specific growth procedure for an MoS_2 monolayer that was used in this study was as follow (Figure 4-2): ramp the temperature of the furnace to 800 ˚C at a rate of 20 ˚C/min in the presence of an argon gas flow of 150 sccm; at 720 ˚C, the sulphur starts to evaporate and was transported by the Ar carrier gas; the temperature of the furnace continues to rise to 800 ˚C and maintain the temperature for 5 minutes; the furnace was then cooled naturally down to room temperature. The growth of the TMDC monolayer starts when the sulphur is introduced. Although the growth rate is difficult to accurately define, the average size of the MoS_2 crystal is around 200 μm when the growth time is 3 minutes at 800 ˚C and when the amount of MoO_3 precursor is 0.01 mg. In this sense, the growth rate can be estimated to be 66.7 μm/min. However, it should be noted that the growth process can continue even when cooling down until the temperature of the furnace is reduced below the reaction temperature (< 600 ˚C).

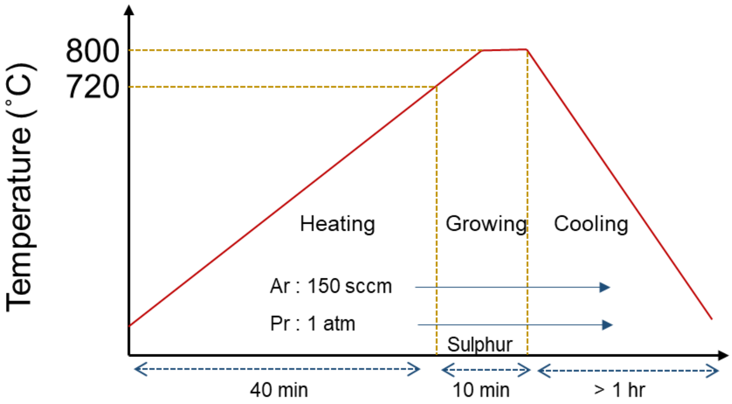

Figure 4-2. Growth procedure of an MoS_2 monolayer.

Supersaturation is the driving force behind the nucleation and growth of the MoS_2 crystal.[92] If the pressure of vapour phase (assuming constant temperature) is increased beyond the vapour pressure of the solid, then a state of supersatureation is achieved,[92, 93] while saturation is an equilibrium condition where a gas phase is in equilibrium with the solid phase. Therefore, the degree of supersaturation is dependent on the amount of reactive gas species and affect the nucleation rate, growth rate, and size of the crystals. The extremely small number of precursors and high growth temperature (800 ˚C) result in the following: the low supersaturation level near the substrate leads to a low nucleation density grown on the surface of the substrate whereas the high growth temperature maximizes the crystal size and the degree of crystallinity. The low supersaturation leads to a low nucleation rate, guaranteeing a thermodynamically stable reaction during the growth procedure.[89, 94] In this thermodynamically stable synthesis process, the reactive species have enough energy and time to diffuse to energetically favourable locations near the nucleation sites, leading to a stable structural growth of the crystal. However, if the amount of MoO_3 precursors is sufficiently large, the growth process can be dominated by a kinetic-controlled reaction. In this case, the nucleation density becomes high, and the size of the MoS_2 crystals reduces. The reaction-dependent MoS_2 monolayer synthesis is depicted in Figure 4-3. It can be clearly observed that the size of the crystals decreases when there are excess MoO_3 precursors. Using 0.01 mg of MoO_3 precursor, a continuous MoS_2 film can be obtained at the centre of the substrate, while large-sized triangular crystals are grown near the edges of the substrate where the flow of the precursors is insufficient (Figure 4-4). The largest crystal size was found to be as large as 500 μm. It should be noted that the amount of MoO_3 (0.01 mg) used in this study is 2-3 orders of magnitude lower than that typically employed using the same CVD configuration as that used in this study (i.e. the SiO_2 substrate facing down on the boat containing the MoO_3 precursor).[76, 89, 95] This means that our setup induces a low supersaturation level, supported by the nucleation density and crystal size in Figure 4-3b.

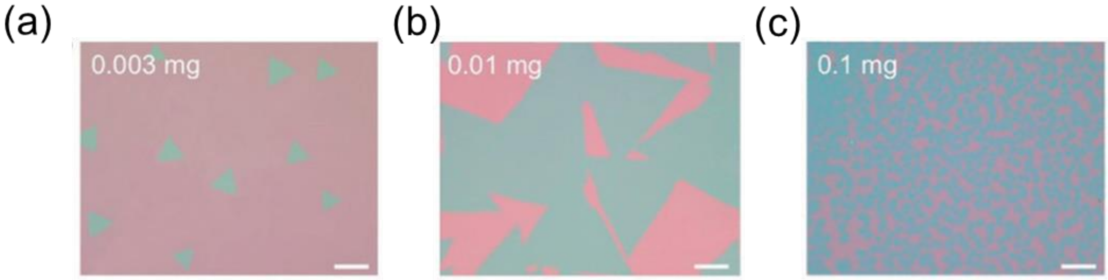

Figure 4-3. MoS_2 crystal size and nucleation density when the amount of precursor is varied. Optical microscope images when (a) 0.003 mg, (b) 0.01 mg, and (c) 0.1 mg of MoO_3 precursors were used. The images were taken by Juwon Lee in the NST group. Scale bar: 100 µm. Figure reproduced (adapted) with permission from Ref[96]. Copyright 2017 John Wiley and Sons.

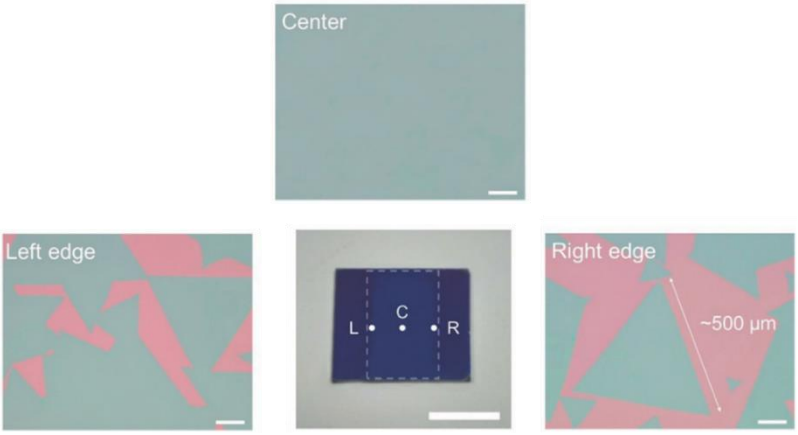

Figure 4-4. Optical images of an MoS_2 monolayer grown when 0.01 mg of the MoO_3 precursor was used. The images were taken from the left side, centre, and right side of the SiO_2/Si substrate. In the middle of the substrate, a continuous MoS_2 film has been formed, while large MoS_2 crystals up to 500 µm are grown on the left- and right-hand side of the substrate. Scale bar: 100 µm. The images were taken by Juwon Lee in the NST group. Figure reproduced (adapted) with permission from Ref[96]. Copyright 2017 John Wiley and Sons.

4.2.2. MoS_2 characterisation

The quality of the MoS_2 crystals grown using the above method was assessed using a combination of techniques including AFM, Raman spectroscopy, PL spectroscopy, and TEM imaging. Figure 4-5 shows an AFM topography image of an as-grown MoS_2 monolayer on the SiO_2/Si substrate, which was taken using the tapping mode of the AFM as described in Chapter 3, Section 4. A uniform surface morphology as well as a monolayer thickness of ~0.8 nm can be seen. Raman and PL measurements were carried out to confirm their layer thickness and crystal properties, and in this regard, Figure 4-6a shows the Raman spectrum of the as-grown MoS_2 monolayer. The difference in the frequencies for the E^1_{2g} and A_{1g} modes is found to be ~18.8 cm^{-1}, in accordance with that of a monolayer.

Additionally, Figure 4-6b shows an example of the PL spectrum from the MoS_2 monolayer with the PL emission peak centred at ~1.86 eV. Noticeably, the PL intensity of the as-grown monolayer is rather intense with its FWHM found to be as small as 48 meV. This value is close to or even better than that reported for exfoliated or suspended MoS_2 crystals.[40, 97] To verify the crystal quality and homogeneity of the MoS_2 monolayer over the entire substrate, Raman and PL spectra were taken at 50 different locations on the substrate. Statistical values for the Raman frequency, Raman FWHM, PL emission centre, PL FWHM are plotted in Figure 4-6c,d. Here the standard deviation was found to be 0.16 cm^{-1} and 1.1 meV for the E^1_{2g} Raman mode and PL peak position, respectively, clearly highlighting the uniformity of monolayer over the entire substrate.

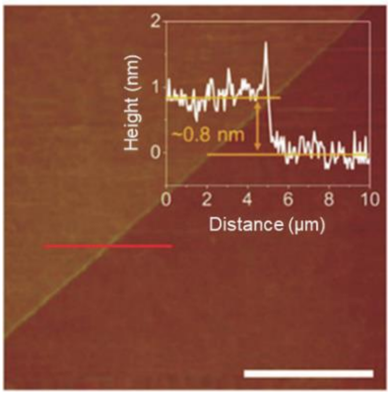

Figure 4-5. AFM topography image of an MoS_2 monolayer. Scale bar: 10 μm. The AFM was measured by Mr. Yuljae Cho in the NST group. Figure reproduced (adapted) with permission from Ref[96]. Copyright 2017 John Wiley and Sons.

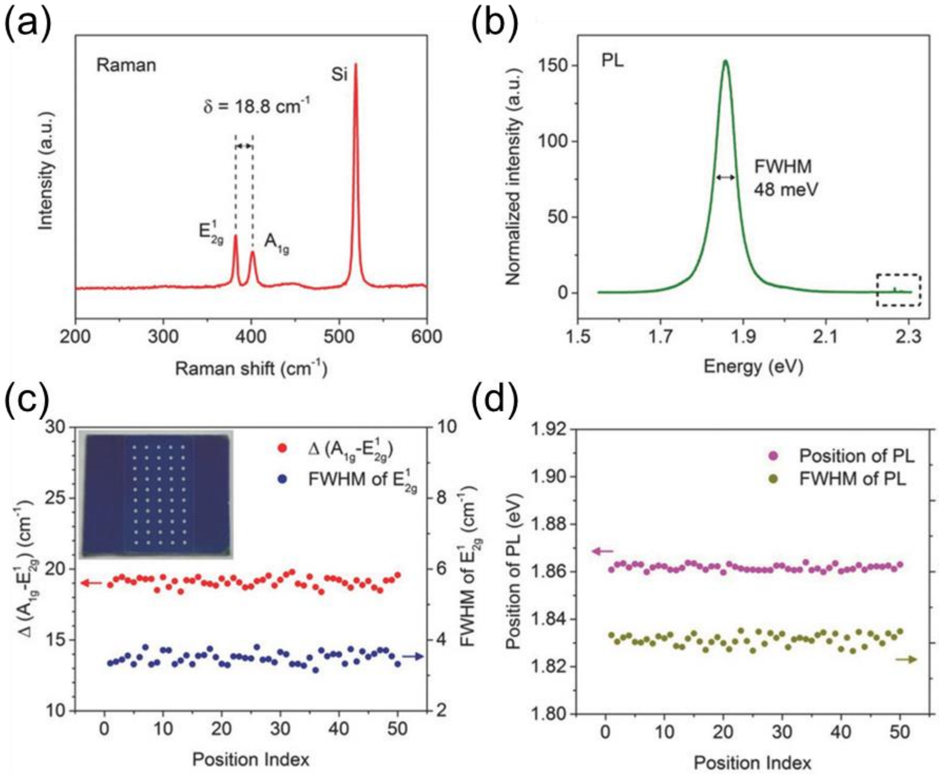

Figure 4-6. Raman and PL measurements of a MoS_2 monolayer. a) Raman and b) PL spectrum obtained from a single-crystalline MoS_2 monolayer. The dashed box in b) highlights the strong PL intensity with respect to the Raman peaks. c) The frequency difference between the two Raman vibrational modes (primary axis) and FWHM (secondary axis) of the E^1_{2g} peak obtained across the

substrate. The inset image illustrates where the measurements were taken on the substrate. d) PL emission peak (primary axis) and FWHM (secondary axis) obtained at different locations across the substrate. Figure reproduced (adapted) with permission from ref[96]. Copyright 2017 John Wiley and Sons.

The crystal structure of the MoS_2 monolayer was examined using a combination of high-resolution TEM, selected area electron diffraction (SAED), and annular dark-field scanning transmission electron microscopy (ADF-STEM), all of which are presented in Figure 4-7. The TEM image (Figure 4-7a) shows a smooth, uniform surface with a well-organized honeycomb structure, whilst the corresponding hexagonal symmetrical pattern in the SAED data verifies the single-crystalline nature of the MoS_2. The ADF-STEM image (Figure 4-7b) reveals the atomic configuration of the MoS_2 which clearly distinguishes the spatial distribution of individual Mo and S atoms.

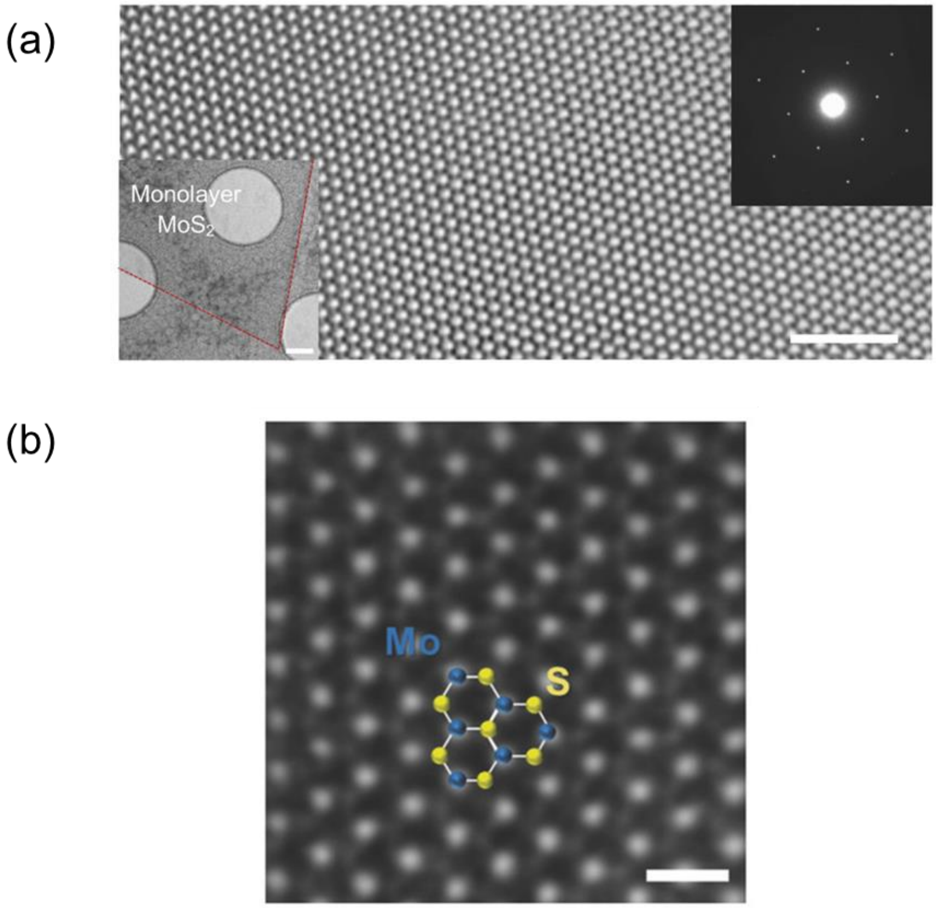

Figure 4-7. TEM images of an MoS_2 monolayer. a) High-resolution TEM image and b) STEM image of a MoS_2 monolayer. Scale bar: 2 nm for a) and 0.5 nm for b). The images were taken at UNIST by Prof. Hu Young Jeong. Figure reproduced (adapted) with permission from ref[96]. Copyright 2017 John Wiley and Sons.

4.3. WS_2 monolayer

4.3.1. WS_2 synthesis

A similar process to that used for MoS_2 was used to synthesize high-quality, large-sized WS_2 monolayer crystals, which was performed in the CVD system described in Chapter 3, Section 1. For the growth of the WS_2 monolayers, WO_3 precursors were first dissolved in NH_4OH (20 mg/ml), and 50 μL of the dissolved precursor solution was then dropped into an alumina boat using an adjustable-volume pipette before being dried at 300 ˚C for 10 minutes on a hot-plate. The growth of an WS_2 monolayer was conducted using a similar procedure as described for the MoS_2 monolayer, except for the growth temperature, sulphur introduction time, and growth time. The detailed growth procedure is depicted in Figure 4-8. In this case, a growth temperature of 950 ˚C was used because the vapour pressure of WO_3 is much lower than that of MoO_3. Furthermore, a growth time of 30 minutes was used to increase the crystal size. Using this growth procedure, WS_2 monolayer with crystal sizes up to 360 μm were achieved as shown in Figure 4-9. The growth rate of WS_2 can be estimated to be 7.3 μm/min (at 950 ˚C). However, it was not possible to grow an WS_2 film over the entire substrate.

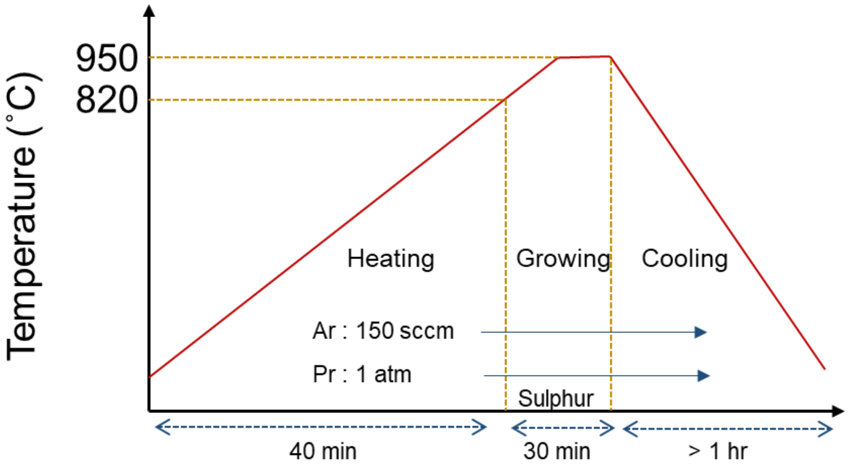

Figure 4-8. Growth procedure of an WS_2 monolayer.

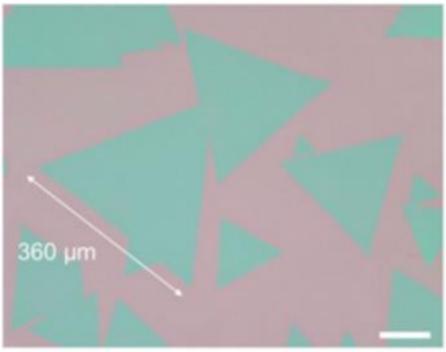

Figure 4-9. An optical image of an WS_2 monolayer. Scale bar: 100 μm. Figure reproduced (adapted) with permission from ref[96]. Copyright 2017 John Wiley and Sons.

4.3.2. WS_2 characterisation

Figure 4-10 shows the Raman and PL spectrum of an WS_2 monolayer grown on the SiO_2/Si substrate using the procedure described in the previous section. The Raman spectrum was taken using a 532 nm excitation wavelength and further details of the system are provided in Chapter 3, Section 2. The spectrum in Figure 4-10a shows two main peaks at 351 cm^{-1} and 417 cm^{-1}, which can be assigned to the overlapping of 2LA (longitudinal acoustic mode) mode with the E^1_{2g} mode and the A_{1g} mode, respectively. The 2LA mode as well as the remaining deconvoluted peaks that do not correspond to the A_{1g} and E^1_{2g} modes are second-order peaks that are much stronger (or as strong) as the first-order peaks (e.g. A_{1g} and E^1_{2g}). These are attributed to the laser wavelength that was used as this is in resonance with the B exciton peak (one of the electronic transitions) of the WS_2 monolayer. Such frequency coincidence (Resonance Raman scattering) can lead to enhanced Raman intensities. The difference between the two Raman vibrational modes (A_{1g} and 2LA) was

~66 cm^{-1}, which is consistent with earlier studies that state that this is indicative of a single-layer of WS_2.[32, 33] Figure 4-10, on the other hand, shows a strong PL peak centred at around 630 nm. This is also a clear signature that the WS_2 synthesized in this work is single-layered. The FWHM of the PL peak was around 50 meV, which implies that the WS_2 monolayer grown using the method is highly crystalline.

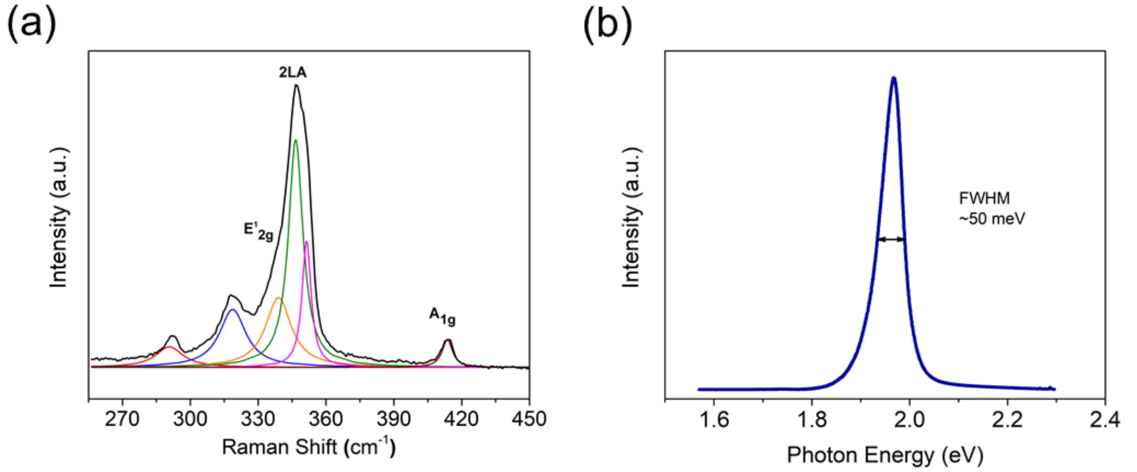

Figure 4-10. Raman and PL spectrum of an WS_2 monolayer. The 2LA and A_{1g} modes are the most characteristic peaks of WS_2 when measured under 532 nm laser illumination. The deconvoluted peaks at around 291, 317, 342, and 351 cm^{-1} correspond to second order Raman peaks resulting from the coupling between the laser and the excited states.

4.4. MoS_2/WS_2 in-plane heterostructures

Using the synthetic process employed to fabricate the MoS_2 and WS_2 monolayers, it is possible to grow MoS_2/WS_2 heterostructures. Generally, there are two approaches for synthesizing MoS_2/WS_2 heterostructures, which can be classified as either a one-step[98-100] or two-step[101-104] CVD synthesis procedure. For the one-step growth process,

MoO_3 and WO_3 precursors are loaded together so that the MoS_2 grows first followed by the WS_2 layer, or vice versa if there is a multi-heat zone in the furnace. For the two-step growth process, the substrate with the material synthesised first is taken out of the furnace, and the furnace is then rearranged to grow the second material. It is generally preferable to grow the heterostructures using the two-step synthetic procedure as it is easier to control the precursor and prevent precursor-mixing, which can lead to the formation of alloys. However, the one-step growth approach is more desirable from the point of view that the heterostructure can be grown sequentially under similar synthetic conditions to ensure energetically stable synthesis of the shell layer. Our synthetic approach, which uses a small amount of precursor, is perhaps better suited to the one-step synthetic procedure because the MoO_3 precursor can be consumed first in a fast timescale.

4.4.1. MoS_2/WS_2 heterostructure synthesis

For the growth of the MoS_2/WS_2 heterostructure, a MoO_3 solution in ammonium hydroxide (NH_4OH) was dropped onto an alumina boat as before (0.005~0.01 mg). To ensure a sufficient supply of tungsten, the WO_3 precursors were scattered directly onto the SiO_2/Si substrate using a solution containing WO_3 and sodium cholate together in the NH_4OH solution as shown in Figure 4-11a. This is because the vapour concentration of the WO_3 powder is much lower than that of MoO_3. The heavy weight of sodium cholate makes it possible to scatter the WO_3 precursor and sodium cholate onto the substrate, and the carbon ring structure of sodium cholate helps with the nucleation of TMDC monolayers.[105] The substrate was then placed on the alumina boat with its face placed upside down (Figure 4-11a), and the growth procedure for the heterostructure was the same as the growth procedure for the MoS_2 monolayer, where the furnace was heated up to 800 ˚C. The growth time was about 10-15 minutes. Figure 4-11b shows the MoS_2/WS_2 hetero-structured crystals grown on the SiO_2/Si substrate. The MoS_2 monolayer was grown first (inner) at a relatively low temperature, and WS_2 was subsequently grown laterally (outer) from the edge of the MoS_2 monolayers. This is due to the high nucleation and growth rate of MoS_2 and the high vaporisation temperature of the tungsten oxide. This is due to the high nucleation and growth rate of MoS_2 and the high vaporisation temperature of the tungsten oxide. It should be noted that WS_2 does not normally grow in the temperature of 800 ˚C when there is no MoS_2 present. The selective growth of the WS_2 region outside of the MoS_2 inner region suggests that the MoS_2 acts as a catalyst for the growth of WS_2 outer region.

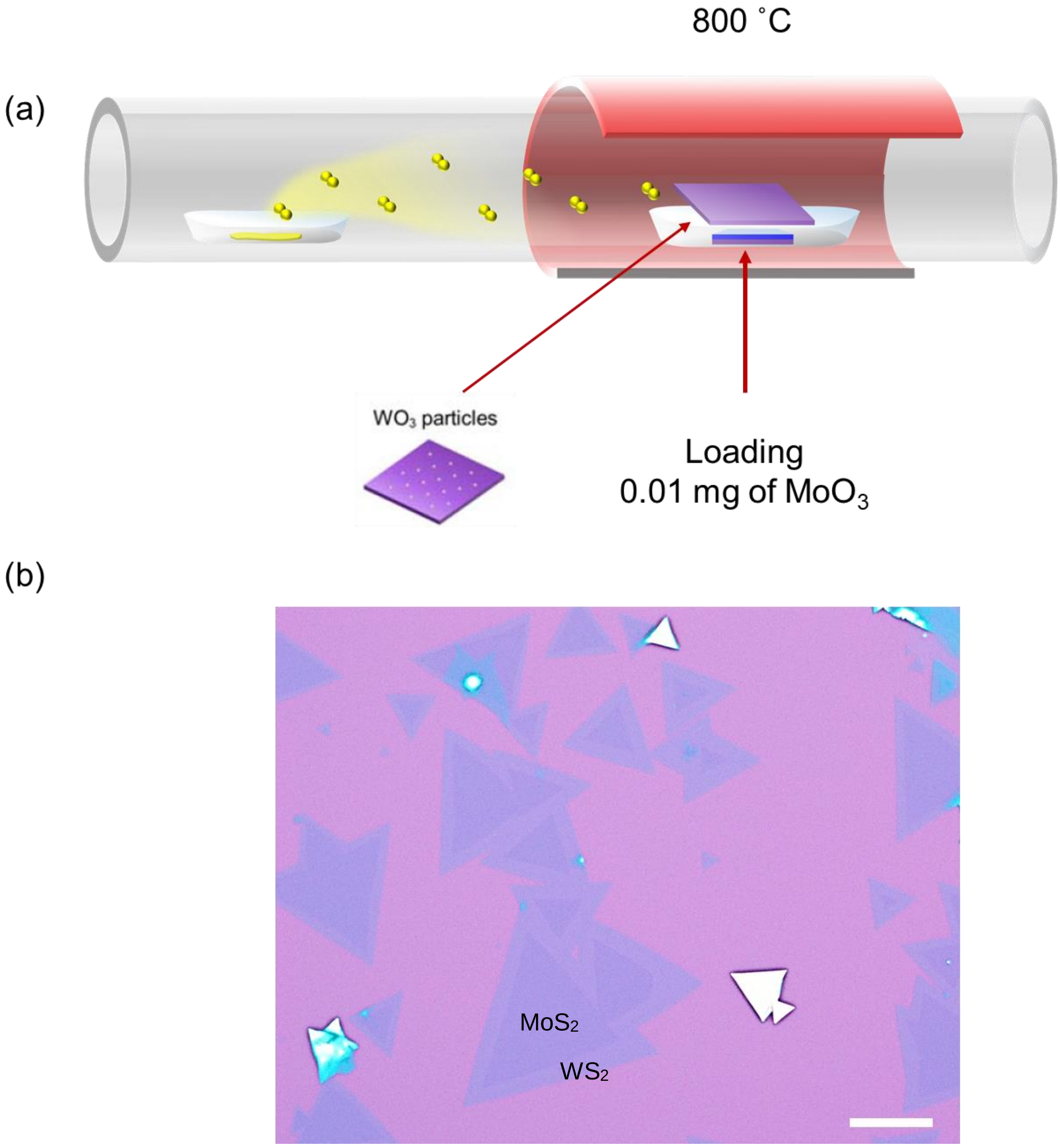

Figure 4-11. Synthesis of an MoS_2/WS_2 heterostructure used in this thesis. a) A schematic illustration of the heterostructure growth process. b) An optical image of the synthesized MoS_2/WS_2 heterostructure. Scale bar: 20 μm.

4.4.2. MoS_2/WS_2 heterostructure characterisation

To confirm and clearly discern that the synthesized heterostructure is indeed a combination of MoS_2/WS_2 monolayers, TEM, Raman, and PL measurements were carried out. Figures 4-12a and b show the optical microscope image and scanning transmission electron microscope (STEM) image of MoS_2/WS_2 heterostructure, respectively. It can be seen optically that the MoS_2 and WS_2 regions are clearly separated, which is discerned from the optical contrast between the two monolayers. The STEM image shows a clear separation of the MoS_2 and WS_2 regions; however, there is a slight diffusion of the tungsten atoms and formation of an alloyed region in the MoS_2 region only. Also, the Mo atoms are not found in the WS_2 region, implying that the precursors were not mixed together during the growth process due to the complete consumption of the MoO_3 precursors. Unfortunately, the slight formation of alloys at the interface was unavoidable.

To further characterize the spatial distributions of the lateral heterostructures, the material transition from MoS_2 to WS_2 was monitored using Raman and PL spectra. Figure 4-12c shows the line scan from a Raman spectrum collected at the interface of the heterostructure (marked in 4-12a). It shows that there is no clear sign of the formation of $Mo_xW_{1-x}S_2$ alloys, typically identified by a shift in the Raman frequencies. The clear heterostructure interface was also evident from the PL spectrum, as shown in Figure 4-13. Intermediate peaks, indicative of the formation of alloys, were not found. The characterisation shows that the interference from the vaporized MoO_3 molecules is largely suppressed during the growth of the WS_2 region due to an extremely small number of MoO_3 precursors employed in this work.

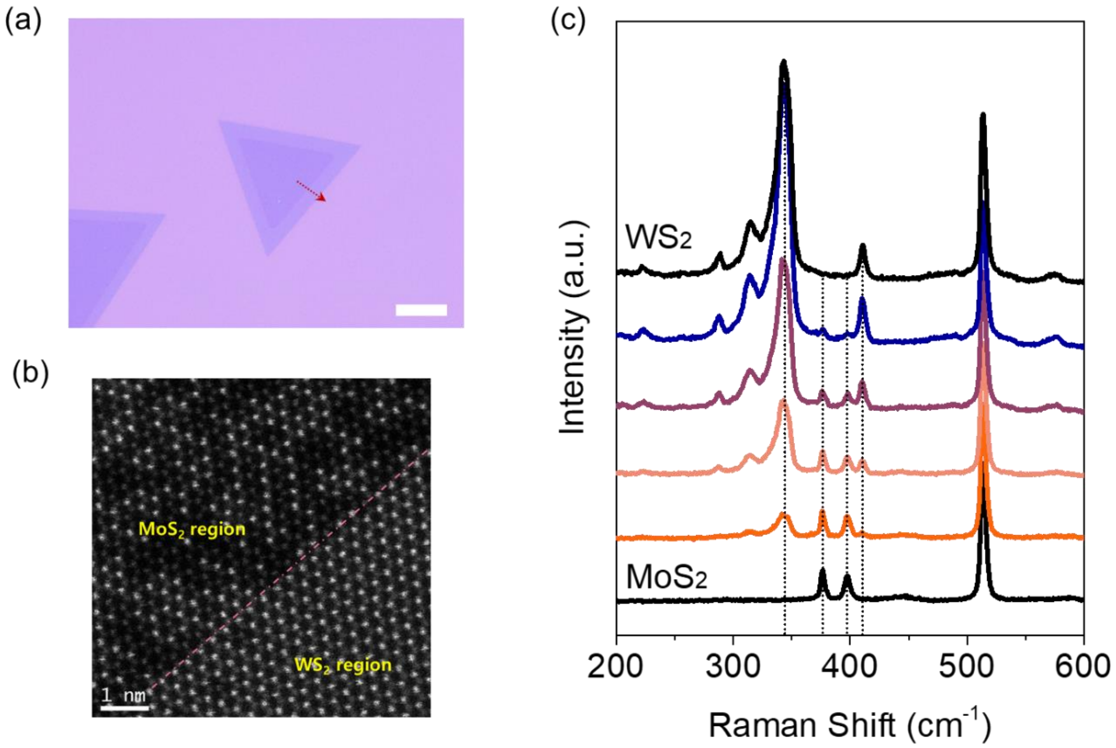

Figure 4-12. Characterisation of an MoS_2/WS_2 heterostructure synthesized using the one-step approach employed in this thesis. a) An optical image of a MoS_2/WS_2 heterostructure. The MoS_2 monolayer is grown first in the inner region before WS_2 is subsequently grown at the outer region. The optical contrast shows that the heterostructure has a sharp interface. Scale bar: 10 µm. b) STEM image of the interface between the two layers of the heterostructure. The STEM image shows that the interface is atomically sharp. However, there is some contamination from the tungsten atoms in the MoS_2 region. Scale bar: 1 nm. c) Raman transition at the interface of the heterostructure marked in a). Raman spectrum was taken starting from the inner MoS_2 region to the outer WS_2 region with a 1 µm step size.

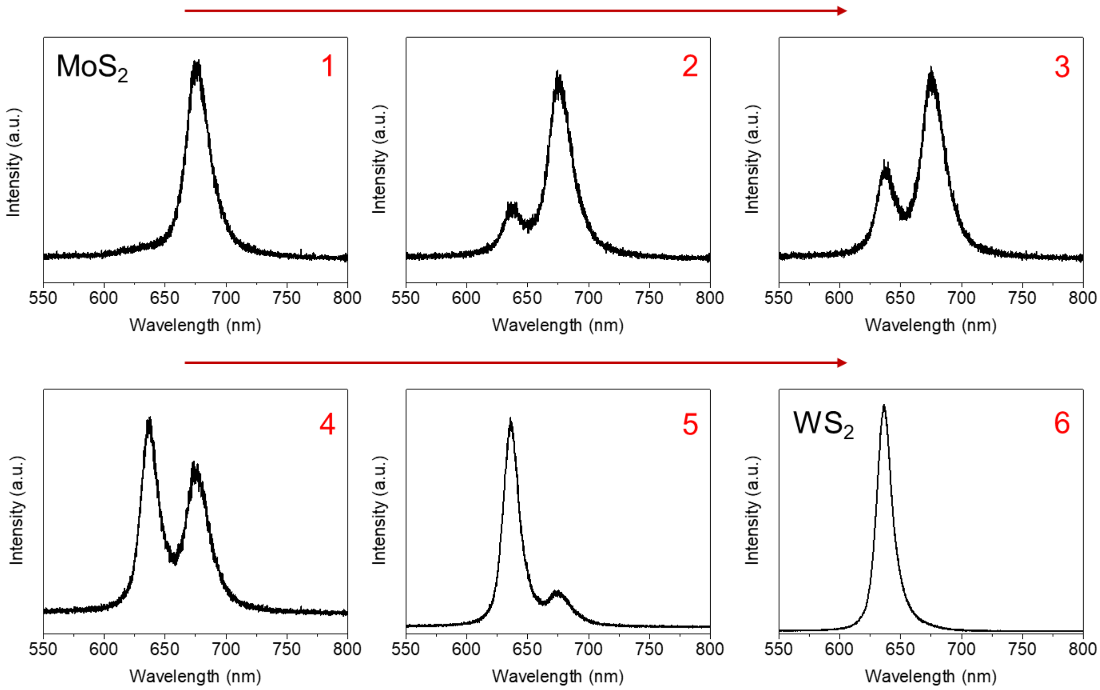

Figure 4- 13. PL spectra taken across the MoS$_2$/WS$_2$ interface. The PL spectrum was taken from Figure 4-12a starting from the inner MoS$_2$ region to the outer WS$_2$ region in 1 μm step sizes.

4.5 Concluding remarks

In conclusion, large-scale and highly crystalline MoS$_2$ and WS$_2$ monolayers as well as MoS$_2$/WS$_2$ heterostructure have been synthesized using a chemical vapour deposition process on a SiO$_2$/Si substrate. This procedure involved a solution-processed control of the precursors. The relatively small number of precursors (MoO$_3$ and WO$_3$) induces a low supersaturation level at the substrate and reduces the nucleation density, which in turn facilitates the growth of large-sized TMDC monolayers in a thermodynamically stable environment. TMDC monolayers synthesized using this strategy are found to have very large crystal sizes up to 500 μm. The high quality of the TMDC monolayers was confirmed using a combination of characterisation techniques including Raman, PL, AFM, and TEM measurements. This approach was also employed to synthesise MoS_2/WS_2 heterostructures. The small amount of metal oxide precursors enabled the synthesis of high-quality heterostructures with sharp interfaces using a one-step CVD process. The sharp interface that was achieved using this synthetic approach is attributed to the prevention of precursor-mixing due to the complete consumption of the MoO_3 precursors during the initial growth stage. The clear and sharp interface was confirmed using STEM, Raman and PL line scan measurements.

Chapter 5. Surface functionalisation of a MoS_2 monolayer

5.1. Introduction

As already discussed in the previous chapters, transition metal dichalcogenides (TMDCs) monolayers are highly suitable elements for next-generation flexible, wearable, and transparent photodetectors. It is well known that the monolayers are atomically thin (~0.7 nm) with high mechanical stability,[18, 106, 107] high mobility (1-40 $cm^2V^{-1}s$),[108, 109] desirable and large semiconducting band gap energies (1.5-2.1 eV),[1] and large exciton binding energies as well as strong light-matter-interaction[10, 110] even for monolayer thicknesses.

To date, there has been much effort directed towards improving the properties of MoS_2 phototransistors to the extent that they achieve high photosensitivity by employing a gate-field[10, 71] or larger photocurrent by modifying the electrical properties of the MoS_2 monolayer, such as doping[69, 111] and passivation.[73, 112] However, photodetectors consisting of the MoS_2 monolayer that have been synthesized using a chemical vapor deposition (CVD) method generally exhibit extremely slow response times (10-100s)[10] and thus low bandwidths, which is believed to be attributed to the long-lived trapped carriers that are particularly dominant within MoS_2 monolayers that have a large surface-to-volume ratio. Therefore, to realize their use in practical optoelectronics applications that demand a fast photoresponse time, the underlying mechanisms accounting for the photoresponse dynamics needs to be clearly elucidated so as to identify the relevant parameters that control both the sensitivity and the response time of the MoS_2 photodetector. Also, thus far, relatively little attention has been devoted to understanding the relationship between the photoresponse characteristics and the electronic energy band structure of an MoS_2 monolayer when the surface chemistry of the layer is altered.

In this Chapter, I focus on the influence of the surface-chemistry on the evolution of the charge carrier density relating to the position of the Fermi level and the energy band structure on the photoresponse behaviour in MoS_2 photodetectors. To clearly demonstrate the relationship between the carrier density, the position of the Fermi level, and the band structure, as well as the corresponding optoelectronic parameters of an MoS_2 photodetector, n-type and p-type doping were introduced into the MoS_2 channel by utilizing a self-assembled monolayer (SAM) that can effectively engineer the carrier concentrations and electronic band structure. It is found that the modification to the charge carrier density in the MoS_2 semiconducting channel and the resulting shift in the Fermi level position, as well as the bending of energy bands near the metal-semiconductor interface directly influence the optoelectronic transport that govern the sensitivity and response time of the MoS_2 photodetector.

5.2. Experimental process

5.2.1. Formation of ODTS and APTES on a MoS_2 monolayer.

The as-grown MoS_2 was surface functionalised with either Octadecyltrichlorosilane (ODTS) or (3-Aminopropyl)triethoxysilane (APTES), purchased from Sigma Aldrich, in an argon-filled glove box by dipping the samples into a solution containing 10 mL of hexane and 50 μL of ODTS/APTES. The MoS_2 samples were soaked in each solution for 2 hours and rinsed with hexane. The samples were then baked at 120 °C on a hot-plate inside the glove box as shown in Figure 5-1.

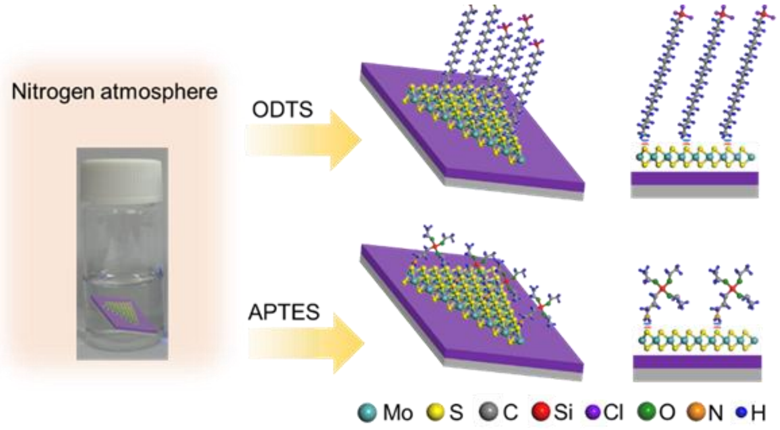

Figure 5-1. Surface functionalisation of MoS_2 monolayer. A schematic representation of the surface functionalisation of MoS_2 using ODTS ($-CH_3$) and APTES ($-NH_2$) molecules employed in this study.

For non-degenerate doping of MoS_2, the well-known self-assembled monolayers (SAM) surface functionalisation technique was implemented in our study. Of the organic molecules that are typically employed for SAMs, octadecyltrichlorosilane, (ODTS, electron withdrawing) and (3-Aminopropyl)triethoxysilane (APTES, electron donating) are well-known to effectively alter the electrical properties and carrier concentrations of TMDCs and other nanomaterials.[108, 113-115]

5.2.2. Characterisation of the doped MoS_2.

The PL and Raman measurements were performed using a 532 nm excitation source on a Jobin Yvon LabRam Aramis confocal Raman spectroscope. Laser powers of 20 μW and 1 mW were used for PL and Raman analysis, respectively. Raman spectrum was taken from 370 to 420 cm^{-1} with 1800 gratings, PL spectrum was taken from 1.6 to 2.15 eV with 600 gratings.

5.2.3. Device fabrication and measurements.

The PMMA (PMMA 950K C4, MicroChem) coated, CVD-grown MoS_2 monolayer was detached from the substrate using a 5M KOH solution. The detached MoS_2 layer was then transferred onto a 300 nm SiO_2/Si substrate. The electrode pad for the MoS_2 field effect transistor (FET) was patterned as described in Chapter 3 using e-beam lithography. The (opto)electronic properties of the fabricated MoS_2 FETs were subsequently measured using a semiconductor characterization system (4200-SCS, Keithley) with a 450 nm laser module (STAR450F5, Roithner Lasertechnik).

5.3. Raman and PL characterization

To observe and verify the modulation of the carrier density as a result of functionalisation using either ODTS- or APTES organic molecules, Raman and photoluminescence (PL) measurements were performed on the functionalised MoS_2 monolayer. Photoluminescence (PL) spectra of the pristine MoS_2 (pristine-MoS_2) monolayer and functionalised MoS_2 layers (ODTS-MoS_2 & APTES-MoS_2) were acquired experimentally as shown in Figure 5-2a. It is clearly shown that the PL spectrum (plotted in terms of electron energy rather than wavelength) of the APTES-MoS_2 layer decreased in intensity and that the peak wavelength red-shifted (15 meV), while for the ODTS-MoS_2 layer it was noticeable that there was an increase in the PL intensity and a blue-shift (11 meV) of the peak wavelength.

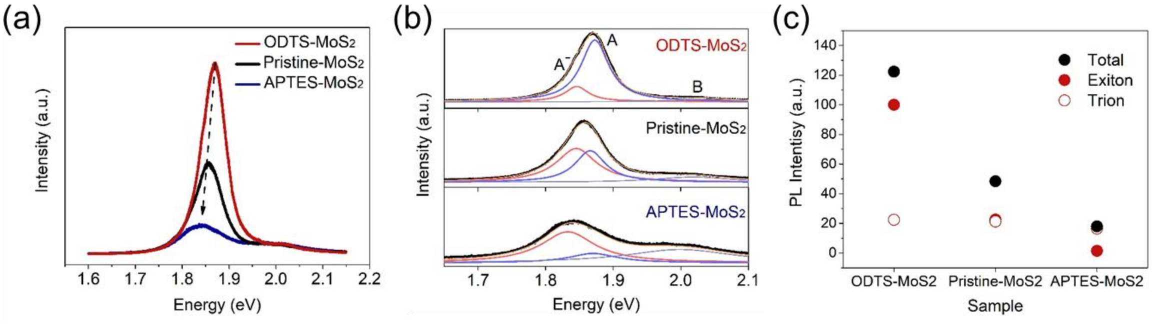

Figure 5-2. PL spectra taken from ODTS-, pristine, and -APTES-treated MoS_2. a) PL spectra taken under the excitation of a 532 nm laser source. b) Deconvolution of the PL spectra to identify the relative contributions from trions (A-), excitons (A), and B-excitons (B) by fitting with Lorentzian curves. c) The resulting intensities of the excitons and trions in the samples.

To further characterise the experimentally measured PL spectra, each spectrum was deconvoluted so that the A^- exciton (trion; 1.846 eV; red line) and A exciton (exciton; 1.874 eV; blue line) contributions could be well identified by fitting with Lorentzian curves. The intensity of each component can then be extracted from the curves (Figures 5-2b,c). It can be seen that the intensity of the trion contribution remains almost the same for all the samples regardless of the surface functionalisation process that was applied. On the other hand, the intensity of the exciton is found to increase (decrease) with surface functionalisation using ODTS (APTES) organic molecules. These results suggest that the exciton recombination was the dominant recombination process in the ODTS-MoS_2 layer, while for the APTES-MoS_2 layer the exciton recombination was largely quenched and instead trion recombination became the dominant contribution. It is well-known that the optical response of a MoS_2 monolayer is predominantly governed by the electron concentration: excess electrons tend to bind to photoexcited electron-hole pairs to generate more tightly bound trions, which lead to a significant reduction in the PL intensity.[44] The trion (A^-) recombination that is dominant in the APTES-MoS_2 layer, therefore, confirms the presence of excess electrons introduced in to the MoS_2 monolayer. Likewise, the dominant exciton peak (A) in ODTS-MoS_2 suggests that an exciton can be recombined more easily without having to form trions due to a decrease in the number of free carriers in the MoS_2 monolayer.

The functionalised MoS_2 layers were further analysed using Raman spectroscopy to assess the doping effects on the phonon vibrational modes associated with electron-phonon coupling. For the pristine-MoS_2 monolayer, the two general characteristic peaks associated with MoS_2 were observed at 381 cm^{-1} and 400 cm^{-1}, which are in accordance with the in-plane (E^1_{2g}) and out-of-plane (A_{1g}) modes, respectively, as also presented in Section 4.2.2. It is clearly observed that functionalised MoS_2 monolayers show a doping-dependence in the A_{1g} vibrational mode while there is negligible change in the E^1_{2g} vibrational mode as demonstrated in Figure 5-3a. Moreover, it was noticed that the A_{1g} mode is softened with electron doping as clearly evidenced by the increase in the full-width-half-maximum (FWHM) for the APTES-MoS_2 layer while it appears to be stiffened for the ODTS-MoS_2 layer as seen by the decrease in the FWHM (Figures 5-3b,c). The softening and stiffening of the peaks can be attributed to the effect of the carrier density on the electron-phonon coupling:[116] electron doping, which leads to the strong electron-phonon coupling, softens the A_{1g} mode by making the bonds weaker. These results are in good agreement with previous studies,[113, 116] which demonstrate that the vibrational modes of MoS_2 monolayers are dependent upon the carrier density.

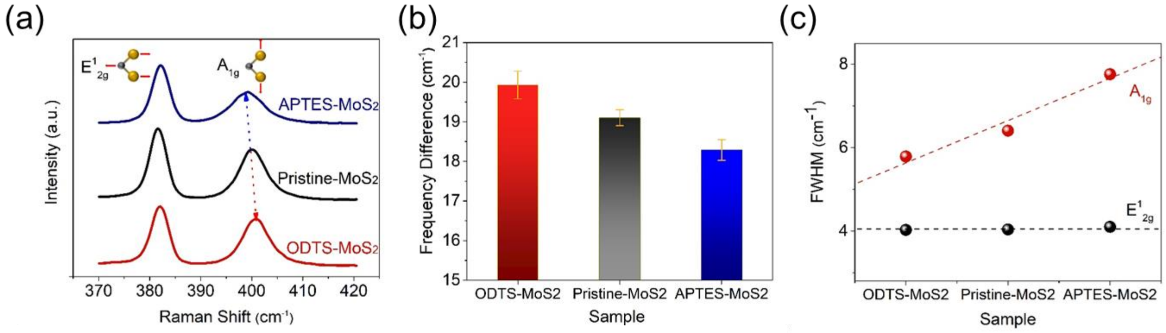

Figure 5-3. Raman spectra of pristine and functionalised MoS_2. a) Raman spectra were taken from the APTES-, pristine, and ODTS-functionalised MoS_2 monolayers. Note that the A_{1g} peak is dependent on the type of surface functionalisation. b) Differences in the Raman frequency and c) full width at half maximum (FWHM) acquired from the samples measured in a).

5.4. Functionalised MoS_2 characterisation

5.4.1. Field-effect transistor measurements

To characterize the effects of SAM functionalisation on the carrier density and charge transport behaviour, the electrical properties of MoS_2-based field effect transistors (FETs) were analysed before and after modifying the MoS_2 monolayer with either ODTS or APTES. These devices are shown in Figure 5-4a. Figure 5-4b shows the representative drain-source current, I_{ds}, as a function of the gate voltage, V_g, on a logarithmic scale at a drain voltage of V_{ds} = 0.2 V. Figures 5-5a,b, on the other hand, show the drain-source current versus drain-source voltage on a linear scale for MoS_2 FETs functionalised with either the APTES or ODTS ligands, respectively.

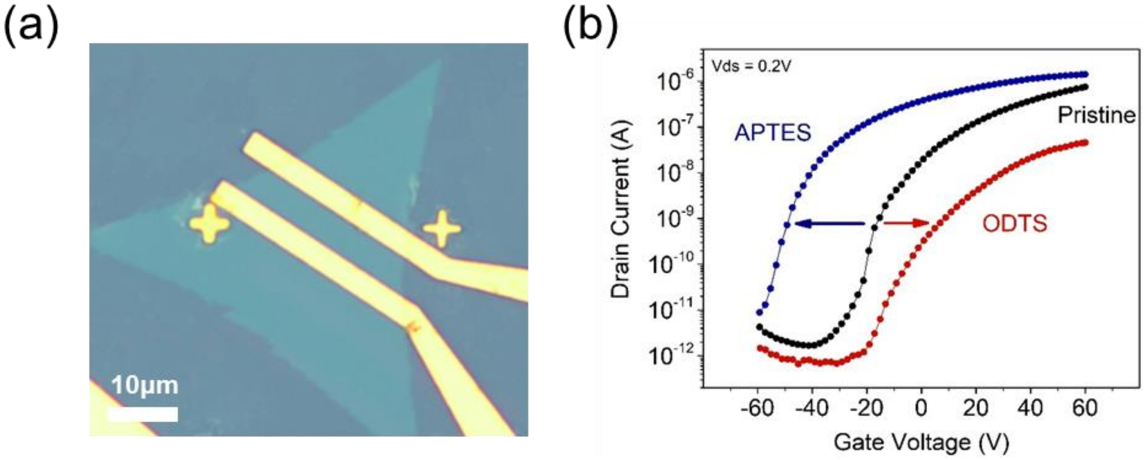

Figure 5-4. An MoS_2 FET functionalised with either ODTS or APTES. a) an optical image of a MoS_2 FET fabricated using E-beam lithography. b) Transfer curves showing the drain current as a function of the gate voltage for the APTES-functionalised (blue line), ODTS-functionalised (red line) and pristine (black line) MoS_2 FET devices at a drain voltage of 0.2 V.

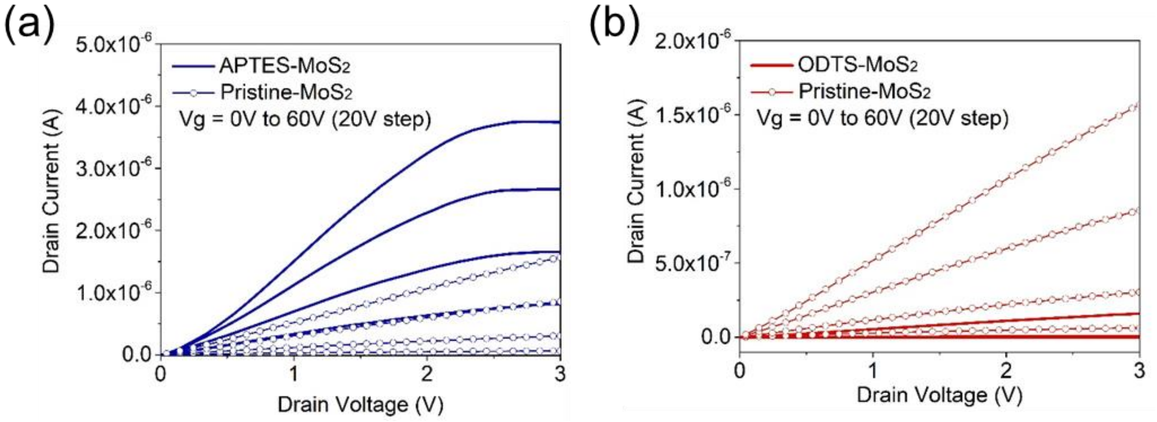

Figure 5-5. Output curves for the MoS_2-based FET functionalised with either a) APTES ligands or b) ODTS ligands. Output curves were acquired at different gate voltages ranging from 0-60 V in 20 V increments. For APTES doping, a higher conductance was measured experimentally, while a lower conductance was observed when using ODTS doping.

It can be seen that the APTES-functionalised MoS_2 FET exhibits higher conductance compared to the pristine-MoS_2 devices, while a lower conductance is measured for the ODTS-MoS_2 devices. Furthermore, it was noticed that the threshold voltages are shifted towards negative voltages for APTES-MoS_2 devices whereas it is shifted towards positive voltages for ODTS-MoS_2 devices. The resulting statistical charts of 20 control devices are summarized in Figures 5-6a,b. These findings show that the functionalised molecules employed in this study are effective in either withdrawing (ODTS) or donating (APTES) electrons to or from the MoS_2 channel, resulting in noticeable changes in the conductance of the MoS_2 channel as well as seen by changes in the threshold voltages as this is due mainly to changes in the electron concentration. We further compared the carrier density for the functionalised MoS_2 devices using the electrical results shown in Figure 5-6 along with the parallel-plate capacitor model,[113]

$$N_{doped} = \mathrm{C}|\Delta V_{th}|/e \tag{5.1}$$

where $C = \varepsilon_0 \varepsilon_r / d$ is the capacitance per unit area of a 300 nm-thick SiO_2 layer (11.5 $\mathrm{nFcm^{-2}}$), $\Delta V_{th} = V_{th,SAM} - V_{th,Pristine}$, e is the elementary charge. From these results, The N_{doped} for the APTES- and ODTS-MoS_2 devices is determined to be 1.79×10^{12} and $0.65 \times 10^{12}\mathrm{cm^{-2}}$, respectively, which is in agreement with our experimental results as well as previously reported results.[113, 114] It is evident from the modulation in the carrier density that we have successfully doped the carrier concentration of the MoS_2 channel through surface modification using either APTES or ODTS ligands

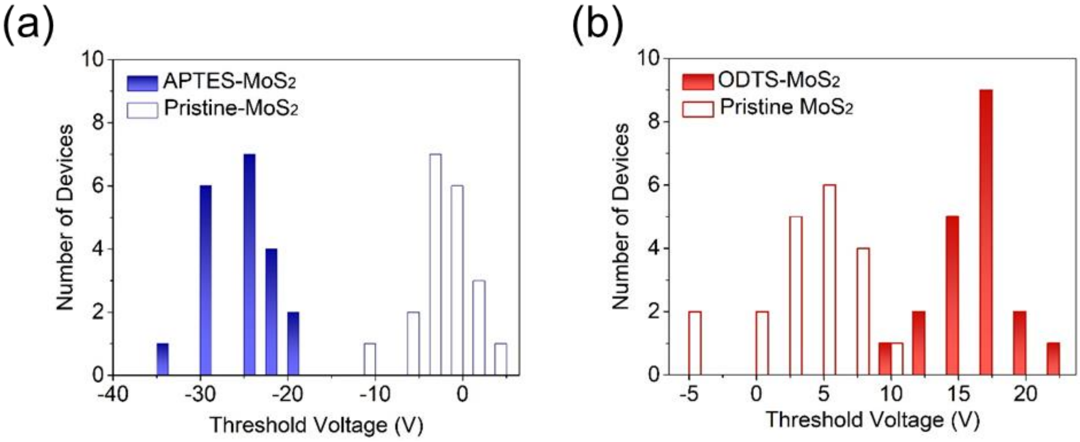

Figure 5-6. A change in threshold voltage for 20 separate control devices after a) APTES or b) ODTS functionalisation. It is shown that the threshold voltages shifted towards negative voltages for MoS_2-based FETs with APTES functionalisation whereas it was found to shift towards positive voltages for MoS_2-based FETs with ODTS functionalisation.

5.4.2. Photoresponse behaviour

In order to understand how the density of charge carriers affects the photoresponsivity and sensitivity as well as the photoresponse decay dynamics of the MoS_2 monolayer, the influence of the surface functionalisation on the optoelectronic characteristics of the MoS_2 photodetector was investigated. Figure 5-7a shows the time-dependent photocurrent measurement of the pristine and functionalised MoS_2 devices operated at $V_g = 0$ V and $V_{ds} = 1$ V under the same illumination power density of 200 nW/μm^2. The temporal responses were plotted on a logarithmic scale so that the dark current, ON current, on/off ratio, and response decay could be readily compared. The measured values of these key performance parameters are shown in Figure 5-7b.

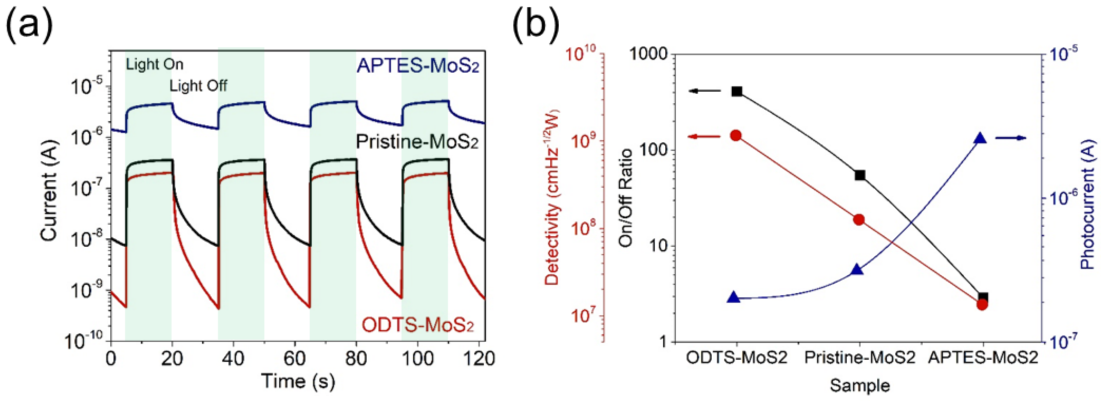

Figure 5-7. Photoresponse of the surface-functionalised MoS_2 devices compared to a control device consisting of a pristine MoS_2 device. a) Time-dependent photocurrent measurements operated at $V_g = 0$ V and $V_{ds} = 1$ V recorded under the same illumination power density of 200 nW/μm^2 and the same wavelength (450 nm). The temporal responses are plotted on a logarithmic scale. b) The photodetector parameters for the three different samples: photocurrent (secondary axis), ON/OFF current ratio (primary axis), and detectivity (primary axis), acquired from a).

5.4.3. Photoresponsivity

Compared to the pristine-MoS_2 device, the APTES functionalised MoS_2 device (higher carrier concentration) exhibited both a higher dark current (~ 1.2 μA) and ON current (~ 4.6 μA), whereas the ODTS-functionalised MoS_2 device (smaller carrier concentration) exhibited a lower dark current (475 pA) and ON current (202 nA). The photoresponsivity, $R = I_{ph}/P$, was calculated to be R = 25.2 A/W for the APTES-MoS_2 device and R = 2.5 A/W for the ODTS-MoS_2 device. These values can be further increased up to 1500 A/W and 37.5 A/W, respectively, at lower illumination intensities (Figure 5-8). Note that these values are measured at drain and gate voltage conditions of V_{ds} = 1 V and V_g = 0 V, respectively.

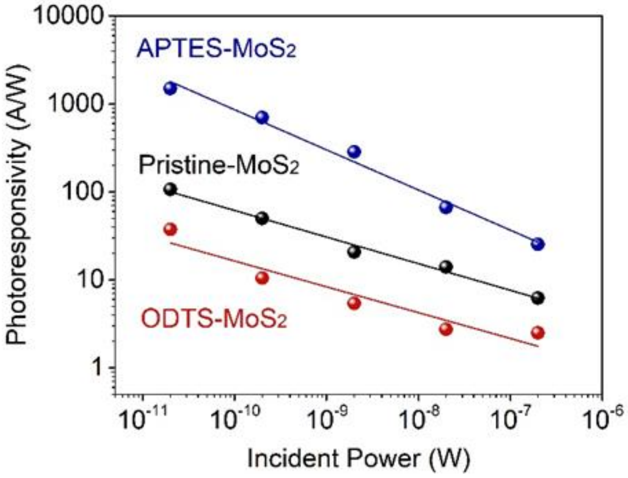

Figure 5-8. Photoresponsivity with respect to the incident illumination power for the pristine, ODTS-, and APTES-MoS_2 devices.

5.4.4. Detectivity

Even though the largest photoresponsivity was measured in the APTES-MoS_2 device, due to a negative shift in the threshold voltage, which arises from an increase in the carrier concentration, an extremely high dark current level was measured for the APTES-MoS_2 device. Therefore, in order to obtain highly sensitive photodetection, this configuration is not favourable. The detectivity $D*$ is perhaps a more representative *figure-of-merit* in characterising photodetection, which takes into account the noise of the device, device area, and bandwidth. $D*$ can be expressed as

$$D^{*} = \sqrt{AB}/NEP \tag{5.2}$$

where A is the detector area, B is the bandwidth, and NEP is noise-equivalent power, which is the minimum detectable power when the signal-to-noise is equal to unity and the bandwidth is limited to 1Hz.

Compared with the APTES-MoS_2 device, the ODTS-MoS_2 device showed a much lower dark current due to the reduced carrier density, resulting in a low channel conductance and a positive shift in the threshold voltages. However, a considerable photocurrent is still exhibited. Consequently, a much higher detectivity (2 orders of magnitude higher) of $D* = 10^9$ $\mathrm{cmHz^{-1/2}W}$ is obtained, which can be further increased up to 10^{11} $\mathrm{cmHz^{-1/2}W}$ when the illumination intensity is further decreased (Figure 5-9). Therefore, this result implies that, for sensitive photodetection, the ODTS-MoS_2 device is the more favourable configuration.

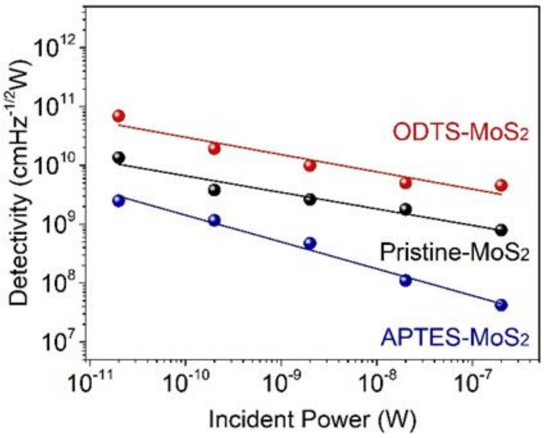

Figure 5-9. Detectivity with respect to the incident illumination power for the pristine, ODTS-, and APTES-MoS_2 devices.

5.4.5. Response time

To compare and assess the effects of surface functionalisation on the photoresponse time, all photocurrent measurements (Figure 5-10) were normalized to the maximum current values and plotted on a linear scale. From the photocurrent signal, we can clearly identify differences in the response time of the photocurrent decay. For a more detailed comparison of the response time of the APTES-, pristine, and ODTS-MoS_2 devices, each decay curve can be adequately fitted using two exponential functions expressed as

$$\mathrm{I} = I_0 + A_1 e^{-t/\tau_1} + A_2 e^{-t/\tau_2} \tag{5.3}$$

where I_0 is the photocurrent when switching off the laser and τ_1 and τ_2 are two relaxation time constants.[110, 117-119] Generally, τ_1 can be attributed to the fast response component related to instantaneous band-to-band recombination when the laser is switched off. The slow response component τ_2, on the other hand, is dominant in nanoscale materials with a large surface-to-volume ratio and depends on the existence of defects or trap states in the MoS_2 layer, which are influenced by the surroundings (e.g. underlaying substrates). For this, external factors are known to induce a significantly slow response time in a monolayer MoS_2 photodetector.[65, 120] Interestingly, both extracted relaxation constants depend considerably on the type of SAM functionalisation. Compared with the pristine-MoS_2 device ($\tau_1 = 0.27s$, $\tau_2 = 3.84s$), the APTES-MoS_2 device showed significantly larger relaxation time constants ($\tau_1 = 0.33s$, $\tau_2 = 5.29s$), while on the other hand, they were found to decrease for the ODTS-MoS_2 device ($\tau_1 = 0.25s$, $\tau_2 = 2.84s$).

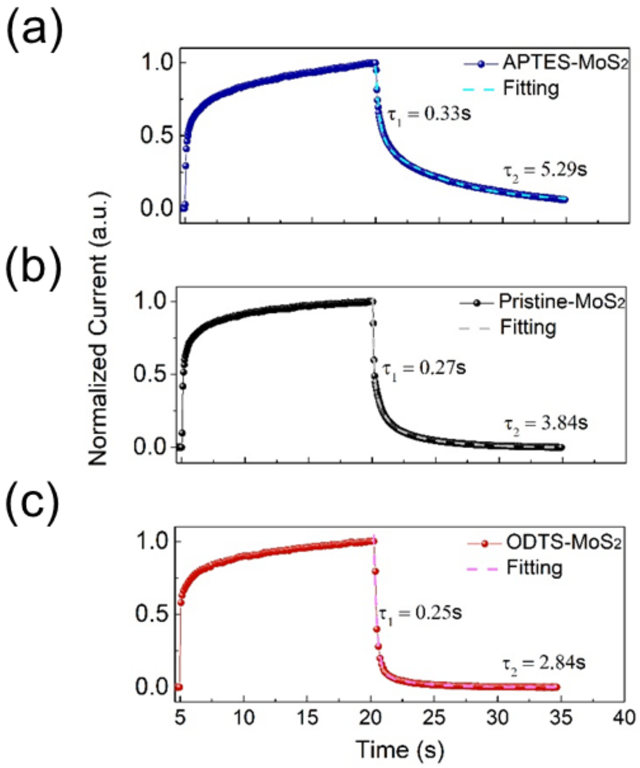

Figure 5-10. Normalized time-domain photocurrent measurements of the functionalised MoS_2 devices in comparison to the control (pristine) device. Photocurrent measurements normalized to the maximum current are presented on a linear scale so as to compare the decay curves that are fitted using a double-exponential function.

In order to help understand the SAM-mediated photoresponse behaviour that has been observed thus far, we propose the following energy band model, which is presented in Figures 5-11a,b. Depending on the nature of the functionalisation of the MoS_2 channel, the corresponding equilibrium energy band structure can be modified along with the Fermi-level position with respect to an additional increase/decrease in the carrier density of the MoS_2 monolayer. When the MoS_2 device is surface functionalised with APTES (ODTS), the position of the Fermi-level rises (falls) towards the conduction (valence) band due to an increase (decrease) in the concentration of majority carriers, consequently, giving rise to an increase (decrease) in the bending of the energy bands near the junction between the metal and semiconductor through the alignment of energy bands at equilibrium (Figure 5-11a).

For the APTES functionalised device, the increase in the bending of the energy band near the metal-semiconductor junction leads to the creation of a built-in potential, resulting in a separation of the photogenerated electron-hole pairs, as shown in the left-hand schematics of Figure 5-11b. This effect makes the direct band-to-band recombination of the electron-hole pairs more difficult and leaves excess unpaired electrons in the channel even after the laser illumination source is switched off, leading to the slow decay process of the photocurrent in the device.[121] On the contrary, for the case of the ODTS functionalised device, band bending near the metal-semiconductor interface is rather reduced compared to the pristine device, and therefore photogenerated electron-hole pairs can be easily recombined through a direct band-to-band transition. Hence, this results in a fast photocurrent decay process with a relatively small relaxation time.

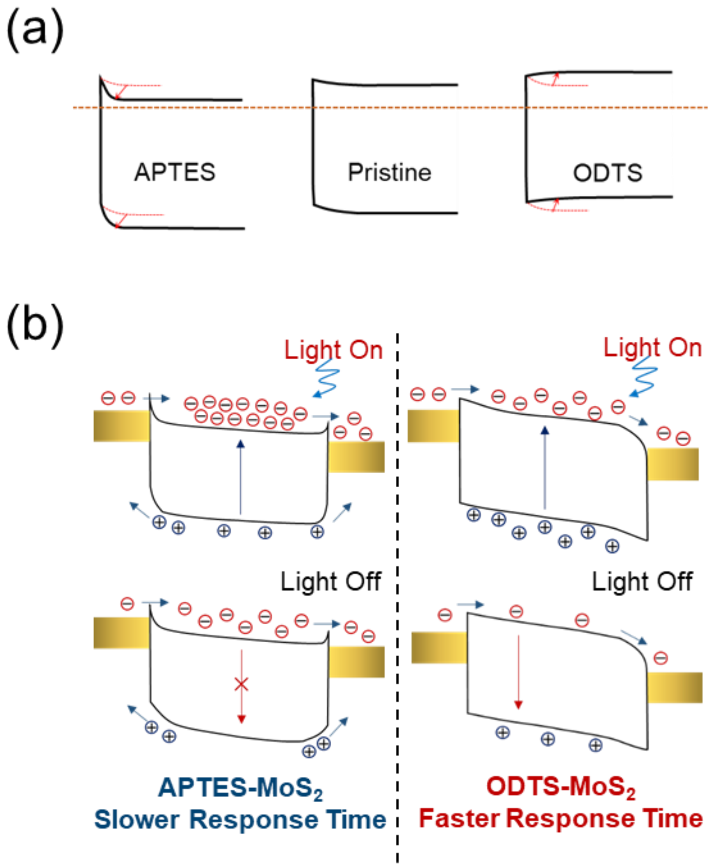

Figure 5-11. Schematic illustration of the role of energy band modulation on the photo-response decay speed.

5.5. Concluding remarks

In this chapter, the role of surface functionalization of a MoS_2 monolayer on the carrier density and subsequent photoresponse behaviour of MoS_2 photodetectors has been investigated. For the systematic study, both n-type and p-type doping were introduced into the channel by employing a self-assembled monolayer (SAM) that can effectively contribute to the engineering of the carrier concentrations and electronic band structure. It is shown that p-doping and n-doping of a MoS_2 monolayer in photodetector devices lead to distinctly different photoresponse behaviours: n-doped (APTES) MoS_2 device exhibited a slower response time and lower detectivity, whereas the p-doped (ODTS) MoS_2 device exhibited a faster response time and higher detectivity. It is found that the modification to the charge carrier density in the MoS_2 semiconducting channel and the resulting shift in the Fermi level position and bending of the energy bands near the metal-semiconductor interface directly affects the optoelectronic transport properties that govern the sensitivity and response time of the MoS_2 photodetector. The modulation of sensitivity can be attributed to the decrease/increase of carrier densities that effectively control the level of dark current, and the modulation of response time can be attributed to the bending of energy bands that controls the recombination probabilities. It is believed that the results reported here represent an important route in designing two-dimensional photodetectors by surface functionalisation and doping techniques.

Chapter 6. Strain effects on TMDC hetero-bilayer

6.1. Introduction

In addition to the modulation of the optical and electrical properties of monolayers of transition metal dichalcogenides (TMDCs) through surface functionalisation-induced doping (as shown in Chapter 5), mechanical strain can also effectively alter the electronic band structure of the TMDC crystals by changing the Mo-S distance, which is modelled in Figure 2-5 in Chapter 5. It is well-known and studied, both from theoretical[122, 123] and experimental[48, 124, 125] perspectives that strain can be used as an effective method for engineering the electronic band structure and modulating the excitonic behaviour in 2D TMDC semiconducting materials. This is because the 4d–sulphur 3p orbital interactions and hybridizations of the transition metals are easily affected in the presence of strain applied to the material.[38, 48, 49, 107, 122, 124-127] It is thus anticipated that strain engineering offers a means for designing and tailoring the unique and attractive features of 2D van der Waals materials. Along these lines, there have been many studies that have focused purely on the effect of strain effects on TMDCs monolayers (e.g. MoS_2,[48, 127] WS_2,[128] $MoSe_2$,[124] and WSe_2[125]).

Besides TMDC monolayers, heterostructures using TMDC semiconducting monolayers can also be of significant interest for both fundamental condensed matter physics and potential applications in modern (opto)electronic devices.[129-131] Recently, notable progress has been made in the development of high performance, high power, and high speed devices using semiconductor heterostructures.[15, 132-135] Moreover, to open up new avenues beyond the current limitations of conventional bulk semiconductor structures, considerable effort have been devoted to finding new semiconducting nanomaterials as well as understanding the various underlying physical phenomena that occur at the interface of a heterojunction. In this sense, TMDC monolayers allow for new heterostructure and device concepts to be created with various unique functionalities, which are particularly relevant to the development of next-generation flexible and wearable electronics/optoelectronics devices.[4, 19, 21, 129]

In this regard, two-dimensional (2D) atomic monolayers including graphene,[4, 136] hexagonal boron nitride (h-BN),[137-139] and transition metal dichalcogenides (TMDCs)[1, 8] have garnered significant attention because they can be assembled vertically so that distinctly different 2D monolayers can be integrated into van der Waals-like heterostructures with structurally abrupt and chemically clean interfaces.[140] To date, these monolayers have been stacked via transfer techniques so as to form a variety of 2D heterostructures with unique heterojunction configurations such as MoS_2/WS_2,[98, 102, 141, 142] MoS_2/WSe_2,[104, 143-145] $MoSe_2/WSe_2$,[17, 103, 146] WS_2/WSe_2,[147] and Graphene/MoS_2.[148] In each case, the heterojunction design is driven by judiciously aligning the energy bands and considering the charge transport/transfer model so that it is suitable for a range of optoelectronic devices. In particular, it has been demonstrated that hetero-bilayers of different 2D materials can preserve the fundamental properties of each individual monolayer; this means that the electronic band structure and excitonic behaviour of each individual monolayer can be made to coexist in the stacked heterostructure configuration, leading to distinct and unique physical behaviour and device performance compared to 2D homo-bilayers.[98-100]

Despite the high importance of understanding the strain-induced modulation of 2D hetero-bilayers, strain-modulation has been solely focused on TMDC monolayers, and there are no detailed accounts describing the strain-dependent evolution of the excitonic behaviour in a hetero-bilayer system. Furthermore, the relationship between the strain-induced electronic band structure transitions for two different monolayers where each individual monolayer can be affected differently when subjected to strain needs to be elucidated.

In this chapter, the uniaxial strain-mediated evolution of the phonon energy and exciton emission properties in a high quality MoS_2/WS_2 heterostructure with an epitaxial interface are investigated experimentally using Raman and photoluminescence (PL) spectroscopy. For this, a one-step epitaxial growth method is employed to obtain a clean, structurally abrupt heterojunction interface so as to eliminate any unwanted side-effects[141] such as, contamination, defects and rotational misalignments, which are often unavoidably introduced into the interface in hetero-bilayer samples that have been fabricated using a transfer stacking process. The PL emission behaviour of a MoS_2/WS_2 hetero-bilayer was directly compared to that of individual MoS_2 and WS_2 monolayers to understand the role of interlayer coupling as well as the emission properties of the hetero-bilayer.

By comparing and analysing the experimentally measured PL emission of TMDC monolayers and hetero-bilayers, we demonstrate a clear relationship between interlayer interactions and excitonic behaviour, which is closely related to the transition of the energy band structure of the MoS_2/WS_2 hetero-bilayer, and which show opposing behaviour under uniaxial tensile and compressive strain. Moreover, it is observed that the combined vibrational and emissive properties of two different monolayers in the heterostructure are modulated separately by the strain while retaining the characteristics of each monolayer.

6.2. Experimental process

6.2.1. CVD Growth of TMDCs.

Growth of the MoS_2 monolayer, WS_2 monolayer, and epitaxially-grown MoS_2/WS_2 vertical heterostructure (see Figure 6.1a) were synthesized as described in Chapter 4. It should be noted that the vertical and in-plane heterostructures were both formed on one single substrate.

6.2.2. Wet transfer of the TMDCs onto a PET substrate

The as-grown TMDC crystals on a SiO_2/Si Substrate were transferred onto a flexible PET substrate with a 125 μm thickness via a standard wet transfer process. The as-grown samples were spin coated with PMMA (950 PMMA A8), and the substrate was then baked on a hot-plate at 120 °C for 5 minutes. Afterwards, the substrate was floated on a KOH solution of 1M in order to wet etch the underlying SiO_2 substrate at 90 °C. The remaining PMMA-coated TMDC sample was finally rinsed several times in DI water and transferred onto the 1 cm × 1 cm PET substrate and baked for a further 5 minutes at 90 °C.

6.2.3. Density functional theory calculation under strain

Local density approximation (LDA) was used to model the electronic band structures of the monolayers of MoS_2 and WS_2 according to the Ceperlay Alder (CA) parameterization. The approximation model was benchmarked against the literature[39, 149] that had already calculated the strain-dependent electronic band structure of MoS_2. The lattice parameters were optimised to have a = 3.12 Å and a vacuum spacing of 20 Å was added to hinder the interaction between the periodic replicas along the c-direction. The atomic positions were relaxed until a convergence tolerance of 1×10^{-2} eV/Å and energy of 5×10^{-7} eV. A plane wave cut-off energy of 720 eV was used. Strain was induced by adding external stress to the lattice and the strain that was applied was then calculated using $\varepsilon = \frac{a - a_0}{a_0} \times 100\%$, where a is the lattice parameter of the strained monolayer and a_0 is the optimized lattice constant. To calculate the strain-induced band structures, the same optimisation process was carried out. Tensile and compressive strains of 0.8% were simulated to check the manner in which the band structure changed. It was not, however, used to prove the accuracy of the strain-induced values. With tensile strain, the calculated energy band gap was changed from 1.821 eV to 1.729 eV for MoS_2 and from 1.936 eV to 1.829 eV for WS_2. Under compressive strain, the calculated band gap is changed from 1.821 eV to 1.913 eV for MoS_2 and from 1.936 eV to 2.041 eV for WS_2. Simulations were carried out by Juwon Lee in the NST group at the University of Oxford.

6.3. Material characterisation

Figures 6-1a,b show a schematic and an optical image of the as-grown triangular MoS_2/WS_2 heterostructure, respectively, which was formed vertically during the growth process. The hetero-bilayer feature consisting of morphologically distinct MoS_2 and WS_2 monolayers was clearly identified by comparing the optical colour contrast (Figure 6-1b) and considering the AFM image which shows the height profile (Figure 6-1c), revealing that WS_2 was grown on top of the MoS_2 monolayer with AA-stacking (3R phase), also confirmed through a high angle annular dark field scanning transmission electron microscopy (HAADF-STEM) image presented in Figure 6-2. It is worth mentioning that the directly grown MoS_2/WS_2 heterostructure with an epitaxial interface is the most energetically favourable and can result in strong coupling between the monolayers.[142] This highlights the merit of our heterostructure samples over those fabricated using mechanical-transfer, which enables a more detailed understanding of the interlayer coupling in the van der Waals hetero-bilayer by circumventing contamination effects and/or rotational misalignment effects.

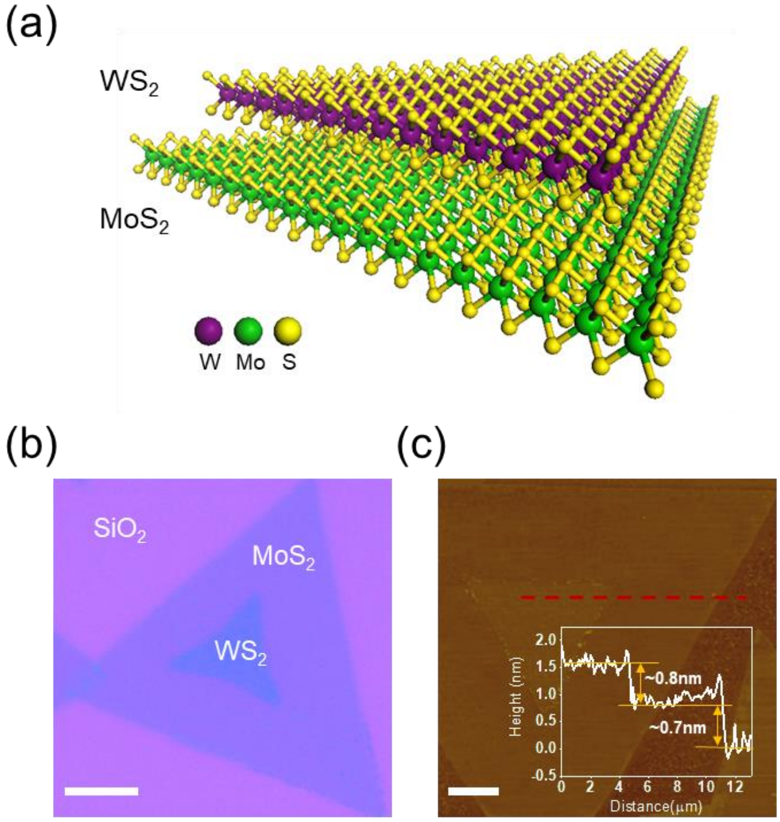

Figure 6-1. MoS$_2$/WS$_2$ vertical hetero-bilayer. a) A schematic of the MoS$_2$/WS$_2$ hetero-bilayer with WS$_2$ grown on top of MoS$_2$. b) An optical image of the hetero-bilayer on a 300 nm-thick SiO$_2$ substrate. Scale bar: 10 μm. c) An AFM topography image of the hetero-bilayer. The thickness of the monolayer of WS$_2$ and MoS$_2$ were found to be 0.8 and 0.7 nm, respectively, from the height profile (inset) at the vertical step edge of the MoS$_2$/WS$_2$ hetero-bilayer and the MoS$_2$/SiO$_2$. The AFM image was acquired by Mr. Yuljae Cho in the NST group. Figure reproduced (adapted) with permission from ref[18]. Copyright 2017 American Chemical Society.

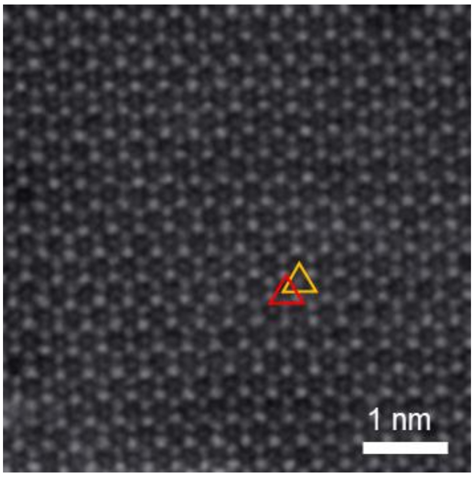

Figure 6-2. High angle annular dark field scanning transmission electron microscopy (HAADF-STEM) image of the MoS_2/WS_2 hetero-bilayer. It shows that the hetero-bilayer exhibits AA-stacking with the 3R phase. Figure reproduced (adapted) with permission from ref[18]. Copyright 2017 American Chemical Society.

The stacking order of the CVD-grown TMDCs homo-bilayers and hetero-bilayers can be discerned through relative orientation angles between the bottom layer and the top layer.[103, 142, 150, 151] Stacking angles of 0° (AA-stacking) and 60° (AB-Stacking) are most commonly observed in CVD-grown TMDC bilayers due to their energetically most stable configurations, and they correspond to the 3R and 2H phases, respectively, of the TMDCs crystals. The HAADF-STEM image of our MoS_2/WS_2 hetero-bilayer clearly shows an atomic structural configuration in the 3R crystal phase. Moreover, it is also confirmed that our hetero-bilayer has 0° stacking orientation (AA-stacking) in the 3R phase as observed through the optical image and AFM image in Figures 6-1b and c, respectively.

Raman and PL spectroscopy were performed to investigate the structural and optical properties of the as-grown hetero-bilayer. For a comparison, Raman spectra of individual monolayers and hetero-bilayer samples were measured and plotted together using a 532 nm laser with a spot size of ~1µm as shown in Figure 6-3. As expected, for the monolayer MoS_2, two typical characteristic peaks were observed at 382.8 cm^{-1} and 402.7 cm^{-1}, in accordance with the in-plane vibrational mode (E^1_{2g} mode) and the out-of-plane vibrational mode (A_{1g} mode), respectively, while for the monolayer WS_2, two strong Raman peaks located at 349 cm^{-1} and 417 cm^{-1} were observed, which can be assigned to the overlapping of the 2LA mode (longitudinal acoustic mode at the M point) with the E^1_{2g} mode and the A_{1g} mode, respectively. Unlike MoS_2, Lorentzian fitting to the peaks of the Raman spectra for monolayer WS_2 reveals that there are many second-order peaks such as the 2LA mode around 350 cm^{-1} that are much stronger than the first-order peak[33] (see Figure 4-10a, Chapter 4). The appearance of the second order peaks might be associated with the use of the 532 nm laser employed for measuring the Raman spectrum because this wavelength coincides with the B exciton peak of the WS_2 monolayer.[32, 33, 152]

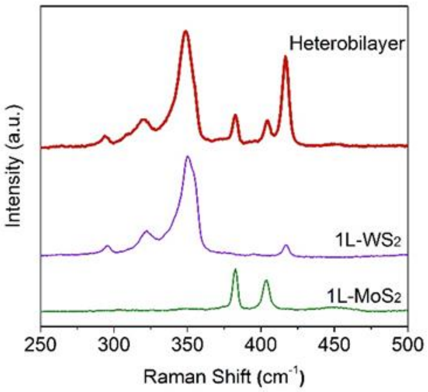

Figure 6-3. Raman spectra of the MoS_2/WS_2 hetero-bilayer and individual monolayers of MoS_2 and WS_2. For a MoS_2/WS_2 hetero-bilayer, the characteristic Raman peaks of each monolayer appear to coexist. Figure reproduced (adapted) with permission from ref[18]. Copyright 2017 American Chemical Society.

The Raman spectra of the hetero-bilayer were found to be composed of the characteristic peaks observed in the individual MoS_2 and WS_2 monolayers, implying the formation of the MoS_2/WS_2 hetero-bilayer. Interestingly, it can be seen that the intensity of the WS_2 A_{1g} peak in the heterostructure is largely enhanced. It has been reported previously that the A_{1g} peak intensity of a WS_2 monolayer increases with the numbers of layers because the intensity of the WS_2 A_{1g} mode is very sensitive to the layer thickness.[33] Thus, it is proposed that the enhancement in the intensity of the WS_2 A_{1g} peak observed here indicates the formation of the hetero-bilayer, which is consistent with the AFM results shown in Figure 6-1c. The Raman intensity mapping images of the MoS_2 A_{1g} mode peak and the WS_2 A_{1g} mode peak further confirm that the vertically-stacked heterostructure consists of distinct monolayers of MoS_2 and WS_2 as shown in Figure 6-4.

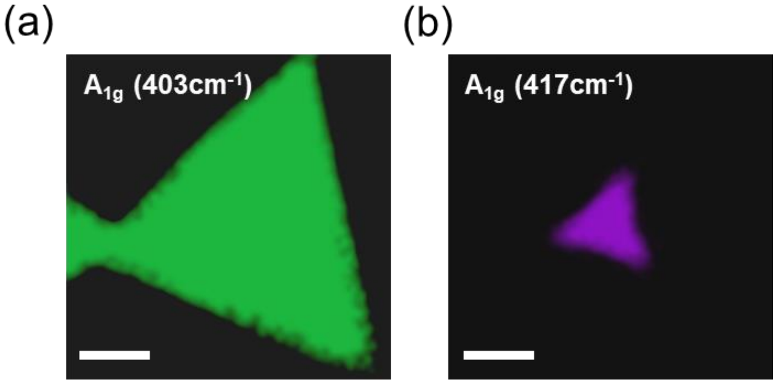

Figure 6-4. Raman intensity mapping images of a) the MoS_2 A_{1g} mode peak (peak at 403 cm^{-1}) and b) the WS_2 A_{1g} mode peak (peak at 417 cm^{-1}). These images demonstrate that the vertically stacked heterostructure consists of monolayers of MoS_2 and WS_2. Scale bars: 10 μm. Figure reproduced (adapted) with permission from ref[18]. Copyright 2017 American Chemical Society.

The PL spectra shown in Figure 6-5, which was obtained from the MoS_2 and WS_2 monolayers show strong emission peaks at their characteristic direct excitonic energies of 1.824 eV (λ = 680 nm) and 1.968 eV (λ = 630 nm), respectively. Also, the hetero-bilayer exhibits two emission peaks due to the strong coupling between the individual monolayers in the hetero-bilayer. In contrast to the monolayers, however, there is a significant reduction in the PL intensity. The reduced PL intensity can be attributed to the interlayer exciton dissociation at the interface (the separation of excited electron and hole pairs) associated with the type II heterojunction.[15, 153]

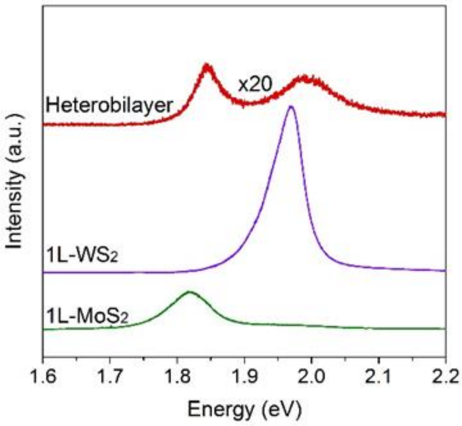

Figure 6-5. PL spectra taken from the hetero-bilayer. The PL intensity of the hetero-bilayer is noticeably decreased compared to that recorded for individual monolayers of MoS_2 and WS_2. Figure reproduced (adapted) with permission from ref[18]. Copyright 2017 American Chemical Society.

Based on the characterisations performed to confirm the MoS_2/WS_2 hetero-bilayer, the data indicates that the bi-layers are held together by Van der Waals interactions and not by a sharing of a sulphur atom (i.e. W-S-Mo link). This can be concluded as follows: the AFM height profile shows that the height of the hetero-bilayer matches exactly with the sum of the thickness of each monolayer (the thickness of the configuration S-Mo-S-W-S would be thinner than the hetero-bilayer); Raman spectra acquired from the TMDC monolayers and hetero-bilayer demonstrate lattice vibrations of X-M-X units and the D_{6h} point group symmetry,[30] - the vibration would be totally different for X-M-X-M-X units. As a result, the combined experimental evidence suggests that the layers do not consist of a W-S-Mo link.

6.4. Influence of strain on the Raman vibrational modes

To gain fundamental insight into the nature of the interlayer coupling in a vertically-stacked TMDC van der Waals hetero-bilayer, the strain-dependent evolution of the Raman spectra of the MoS_2/WS_2 hetero-bilayer has been investigated under both uniaxial tensile and compressive strain as shown in Figure 6-6. For this, the CVD-grown hetero-bilayer sample was firstly transferred onto the flexible PET substrate so that the strain-induced interlayer interaction effects, which can alter the vibrations of the phonon modes in the heterostructure, could be observed by applying a uniaxial strain using a bespoke bending experimental apparatus.

Figure 6-7 shows the strain dependence of the Raman spectra obtained from the CVD-grown hetero-bilayer sample transferred onto the PET substrate under tensile (toward red colour) and compressive (toward blue colour) strain. The applied strain was calculated using $\varepsilon = \tau / R$, where 2τ is the thickness of the PET substrate (125 μm) and R is the radius of curvature. Interestingly, it was found that the in-plane E^1_{2g} modes of the hetero-bilayer show strong phonon shifts under applied strain, while the out-of-plane A_{1g} modes of the hetero-bilayer show negligible shifts under an applied uniaxial tensile and compressive strain.

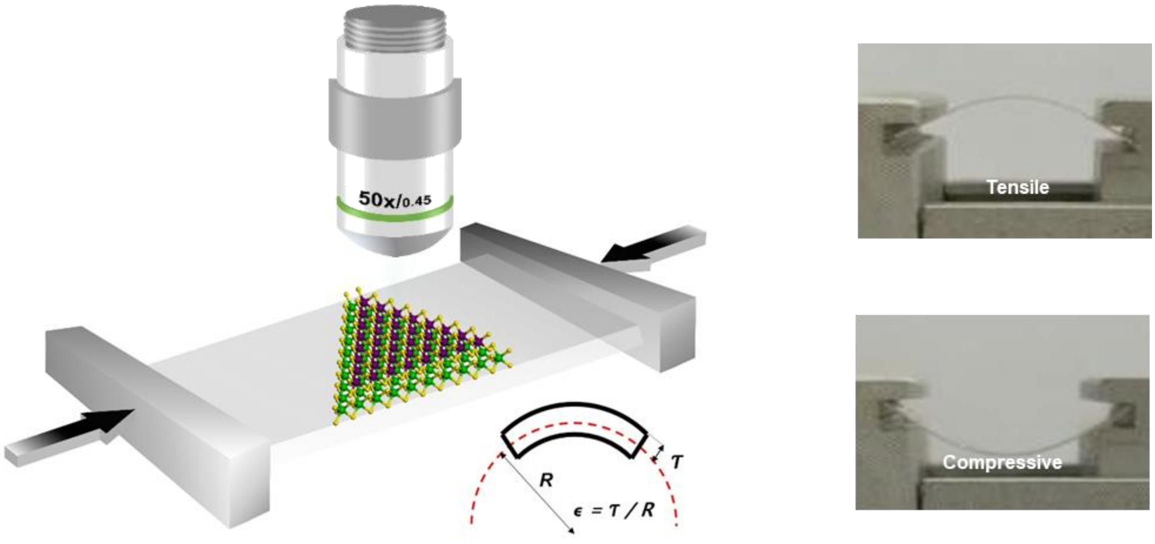

Figure 6-6. A schematic of the bending system used to strain the hetero-bilayer and measure the vibrational phonon modes. Figure reproduced (adapted) with permission from ref[18]. Copyright 2017 American Chemical Society.

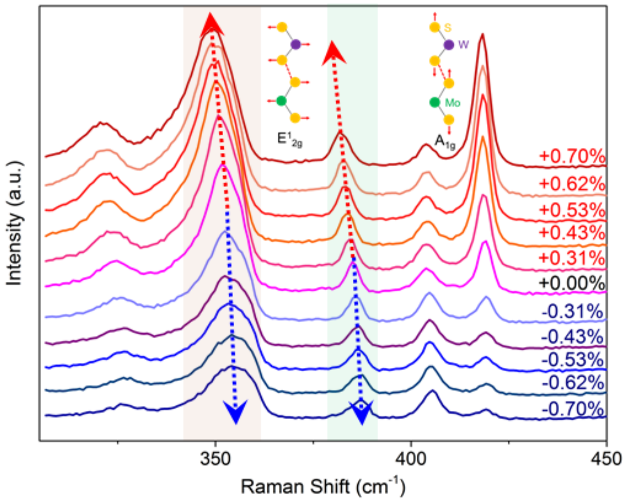

Figure 6-7. Evolution of the Raman spectra as the hetero-bilayer was subjected to strain. Strain was applied from 0% to +0.70% (toward red, tensile) and -0.70% (toward blue, compressive). Figure reproduced (adapted) with permission from ref[18]. Copyright 2017 American Chemical Society.

To further elucidate the strain-induced evolution of the phonon vibrational modes, the change in the peak positions of the E^1_{2g} modes were plotted as a function of strain (Figures 6-8a,b). Under tensile strain, the atomic bond length between the Mo(W)-S increases as the flexible substrate is bent upward so as to stretch the TMDC crystals. In this case, the in-plane vibration peaks soften as a result of a weakening of the restoring force. Under compressive strain, the converse occurs, and the in-plane vibration peaks are thus stiffened as a result of a strengthening of the restoring force. It can be seen that for an applied strain in the range of 0-0.7 %, the E^1_{2g} peak in the hetero-bilayer was found to shift linearly with strain, and from this, the linear shift rates were determined to be -4.13 and 2.63 cm^{-1} for tensile and compressive strain, respectively in MoS_2 and -5.04 and 3.71 cm^{-1} for tensile and compressive strain in WS_2, respectively. It was also observed that the frequency of the E^1_{2g} modes was more strongly affected under tensile strain than compressive strain. It is expected that the bond length of Mo(W)-S increases while the interlayer S-S distance decreases under tensile strain, and the opposite trend is expected under compressive strain, which could explain the phonon frequency softening (stiffening) in the hetero-bilayer as a result of an increase (decrease) in the lattice constant under tensile (compressive) strain.[125, 127]

The results suggest that a decrease in the interlayer distance under tensile strain induces a stronger interlayer interaction between the layers compared to that observed for compressive strain, and thus a significantly enhanced interlayer coupling between the MoS_2 and WS_2 layers can be induced. This enhanced coupling induces a strong dependence of the E^1_{2g} modes on tensile strain compared to compressive strain. Also, we note that the Raman intensity of the phonon modes in WS_2 was found to be affected by applied strain. It was previously reported that the Raman intensity of 2D TMDCs is modulated when the excitation laser energy is in resonance with the excited states of the TMDC material.[33, 154, 155] Thus, it is postulated that our observation of intensity changes in the A_{1g} and 2LA phonon modes might be associated with the interaction between the excitation laser energy and the B exciton energy of the monolayer WS_2, which is affected by strain.

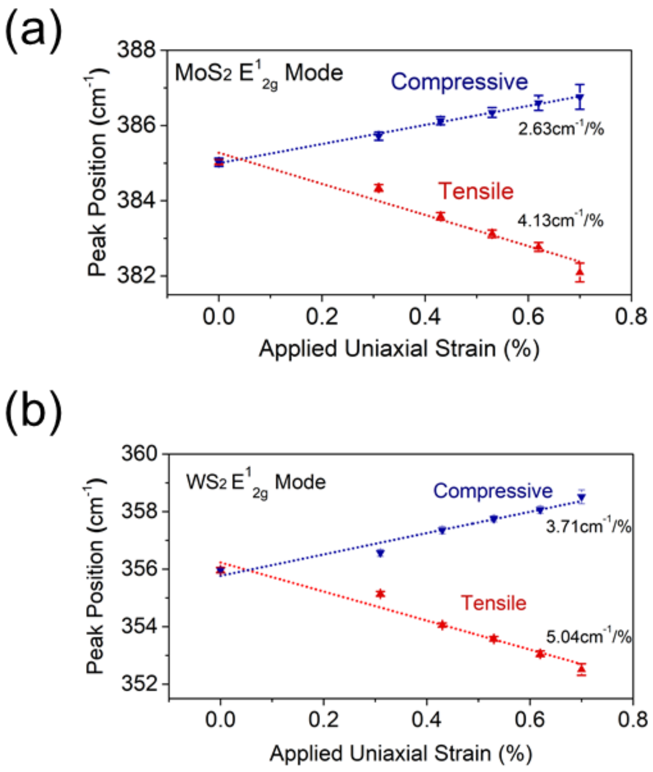

Figure 6-8. The change in the Raman in-plane E^1_{2g} mode under strain. The change was plotted for a) MoS_2 and b) WS_2 in the hetero-bilayer under uniaxial tensile (red) and compressive (blue) strain. Figure reproduced (adapted) with permission from ref[18]. Copyright 2017 American Chemical Society.

6.4. Influence of strain on photoluminescence

6.4.1. Strain-dependent PL in a hetero-bilayer

To understand in detail how the strain-modulated interlayer interaction affects the excitonic behaviour in the hetero-bilayered structure and how each monolayer plays a role in determining the resultant optical properties, in-situ strain PL measurements have been carried out to characterise the evolution of the electronic band structure of the hetero-bilayer. Figure 6-9a shows the evolution of the strain-dependent coupled PL spectra measured as a function of both tensile and compressive strain applied to the MoS_2/WS_2 hetero-bilayer. It can be seen that both the coupled PL peaks corresponding to each monolayer are modulated individually by the strain while maintaining the emission features of the hetero-bilayer. Moreover, a linear red-shift is observed (63.4 meV/% for MoS_2 and 68.4 meV/% for WS_2) and a linear blue-shift (36.3 meV/% for MoS_2 and 23.9 meV/% for WS_2) of the PL peaks with increasing tensile and compressive strain, respectively (Figures 6-9b,c). In principle, the shift in the PL spectrum can be considered to be an indicator of changes in the electronic band structure. The trends observed for the shifts in the PL peak and the sensitivity of the spectra to the strain applied to our hetero-bilayer sample are in agreement with previous theoretical calculations[122, 123] and experiments[48, 128] based on strained monolayer TMDCs, which have shown a reduction or increase in the electronic band gap. It is therefore believed that the overall optical characteristics of the MoS_2/WS_2 hetero-bilayer are dependent strongly on the evolution of the electronic band structure in each individual monolayer in the hetero-bilayer. Also, there is a correlation with PL peak shifts and Raman peak shifts because the change in the electronic band structure is a result of the change in atomic displacement which is shown through the changes in the Raman peaks. The linear and similar trend of both PL and Raman peaks of the heterobilayer indicate that each monolayer is affected individually under applied strain.

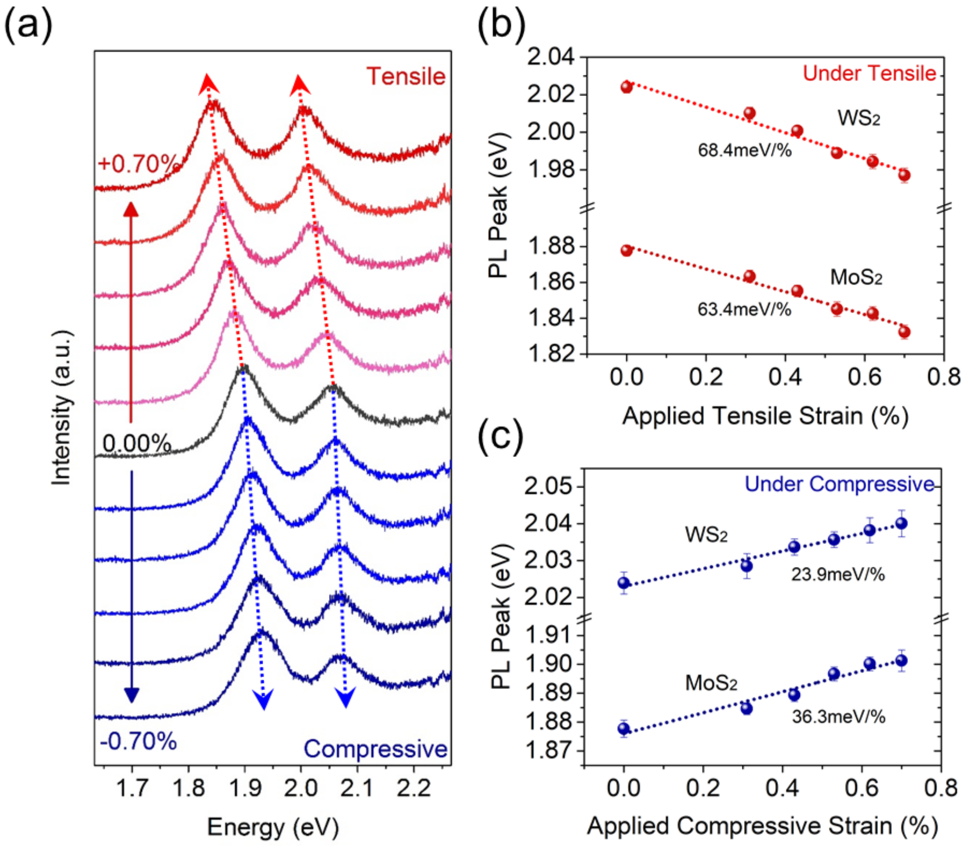

Figure 6-9. Strain-dependent emission properties of the MoS_2/WS_2 hetero-bilayer. a) Evolution of the PL spectra as the hetero-bilayer is strained from 0 % (black) to +0.7 % (toward red, tensile) and -0.7 % (toward blue, compressive). Strain-dependent PL peak position of coupled MoS_2 and WS_2 in the hetero-bilayer under uniaxial b) tensile and c) compressive strain. Figure reproduced (adapted) with permission from ref[18]. Copyright 2017 American Chemical Society.

6.4.2. Shifts of the peak in the hetero-bilayer and its monolayers

In order to further analyse the relationship between the changes in the strain-induced electronic band structure and the corresponding exciton transition behaviour in the hetero-bilayer, the change in the PL spectra of individual MoS_2 and WS_2 monolayers are compared with those of a hetero-bilayer induced by strain as shown in Figure 6-10. It is noted that while the differences in the magnitude of the shift rates of the PL peaks between the monolayer and the hetero-bilayer were not significantly noticeable under uniaxial compressive strain, tensile strain was shown to noticeably influence the emission peaks in the hetero-bilayer compared to that of the monolayers of MoS_2 and WS_2 (the shift rates for the hetero-bilayer were shown to increase by more than 20% under tensile strain compared to that under compressive strain as shown in Figure 6-10). This indicates that the interlayer interaction between the monolayers in the hetero-bilayer has a stronger impact on the electronic band structure under applied tensile strain, showing a similar trend to that observed in the strain-dependent in-plane E^1_{2g} peak in the Raman spectra.

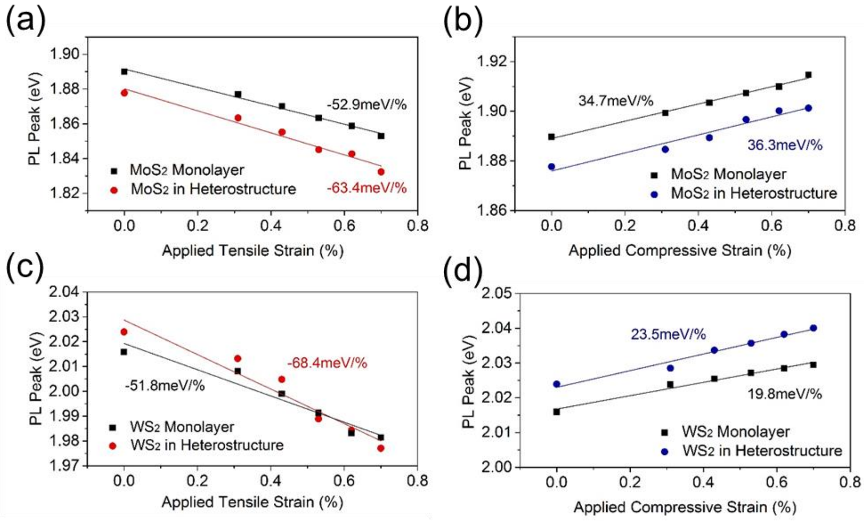

Figure 6-10. Strain-dependent shifts in the peak of the PL spectrum. The shift in the PL peak was measured in both the monolayers and the hetero-bilayer under tensile and compressive strain for a,b) MoS_2 and c,d) WS_2. Figure reproduced (adapted) with permission from ref[18]. Copyright 2017 American Chemical Society.

6.4.3. PL intensity in a hetero-bilayer and its monolayers

To clearly elucidate the mechanism underpinning the exciton transitions that are associated with the strain-modulated hetero-band structure, the PL intensity as a function of tensile and compressive strain has been investigated, which has been extracted from Figure 6-9a. Interestingly, the relative intensity ratio of WS_2 to MoS_2 in the hetero-bilayer was found to monotonically increase (up to 20%) under applied tensile strain, while under applied compressive strain the relative intensity was found to decrease (down to 7%) as shown in Figures 6-11a,b. Here, we note that the monolayer of MoS_2 (Figure 6-11a) and that of WS_2 (Figure 6-11b) show a contrasting trend in terms of the change in PL intensity under tensile and compressive strains, which is consistent with previously reported theoretical calculations and experimental demonstrations of the strain-dependent band structure evolution of monolayers of MoS_2 and WS_2.[48, 123]

When a tensile strain is applied, the PL intensity of MoS_2 is decreased, and it is increased for WS_2. In contrast, the PL intensity of MoS_2 is increased and decreased for WS_2 when a compressive strain is applied. Such behaviour originates from the transition between a direct and indirect band gap (and vice-versa), which is different in strained monolayers of MoS_2 and WS_2 and is discussed in more detail in the next sub-section (Section 6.4.4). Thus, even though the origin of the changes in the PL intensity in the hetero-bilayer is still unclear, we attribute the strain-dependent PL properties of the hetero-bilayer to a combined modulation of the band structures for each monolayer within the hetero-bilayer.

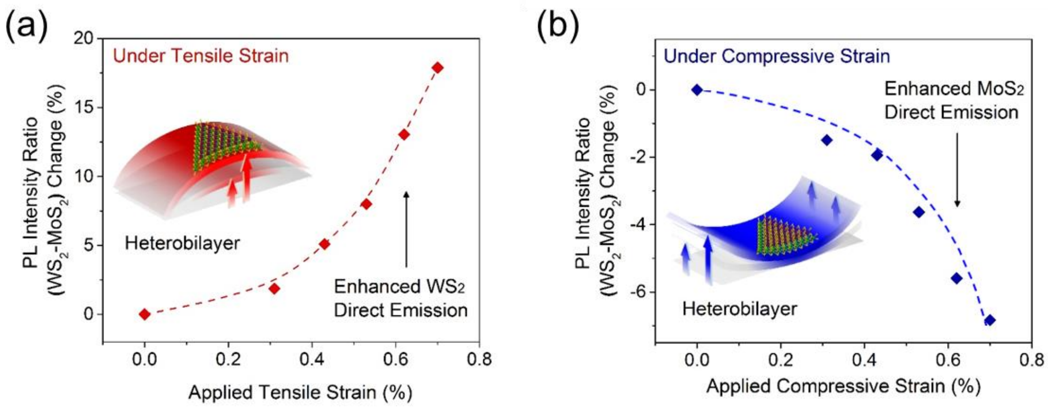

Figure 6-11. Variation in the PL intensity in the hetero-bilayer. The dependence of the WS_2 to MoS_2 PL intensity in the hetero-bilayer under a) tensile and b) compressive strain. Figure reproduced (adapted) with permission from ref[18]. Copyright 2017 American Chemical Society.

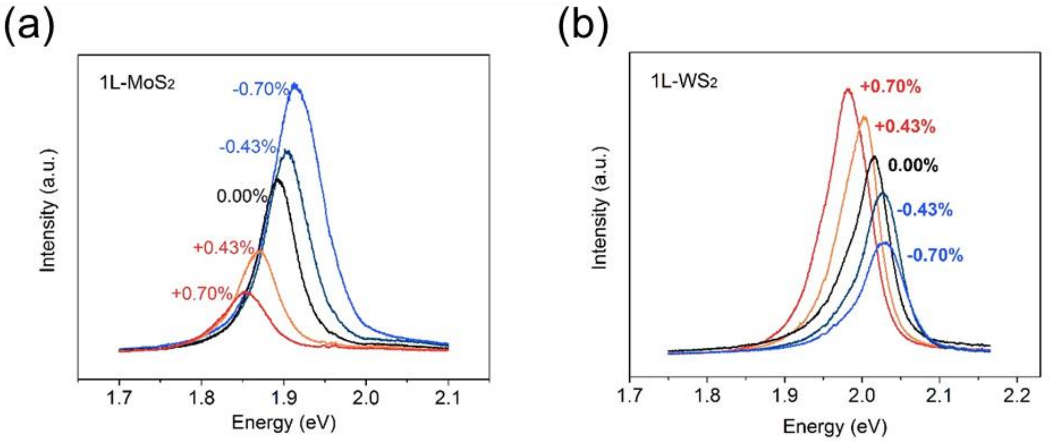

Figure 6-12. Strain-dependent PL spectra of monolayers of MoS_2 and WS_2. The positive and negative signs indicate tensile and compressive strains, respectively. Figure reproduced (adapted) with permission from ref[18]. Copyright 2017 American Chemical Society.

6.4.4. Band structure evolution of MoS_2 and WS_2 under strain

It should be noted that for single monolayer crystals, MoS_2 undergoes a direct-to-indirect band transition while for WS_2 the direct semiconducting characteristic is reinforced under tensile strain, and vice-versa under compressive strain,[48, 122, 123, 125] revealing the contrasting evolution of the band structure as depicted in Figures 6-13a,b. That is, as confirmed by theoretical and experimental studies,[48, 122] for a MoS_2 monolayer (Figure 6-13a left and 6-13b left), the transition of the band gap is predominantly governed by a change in the energy of the local valence band (VB) maxima where the indirect VB maxima at the Γ-point shifts up (down) with tensile (compressive) strain more rapidly than the direct VB maxima at the K-point. On the contrary, for a WS_2 monolayer, it is predicted theoretically[123] that under tensile strain the direct semiconducting characteristics are reinforced (Figure 6-13a right) and that it undergoes a direct-to-indirect transition under compressive strain (Figure 6-13b right). This is because the evolution of the band gap is driven by the conduction band (CB) minima of WS_2, which is changed as a result of opposite shifts in the energy at the K and K-Γ points. The interpretation of these trends is consistent with our experimental and simulation results (Figure 6-12 and Figure 6-14), showing the different dependence of the PL intensities of monolayers of MoS_2 and WS_2 on the applied strain.

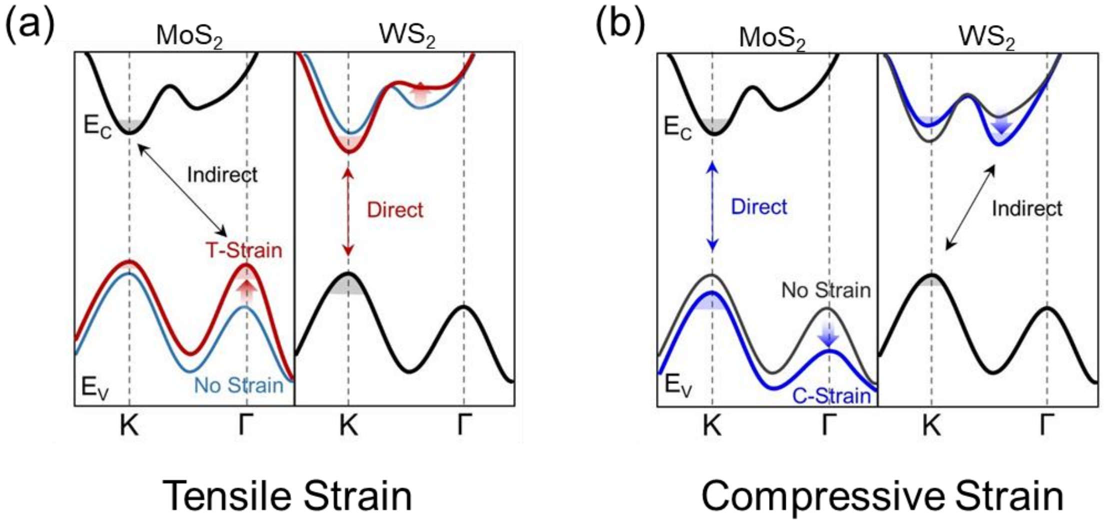

Figure 6-13. A schematic representation of the band structure under strain. The contrasting trends of the evolution of electronic band structure in monolayers of MoS$_2$ and WS$_2$ under a) tensile (red) and b) compressive (blue) strain. “direct” and “indirect” represent the direct semiconducting characteristic and direct to indirect transition, respectively. Figure reproduced (adapted) with permission from ref[18]. Copyright 2017 American Chemical Society.

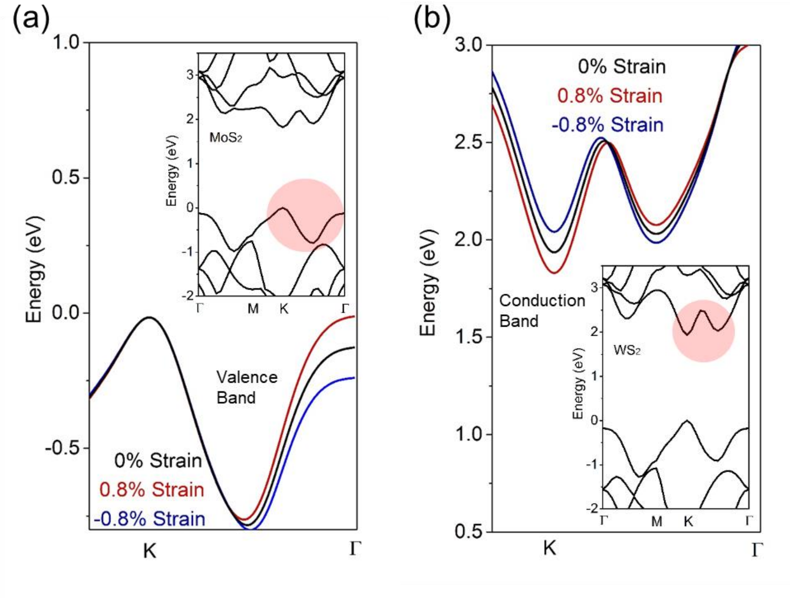

Figure 6-14. Density functional theory (DFT) calculations. The calculation further confirms clear contrasting evolution of the band structure in a) MoS_2 and b) WS_2. For MoS_2, the transition is governed by the change in the energy level of the local valence band maxima at the Γ-point, whereas for WS_2, the transition is governed by an opposite shift in the conduction band energies at the K and K-Γ points. The inset images show band structure of MoS_2 and WS_2 at zero strain. The DFT calculation was carried out by Juwon Lee in the NST group. Figure reproduced (adapted) with permission from ref[18]. Copyright 2017 American Chemical Society.

It is anticipated that the MoS_2/WS_2 hetero-bilayer retains the direct optical band gap characteristic regardless of any strain environment by complementing the PL properties of MoS_2 and WS_2 monolayers, which exhibit markedly opposing strain dependencies. In other words, the enhancement in the PL intensity for the WS_2 monolayer in the hetero-bilayer becomes dominant through the reinforcement of its direct band gap characteristics under tensile strain; while for compressive strain, the direct semiconducting nature of the MoS_2 monolayer is also relatively strengthened, leading to an enhancement in the PL intensity of MoS_2 in the hetero-bilayer. As a result, it is believed that the relative increase (decrease) in the PL intensity ratio of the WS_2 to MoS_2 monolayers in the heterostructure is attributed to an enhancement (weakening) in the PL intensity of WS_2 along with a weakening (enhancement) of the PL intensity of MoS_2 under tensile (compressive) strain. These findings suggest that the PL properties of the hetero-bilayer are different from those of a homo-bilayer formed from either MoS_2 or WS_2 and complement one another through the crossovers between a direct and indirect band gap in monolayers of MoS_2 and WS_2.

6.5. Concluding remarks

In this chapter, for the first time, strain-dependent vibrational and optical properties of a TMDC hetero-bilayer have been investigated experimentally. The strain-dependent phonon modulation, emission properties, and the complementary changes in the PL intensity of an epitaxial-grown MoS_2/WS_2 hetero-bilayer when subjected to tensile and compressive strains have been investigated in detail. For a better understanding of the hetero-bilayer, we have compared the emission behaviour with that of its constituent monolayers. Vibrational properties under strain were experimentally measured for the first time to show direct evidence of atomic strains under bending tests.

Interlayer interactions are shown to strongly affect the band structure of the hetero-bilayer, which is confirmed by the enhanced shift rates in the in-plane vibrational phonon modes and the PL emission peaks under tensile strain. Furthermore, strain-dependent PL properties were experimentally measured in the MoS_2/WS_2 hetero-bilayer. By carefully examining the strain-dependent changes in the WS_2 to MoS_2, as well as the PL intensity ratio of the hetero-bilayer and its monolayers, it is observed that the excitonic behaviour is governed by the combined evolution of the band structure of the individual monolayers of MoS_2 and WS_2, which exhibit different dependencies on the strain. These observations strongly support that strain engineering is a versatile tool with which to explore the various fundamental material properties of MoS_2/WS_2 heterostructures as well as in many other combinations of 2D van der Waals materials. It is believed that these findings are important in the understanding of electron, photon, and phonon dynamics in the heterostructures, which is of importance for the development of flexible and transparent (opto)electronics technologies.

Chapter 7. Optoelectronic device applications of TMDC monolayers

7.1. Introduction

Previous chapters were focused on the synthesis of high quality TMDC crystals and the subsequent modulation of their fundamental optical, electrical and optoelectronic properties using surface and interface engineering (Chapter 5), as well as strain engineering (Chapter 6). An understanding of these properties provides fundamental insight into optimum device design configurations for enhancing the performance of optoelectronic devices. In this chapter, two device architectures, a MoS_2/QDs hybrid-structured phototransistor and a surface-engineered MoS_2 flexible photodetector, are demonstrated. Following characterisation, experimental results highlight the benefits of developing MoS_2 crystals for optoelectronic devices.

7.2. MoS_2/PbS QDs phototransistors

7.2.1. Introduction

To enhance the performance of photodetectors based on low-dimensional materials, a phototransistor with a vertical heterojunction structure has very recently attracted notable attention as a promising device design architecture that can significantly increase the quantum efficiency of the detector. This is attributed to the fact that the new device design utilises channel materials that have high carrier mobilities for fast charge carrier transport along with strong light-absorbing semiconductors coated onto the channel that have a favourable alignment of the energy bands thus ensuring efficient carrier generation and charge transfer.[156, 157] With the recent advent of 2D materials such as graphene and MoS_2, phototransistor architectures that consist of a combination of a 2D channel material and semiconducting quantum dots have achieved unprecedented sensitivity and gain.[158] The recent development of this hybrid architecture has already been proven to be compatible with a variety of 2D channels and colloidal quantum dots.[156, 158-161] Furthermore, the 2D/QD hybrid combination has been recognised as a particularly desirable structure, associated with the thin, transparent and high mobility of the 2D structures and the extra degree of freedom in terms of the location of absorption spectrum, which arises from the tunability of optical bandgap of the QDs. Nevertheless, photogenerated carriers in the light-absorbing medium need to be transported more quickly and efficiently in a preferential direction, otherwise it can limit the overall external quantum efficiency (EQE) and response time of the detector.[158]

For 2D/QD vertical heterojunction phototransistors, a built-in potential is created at the 2D channel and QD interface only by forming a junction. Therefore, the overall performance of the vertical heterojunction photodetector is limited by the energy band alignment of the QD layers that govern the dissociation of the photogenerated excitons and diffusion of the charge carriers within the thick QD layers. As a result, an additional driving force in the heterojunction device is needed to facilitate exciton dissociation and charge transfer within the light-absorbing QD layers so as to effectively transfer photogenerated carriers into the 2D channel.

In this chapter, a built-in potential within the light-absorbing QD layers is formed that can effectively dissociate and transfer photogenerated carriers to the channel, thereby improving the overall optoelectronic performance of a phototransistor with a vertical heterojunction platform. For this work, colloidal lead sulphide (PbS) QDs and an MoS_2 monolayer were employed to demonstrate the concept of the vertical phototransistor design. The built-in potential was created by surface-modifying PbS QD layers sequentially with n-type tetrabutylammonium iodide (TBAI) and p-type 1,2-ethanedithiol (EDT), which is a well-known surface engineering strategy to create p-n junctions in PbS QDs photovoltaics.[162] Also, an MoS_2 monolayer was employed as the channel material as it can effectively transport photogenerated carriers with modulated field-effect conductivities. The efficient separation of charge carriers, which results from the electric field created by the built-in potential in the QD layers, is found to lead to an increase in the photocurrent generation as well as the photoresponsivity. Furthermore, we observe large improvements in the response time to values below 1 ms when the built-in potential is employed in the QD layers and attribute the reduced time to an enhanced charge transfer as a result of drift of electrons within the QD layers. This proof-of-concept device presents an important pathway towards designing mixed-dimensional van der Waals heterostructures.

7.2.2. Experimental process

Colloidal PbS QD Synthesis: PbS CQDs were synthesised and characterised by John Hong and Dr. Bo Hou in the NST group at the University of Oxford. PbS CQDs with an absorption peak at 953 nm (1.30 eV) were synthesised using a method developed by the NST group.[163, 164] A Pb precursor solution was prepared by mixing lead oxide (PbO), oleic acid (OA) and

1-octadecene (ODE) into a 50 mL two neck flask. The solution was heated to 100°C under vacuum for 3 hours before the heating temperature was elevated to 130°C for further treatment of the precursor solution under an argon (Ar) environment for 1 hour. A sulphur precursor solution was made by mixing hexamethyldisilathiane (TMS) and ODE in a 50 mL two-neck flask and then stirred for 4 hours at room temperature under an Ar environment. The PbS CQD synthesis was proceeded by rapid injection of the sulphur precursor solution in to the Pb precursor solution. The purification and washing steps were carried out on the solution containing PbS CQDs, and then PbS CQDs were finally dispersed in toluene at a concentration of 50 mgmL^{-1}. The synthesised PbS QDs and their optical and crystal structure were confirmed as shown in Figure 7-1 and Figure 7-2, respectively, where absorption and TEM measurements reveal the band gap energy of the resulting QDs (1.3 eV).

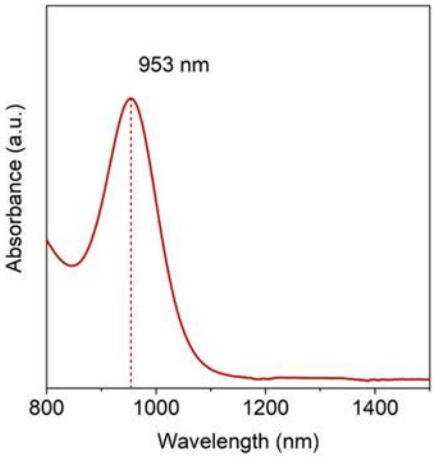

Figure 7-1. Absorption spectra of PbS QDs in toluene at a concentration of 50 mgmL^{-1} where the first absorption peak is shown at a wavelength of 953 nm. QD characterization was performed by John Hong in the NST group.

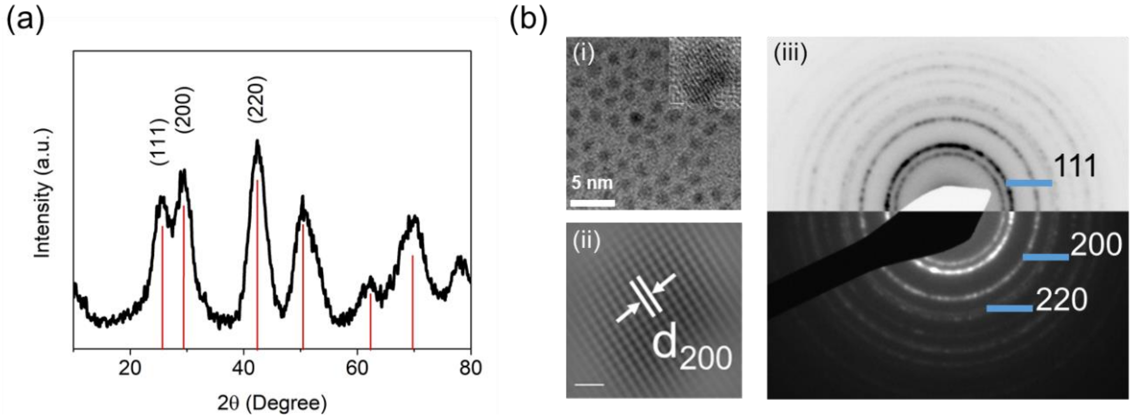

Figure 7-2. XRD spectrum and HRTEM image of an OA-passivated PbS QDs. Crystallographic characterization of the as-synthesized PbS CQDs was performed using a) X-ray diffraction (XRD), b) (i) high-resolution TEM (HRTEM), (ii) A magnified image and (iii) selected area diffraction (SAED). Scale bar for b) (ii) is 1 nm. QD characterization was performed by Dr. Bo Hou in the NST group.

Device fabrication: to fabricate the MoS_2 device, electrode contacts were drawn by a standard electron beam lithography process, followed by the sequential deposition of titanium (5 nm) and gold (45 nm) using a thermal deposition process. To fabricate the MoS_2/PbS hybrid-structured device, the solution containing PbS colloidal QD was spin-coated 6 times layer-by-layer so as to deposit the QDs onto the MoS_2 device at a spin rate of 3000 rpm. 6 layers of the TBAI-exchanged PbS QDs and 4 layers of the TBAI-exchanged PbS QDs with 2 layers of the EDT-exchanged PbS QDs were deposited by spin coating for the MoS_2/TBAI and MoS_2/TBAI/EDT devices, respectively. The thickness (Figure 7-3) was chosen to achieve optimised performance by taking in to account the diffusion length of the

PbS QDs, which is reported elsewhere.[158, 161, 165] For a solid-state ligand exchange process, a tetrabutylammonium iodide (TBAI) solution in methanol at a concentration of 10 mgmL^{-1} was dropped using a pipete on to PbS QDs for 30 seconds. A TBAI-treated CQD layer was rinsed using methanol to clean the layer. Similarly, 1,2-Ethanedithiol (EDT) at a concentration of 0.02 v/v% in acetonitrile was dropped on to a PbS CQD layer that was deposited onto the TBAI-treated CQD layer. After 30 seconds of the EDT treatment, the EDT-treated CQD layer was washed using acetonitrile twice. The spin-coating speed of 3000 rpm was used for the whole process. Characterisation of the FT-IR spectra (Figure 7-4) was performed to provide direct evidence of the removal of the oleic acid (OA) from the PbS CQDs surface via an exchange process with the EDT and TBAI ligands. The absence of the C–H (3000 cm^{-1}) and COO^{-} (1300 cm^{-1}) absorption peaks indicate that the OA that was originally on the PbS QD surface has been successfully replaced with the respective ligands (EDT or TBAI).

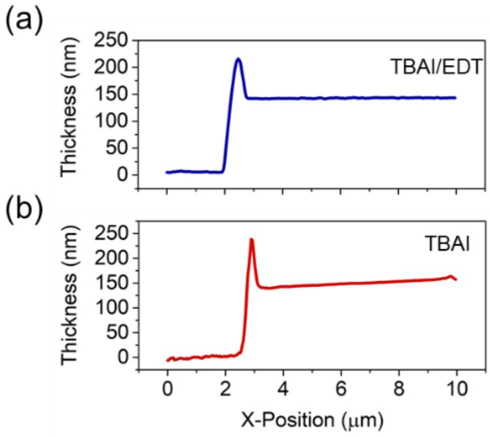

Figure 7-3. Thickness of 6 layers of spin-coated PbS QDs. a) 4 layers of TBAI-QDs and 2 layers of EDT QDs. b) 6 layers of TBAI QDs. The measured height using AFM shows the thickness of the QD layers to be around 150 nm. The AFM measurement was carried by Mr. Yuljae Cho in the NST group.

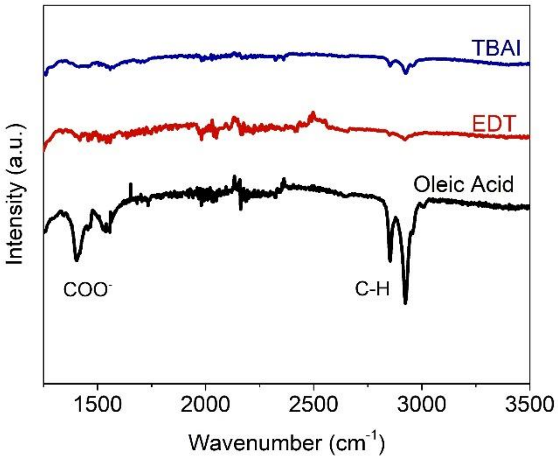

Figure 7-4. Surface analysis of the PbS CQDs passivated by Oleic Acid (Black), EDT (Red), and TBAI (Blue) using Fourier transform infrared (FT-IR) spectroscopy. The FTIR measurement was carried by Mr. Yuljae Cho in the NST group.

Figure 7-5a-c shows a schematic illustration of the hybrid structure, an optical image of the MoS_2 device, and a three-dimensional atomic force microscopy (AFM) image of the MoS_2 and PbS QDs on the SiO_2 substrate so as to clearly illustrate the vertical heterojunction device. The resulting transfer and output curves of the MoS_2 and hybrid-structured devices are analysed in Figure 7-6. The transfer curves were measured between gate voltages of -60 V to 60 V, corresponding to an electric field of 2×10^8 V/m. The pristine MoS_2 device showed excellent gate-modulated current with an on/off ratio greater than 10^6 and a calculated mobility of 3 cm^2/Vs, whereas the PbS QD-deposited MoS_2 device exhibited slightly higher current, possibly due to the transfer of charges from the PbS QD layers to the MoS_2 channel.[160]

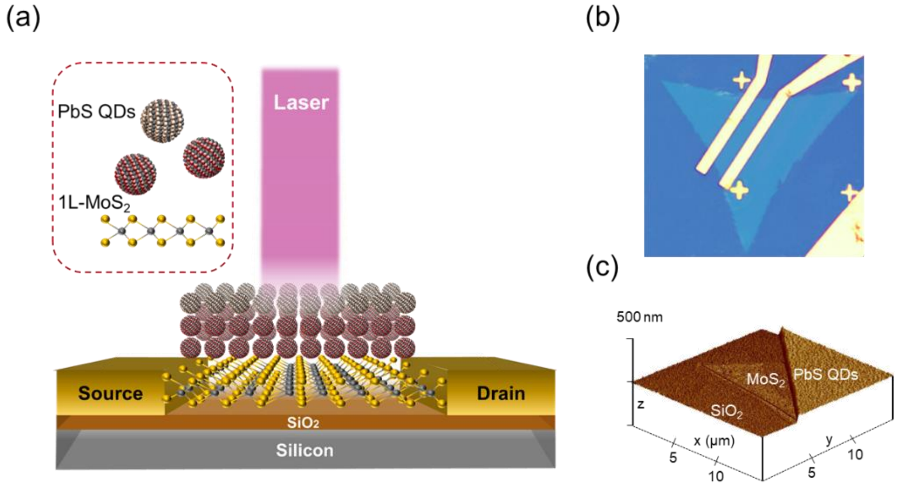

Figure 7-5. MoS$_2$/PbS QDs hybrid-structured device. a) an illustration of the hybrid-structured phototransistor. b) Optical microscope image of the MoS$_2$ device. c) 3D AFM image of the MoS$_2$/PbS QDs hybrid structure showing the 2D/0D vertical junction.

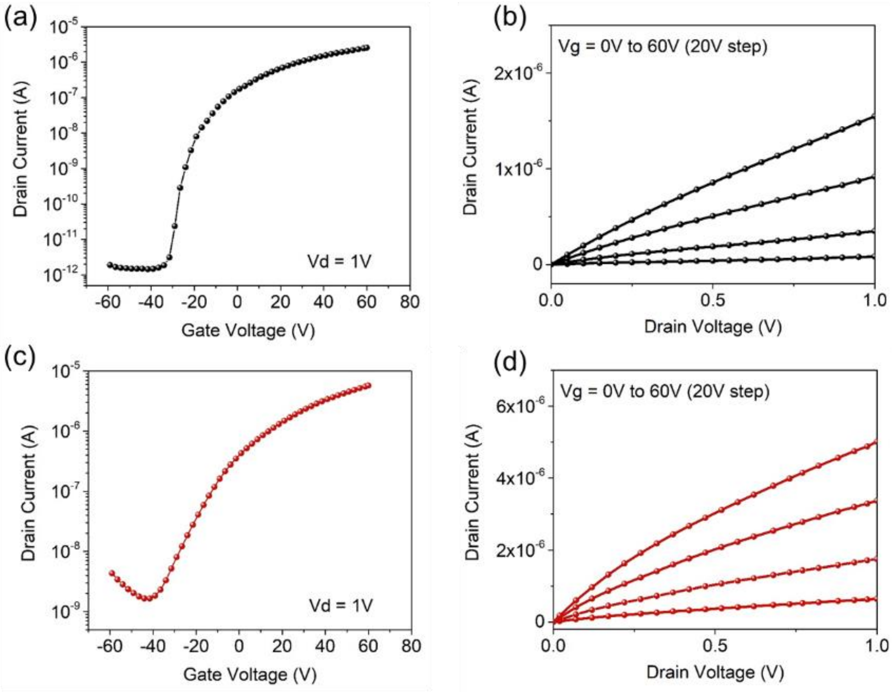

Figure 7-6. Transfer and output curves for the a,b) MoS$_2$ device and c,d) MoS$_2$/PbS QDs device. The transfer curves were measured for a drain voltage of V_d = 1 V, in both ambient and dark conditions.

7.2.3. MoS_2/QD phototransistor device design

The basic principle of the device design and concept is captured in the band alignment of the MoS_2 monolayer and the PbS QDs, as shown in Figure 7-7. A p-n junction structure has been devised to exist within the PbS QD layers and the performance of the device is compared to that of one that does not have any form of junction in the QD layers. The two-device structure includes phototransistors with (1) MoS_2 and TBAI-treated PbS QDs (TBAI-PbS) and (2) MoS_2, TBAI-PbS, and EDT-treated PbS QDs (EDT-PbS). In the first device architecture (Figure 7-7a), the built-in potential is created only at the interface between the MoS_2 channel and the TBAI-PbS QDs due to the formation of a type II heterojunction. Similarly, the second device architecture (Figure 7-7b) has the same built-in potential at the 2D/QD interface; however, another large built-in potential is formed in the QD layers when the n-type TBAI-PbS QDs and the p-type EDT-PbS QDs are aligned. Note that the thickness of the QD layers and the MoS_2/TBAI-PbS interface are identical in both cases to avoid any unintended mismatches and contamination in the two device structures.

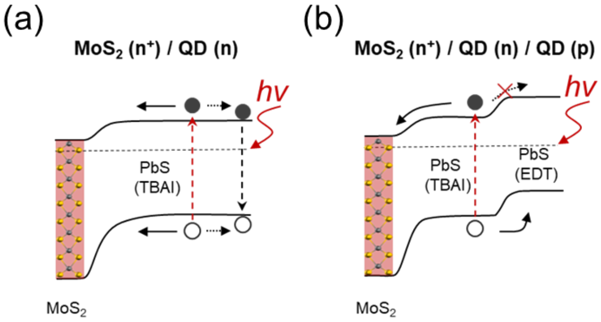

Figure 7-7. Illustration of the band alignments for the a) MoS_2/PbS-TBAI QD and b) MoS_2/PbS-TBAI/PbS-EDT QD structures.

Colloidal PbS QDs with a band gap energy of 1.3 eV were used in the fabrication of these devices. This particular QD size has been reported to efficiently absorb incident light above its bandgap and effectively modify the QD surface with either TBAI or EDT ligands (Figure 7-3).[162] To confirm the energy band alignment of the ligand-exchanged PbS QDs, the energy band levels and alignments have been investigated using ultraviolet photoelectron spectroscopy (UPS) (Figure 7-8). The measured and calculated energy levels of the TBAI-PbS and EDT-PbS QDs confirm that a large built-in potential of 0.31 eV is formed when the energy bands are aligned. Therefore, the MoS_2/TBAI-PbS/EDT-PbS device configuration can be considered as having an n^+-n-p architecture (double-junction) with a depletion region at the TBAI-PbS/EDT-PbS and MoS_2/TBAI-PbS interface, whereas the MoS_2/TBAI-PbS configuration can be considered as having an n^+-n architecture (single-junction) where the majority of the QD volume remains as a quasi-neutral region. Note that the large built-in potential in the QD layers is expected to facilitate the dissociation of excitons[158] as well as the transfer of photogenerated electrons in a preferential direction (from the QD layers towards the MoS_2 channel) with the assistance of an internal electric field.

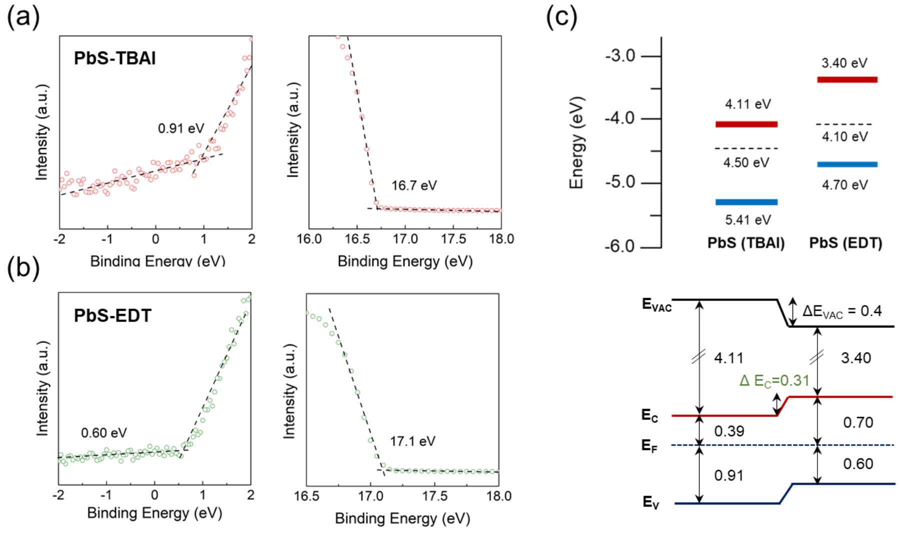

Figure 7-8. Ultraviolet photoelectron spectroscopy (UPS) measurements of PbS QDs passivated with either TBAI or EDT ligands and the corresponding alignment of the energy bands. a,b) UPS spectra of a PbS QD film treated with either TBAI or EDT ligands. The cut-off binding energy of the PbS QD film is 16.7 (17.1) eV, and this corresponds to a work function of 4.50 (4.10) eV. c) A diagram depicting the calculated energy levels of the PbS QDs treated with either TBAI or EDT ligands. The lower diagram in the figure depicts the energy band alignment for the PbS QDs treated with both TBAI and EDT ligands, confirming the presence of a large built-in potential of 0.31 eV. UPS measurements were carried by Dr. Jong Bae Park at KBSI in Korea .

In order to determine the Fermi level (E_F) and the valence band maximum (E_v) of the PbS QD layers with respect to the vacuum level, ultraviolet photoelectron spectroscopy (UPS) with a He source (21.2 eV) was employed. UPS measures kinetic energy of photoelectrons emitted by molecules under ultraviolet photon absorption. As shown in Figures 7-8a,b, the lower and upper binding energy edge are measured using UPS measurements. The work function (Ø) is then calculated by subtracting the energy of the incident photon (21.2 eV) from the binding energy of the secondary electron cut-off (high binding energy edge). The work function with respect to E_{VAC} of the TBAI-PbS and EDT-PbS QDs are calculated to be 4.50 eV (21.2 eV − 16.7 eV) and 4.10 (21.2 eV – 17.1 eV), respectively. On the other hand, E_v is determined by the difference between E_F and the lower binding energy edge measured from Figures 7-8a,b. Finally, the conduction band minimum (E_C) is calculated by adding the bandgap of the PbS CQDs (1.3 eV) to the valence band maximum. The top image of Figure 7-8c illustrates the extracted energy levels from Figure 7-8a,b whereas the bottom image illustrates the energy band diagram of a QD junction formed between the TBAI-PbS and EDT-PbS layers.

7.2.4. Enhancement in photocurrent collection

To verify an enhancement in the charge collection efficiency in our junction-controlled device, the drain-source current, I_{ds}, was measured as a function of the gate-voltage, V_g, under different illumination intensities. In this case, an 850 nm wavelength laser was employed so that light absorption occurs only in the QD layers and so that the transfer of photogenerated carriers can be carefully monitored. The total incident laser power on the effective area was estimated and calculated by considering the laser spot size (diameter 500 μm) and the device active area (200 μm^2). As shown in Figures 7-9a,b, the photocurrent $I_{Ph} = I_{Illumination} - I_{Dark}$ of the double-junction device was higher than that of the single-junction device at the same V_g, V_{ds}, and incident laser power.

To compare the difference in the band alignments for the two device architectures, the power density dependence of the photocurrent of the devices was compared at V_g = 0 V

(Figure 7-9c). In this case, the MoS_2 monolayer (E_g = 1.88 eV) does not respond under 850 nm laser illumination as shown in Figure 7-9d. At a gate voltage of V_g = 0 V, the photocurrent of the hybrid structure devices increases sub-linearly with incident laser power ($I_{Ph} \approx P^{\alpha}$, α < 1). However, this dependence is clearly increased for the double-junction device when compared to the single-junction device, with the exponent α from $I_{Ph} \approx P^{\alpha}$ increased from 0.27 to 0.36. The increase in the photocurrent as well as the value of the exponent implies that larger number of photogenerated electrons are transferred to the MoS_2 channel, and the loss of photogenerated carriers through recombination is reduced, and is believed to be due to the formation of an internal electric field in the photoactive QD layers.[158]

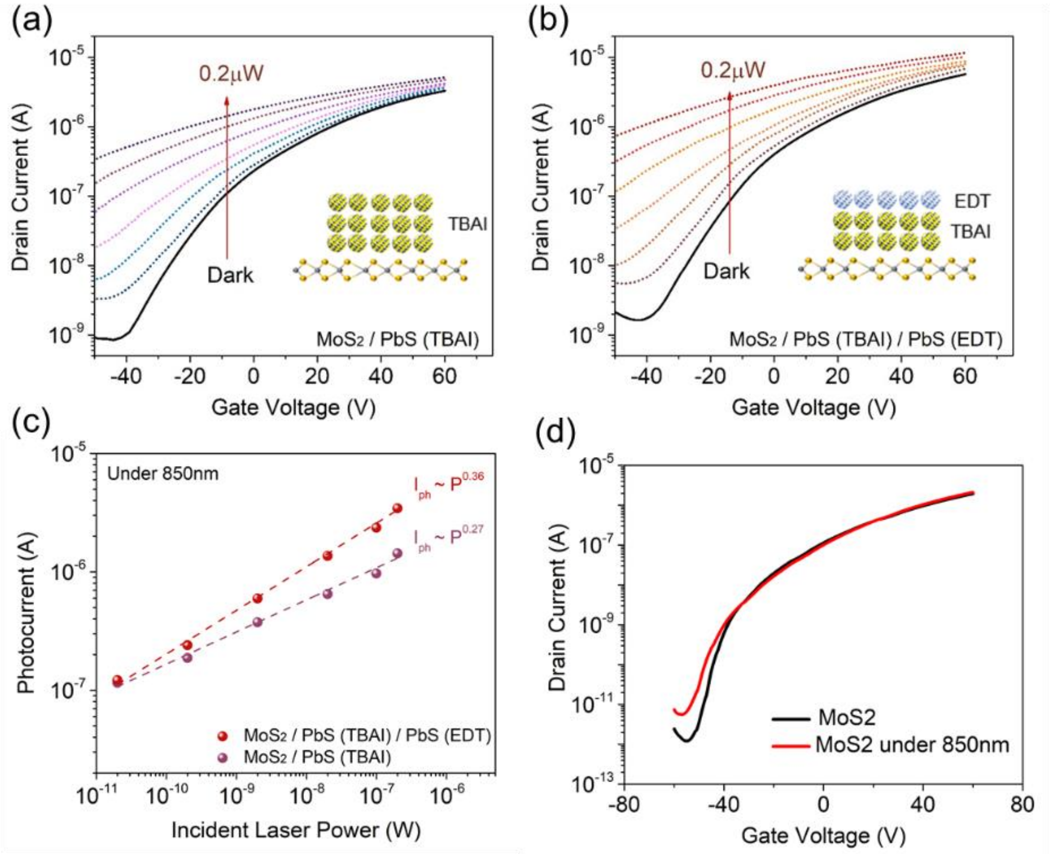

Figure 7-9. Photocurrent measurements of the MoS_2/PbS hybrid-structured device under 850 nm laser illumination and varying intensities. a,b) Measurements of the drain current as a function of gate voltage for the MoS_2/TBAI and MoS_2/TBAI/EDT devices when illuminated with an 850 nm laser at different incident intensities (dark to 200 nW). c) Photocurrent as a function of the incident laser power for the MoS_2/TBAI (purple) and MoS_2/TBAI/EDT (red) devices. The dependence of the exponent in the power-law with varying incident laser power was found to increase from 0.27 to 0.36 when an internal electric field in the QD layers was employed.

Based on the photocurrent measurements shown in Figure 7-9, the photoresponsivity and photogain can be calculated and evaluated. The photoresponsivity (R) of a phototransistor can be estimated using the equation

$$R = I_{Ph}/P \qquad (7.1)$$

where P is the incident laser power on an effective area of the device. At an incident laser power of P = 2 nW, V_g = 0 V, and V_{ds} = 1 V, the photoresponsivity was calculated to be R = 187.1 A/W for the single-junction device. However, the photoresponsivity was increased to R = 297.5 A/W for the double-junction device under the same conditions. When the laser power was substantially reduced to P = 20 pW, R was found to be 5700 and 6080 A/W for the single-junction and double-junction devices, respectively, as shown in Figure 7-10. The large photoresponsivity in our 2D/QD hybrid-structured device benefits from the type II heterojunction that is formed between the channel and the light-absorbing medium, where photoinduced excitons are spatially separated resulting in an extended lifetime; upon laser illumination, photogenerated electrons are transferred to and circulated in the MoS_2 monolayer, and photogenerated holes are trapped in the QD layers, resulting in a photoconductive gain. This gain[161, 166] can be estimated using

$$\mathrm{G} = \frac{\tau_{Life}}{\tau_{Transit}} \qquad (7.2)$$

where the value τ_{Life} = 1 ms can be extracted from the temporal response of the hybrid-structured device (Figure 7-11), and the carrier transit time $\tau_{Transit}$ can be estimated using

$\tau_{Transit} = \frac{L^2}{\mu V_{ds}} = 83\ ns$, where L is the channel length, μ is the field-effect mobility of MoS_2, and V_{ds} is the applied drain-source voltage. The carrier transit time is found to be orders of magnitude shorter than the lifetime of the carriers trapped in the QD layers, and therefore, electrons can be recirculated to achieve a photoconductive gain larger than 10^5.

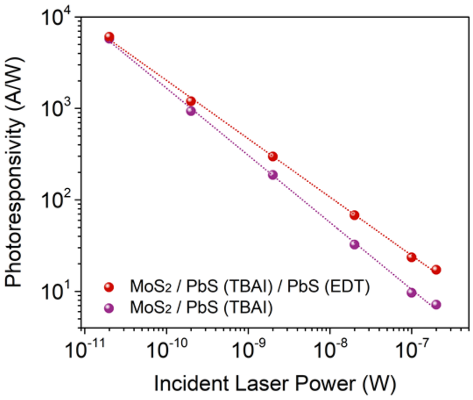

Figure 7-10. Photoresponsivity of a MoS_2/TBAI and a MoS_2/TBAI/EDT device with respect to the incident laser power.

7.2.5. Improved photoresponse time through a built-in potential

The next thing to consider is the effect of the built-in potential that exists within the QD layers on the photoresponse time. The electric field (E) created by the built-in potential in the QD layers is expected to aid the effective separation of excitons and decrease the transit time of free-carriers within the QD layers. Figure 7-11a shows a stable and repeatable temporal photoresponse for the 2D/QD hybrid-structured devices after switching the 850 nm laser illumination on and off for 1 second under bias voltages of V_{ds} = 1 V and V_g = 0 V. From the figure, we can clearly distinguish that the on-current level and rise times are different for the two devices. As demonstrated in Figure 7-9, the double-junction device shows a higher photocurrent level (increased by 50%) compared to the single-junction device. An interesting phenomenon is also observed during the off-to-on process, where we measured the rise time (10% to 90% of the dark to on-level): for the single-junction device, the photocurrent rise times are relatively slow (40 ms), whereas for the double-junction device, the photocurrent rise times are relatively quick (950 μs) and sharp before reaching a constant value.

The dramatic 42-fold improvement in the photocurrent rise time can be attributed to the drift of the dissociated excitons in the depletion region within the QD layers. In the depletion region within the QD layers, charge carriers are swept out as a drift current, leading to the initially quick rise time of the photocurrent.[167] The rise time that is enhanced through the built-in potential in the junction as it is strongly dependent on the depletion region transit time

$$\tau_{Tr,Depletion} = \frac{W_{Depletion}}{\mu_{drift}E} \tag{7.3}$$

where $W_{Depletion}$ is the depletion width, μ_{drift} is the drift mobility, and E is the internal electric field created at the TBAI-PbS and EDT-PbS junction. Therefore, it is anticipated that the transport of the charge carriers within the QD layers is dominated by the drift of carriers, rather than the diffusion of carriers, due to the wider depletion region formed through the potential differences in the device structure. The resulting rise and decay times of the double-junction device are plotted in Figure 7-11b left, with a rise time of 950 μs and a decay time of 1 ms under 850 nm laser excitation.

Such fast response times observed for the hybrid-structured device, when subjected to laser illumination at a wavelength of 850 nm, can be attributed not only to the internal electric field within the QD layers, but also to the laser excitation energy being less than the bandgap of the MoS_2 monolayer ($E_{g,MoS2}$ ~ 1.88 eV). For a pristine MoS_2 monolayer, oxygen/water adsorbates[10, 120] are generally responsible for a slow photoresponse time (1-100s) when the photon energy exceeds the electronic bandgap of the MoS_2 monolayer, as previously reported for MoS_2 photodetectors.[10, 110] This behaviour is also observed in our pristine MoS_2 and MoS_2/PbS QDs devices when a 532 nm ($> E_{g,MoS2}$) laser was used as the illumination source (Figure 7-11b, middle and right). Even though the photoresponse time decreased for the MoS_2/PbS QDs device compared to the pristine MoS_2 device under 532 nm laser excitation, there still remains a noticeable decay tail after the laser illumination is turned off. This suggest that the dominant trap-assisted photoresponse of MoS_2 can still be observed even in the hybrid-structured device. Therefore, for optimum performance of the hybrid-structured detector, the roles of the charge transporting layer and the light-absorbing medium should be decoupled.

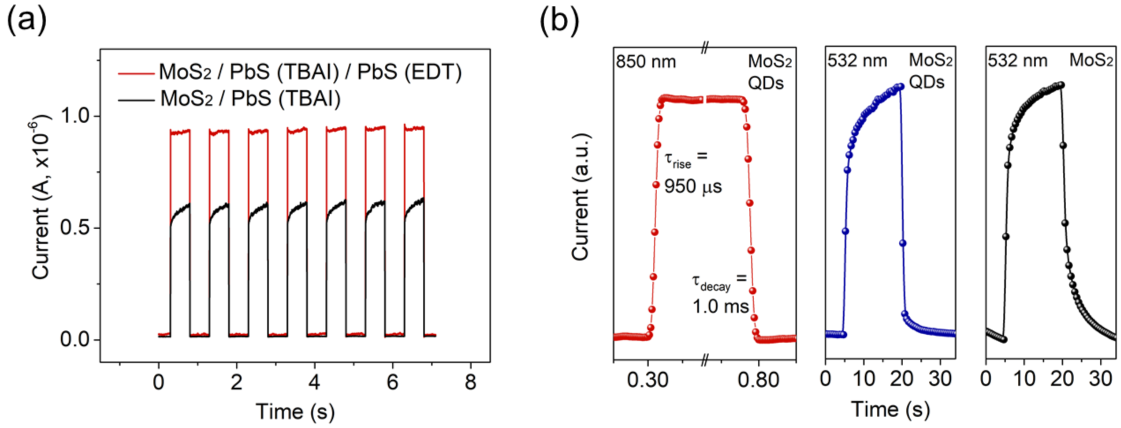

Figure 7-11. Photoresponse of the MoS_2/PbS QDs devices. a) Temporal response of the photocurrent measured for the MoS_2/TBAI and MoS_2/TBAI/EDT devices under 850 nm laser illumination with V_d = 1 V, V_g = 0 V, P_{laser} = 200 nW. b) Temporal response of the photocurrent showing a distinctly different response time when the incident energy (850 nm or 532 nm) is either smaller or larger than the bandgap of the MoS_2 monolayer.

7.2.6. Phototransistor performance

The results presented thus far demonstrate the benefits of an internal electric field that is present within the light-absorbing layers. We now turn our focus to the performance of the phototransistor with a double-junction structure. The employment of a back-gate in the phototransistor can modulate the conductivity of the MoS_2 channel as well as the overall optoelectronic performance of the device. In this device structure, the Fermi-level (E_F) of the MoS_2 channel is modulated through electrical gating. In this case, the effective Schottky barriers at the source and drain electrodes are lowered for positive back-gate voltages (accumulation regime) and are increased when negative polarity back-gate voltages are applied (depletion regime); this in turn influences the dark level and charge transport behaviour that governs the sensitivity of the detector.

Figure 7-12 presents the photoresponsivity calculated for the hybrid-structured device under various illumination intensities and gate voltages. A clear trend showing an increase in photoresponsivity is observed as the amplitude of the positive gate voltage was increased with the maximum photoresponsivity reaching $R = 5.4 \times 10^4$ A/W. This trend can be described as follows: under 850nm laser light illumination, photogenerated electrons are transferred from the QD layers to the MoS_2 monolayer. For positive polarity back-gate voltages, the Schottky barrier height between the MoS_2 channel and the source-drain electrodes is lowered,[168] and charges can then be effectively transported within the MoS_2 monolayer resulting in a higher photoconductive gain in the phototransistor. On the other hand, the transport of charges is hampered when the Schottky barrier height is increased.

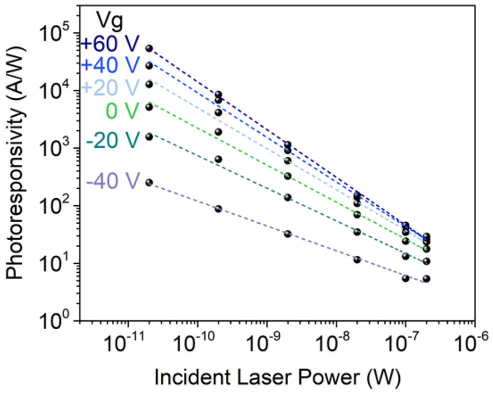

Figure 7-12. Photoresponsivity as a function of the incident laser power for different back gate voltages with a 1 V drain voltage and 850 nm laser illumination.

To evaluate and analyse the sensitivity of the phototransistor with double-junction structure, the signal-to-noise ratio (SNR) and detectivity were measured for different gate voltages as shown in Figure 7-13. The SNR was measured under an incident laser power of 200 nW. Detectivity was calculated based on the calculation described in Chapter 5. While the photoresponsivity is decreased when negative polarity gate voltages are applied, the sensitivity of the detector is largely increased, with the maximum detectivity reaching around D* = 1 × 10^{11} Jones. The improvement in the sensitivity for the negative polarity voltage regime can be attributed to the significantly reduced dark level and increased SNR. Thus, with a semiconducting MoS_2 channel in a 2D/QD hybrid-structured phototransistor, where a modulation of the gate-field is possible, the sensitivity can be enhanced by operating the device in the depletion regime.

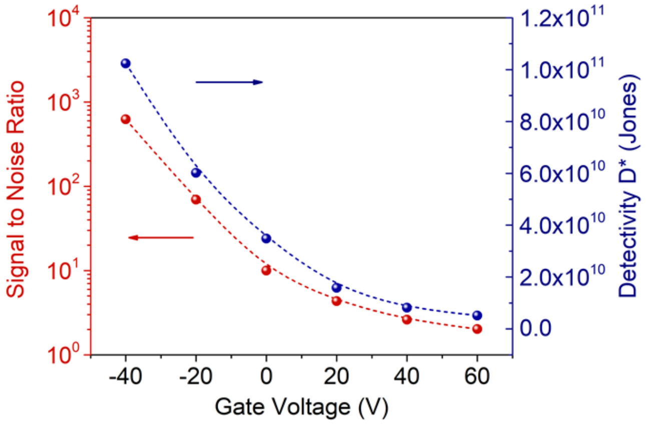

Figure 7-13. Signal-to-noise ratio (primary axis) and measured detectivity D* (secondary axis) as a function of the back-gate voltages. An optimum detectivity of more than D* = 1 × 10^{11} Jones was obtained when the device was operated with a negative polarity gate bias voltage.

The key figures-of-merit of phototransistors are compared with previously reported MoS_2 and MoS_2/QD hybrid devices in Table 7-1. For the first time, a CVD-grown mono-layered MoS_2 channel and consecutive QD junction structures have been employed into a phototransistor, which has resulted in an outstanding performance in terms of the response time, photoresponsivity, and detectivity compared to previous studies on MoS_2 and equivalent hybrid-structured photodetectors.

Table 7-1. Performance of photodetectors based on MoS_2 and its hybrid structures.

Reference	**Materials**		**Laser (nm)**	**Photoresponsivity (A/W)**	**Detectivity (Jones)**	**Rise Time (s)**	**Decay Time (s)**
Nat. Nanotechnol. 2013, 8, 497-501	Exf. 1L MoS_2		561	880	-	4	9
Adv. Mater. 2017, 29, 1702206	CVD 1L MoS_2		450	178	-	>30	
Adv. Mater. 2015, 27, 176-180	Exf. >2L MoS_2	PbS	635	10^6	5×10^{14}	-	0.35
ACS Photonics 2016, 3, 1324-1330	Exf. 1-10L MoS_2	TiO_2/PbS	635	~10^5	5×10^{12}	-	0.012
Adv. Mater. 2017, 29, 1606576	Exf. few layer MoS_2	HgTe	600 – 2000	up to 10^6	10^{12}	-	0.004
Adv. Mater. 2017, 29, 1603995	Exf. thick MoS_2	$MAPbI_3$	500	10^2-10^3	10^{11}	0.025	0.05
This work	**CVD 1L MoS_2**	**n-PbS/p-PbS**	**850**	**5×10^4**	**10^{11}**	**0.00095**	**0.001**

7.3. MoS_2 flexible photodetector

7.3.1. Introduction

Presently, there have only been a few studies on flexible MoS_2 photodetectors, [169-172] with the focus being on the fabrication process and understanding the mechanical stability of the photodetector. There is thus a need to develop an understanding in terms of designing and tailoring MoS_2-based flexible photodetectors.

Based upon the studies carried out in Chapter 5, where the surface-chemistry-mediated photoresponse of an MoS_2 monolayer was studied, the aim now is to apply this to a flexible platform. From Chapter 5, it was concluded that p-type doping induces high sensitivity and faster response time owing to a favourable bending of the energy bands to allow for direct electron-hole recombination. Based upon this concept, a simple two-terminal flexible MoS_2 photodetector is designed and demonstrated in this chapter. For this study, a basic metal-semiconductor-metal structure with Schottky barriers has been developed, which is an essential and favoured band structure required for targeting low noise and fast response speeds.

7.3.2. Experimental process

Flexible device fabrication: A polyimide solution (PI-1388, VTEC^{TM}) was coated onto a 300 nm SiO_2/Si substrate at 3000 rpm (~ 10 μm) for 60 sec, followed by sequential baking at 120 ^{o}C for 2 min, and curing at 200 ^{o}C and 325 ^{o}C for 15 min. The detached CVD-grown MoS_2 was then transferred onto a PI-coated SiO_2/Si substrate. The electrode pad for the

MoS_2 device was patterned using an electron beam lithography process, followed by the sequential deposition of gold (60nm). The device fabricated on the PI substrate was then carefully delaminated from the SiO_2 substrate and transferred onto the 125 μm Polyethylene terephthalate **(**PET) flexible substrate, and the resulting device schematics and images are shown in Figure 7-14. The device was further treated with ODTS as described in Chapter 5.

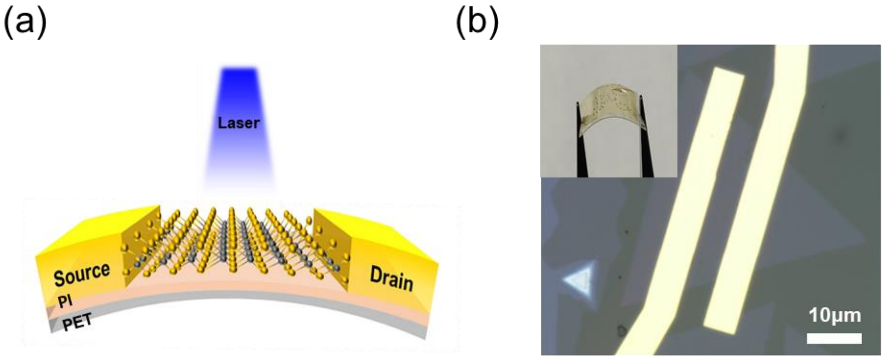

Figure 7-14. Flexible MoS_2 photodetector fabrication. a) a schematic representation and b) an optical image of a two-terminal MoS_2 flexible device fabricated using e-beam lithography.

7.3.3. Electrical measurements

The drain-source current versus drain-source voltage plotted on a linear scale for the pristine flexible device, and ODTS-functionalized device are shown in Figure 7-15. It can be clearly observed that symmetric, rectifying transport characteristics are measured for the pristine and ODTS-functionalized devices, with lower conductance observed for the ODTS-functionalized device as a result of a decrease in the electron concentration.

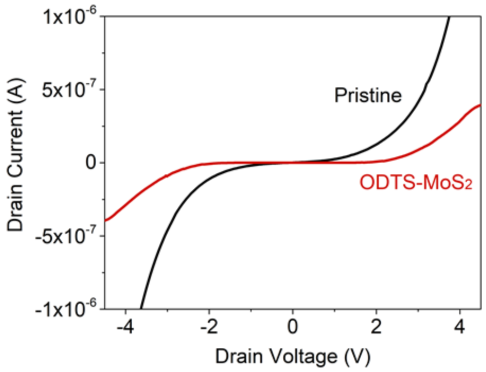

Figure 7-15. I-V curves of the flexible device and the device after ODTS treatment.

7.3.4. Flexible photodetector performance

Figure 7-16 shows the time-dependent photocurrent measurement of the ODTS-treated flexible device under 450 nm laser illumination. The device showed a highly stable and repeatable photocurrent even on the flexible platform as well as outstanding response speeds (decay time of 0.7s and rise time of 1.6s). Here, the rise and decay time were extracted from the 10% to 90% and 90% to 10% response, respectively, of the current amplitude. As expected, this photoresponse decay time is largely decreased compared to the pristine devices on the SiO_2 substrate as well as the flexible substrate (Figure 7-17) where the decay times are of the order of a few seconds. The resulting response time and device performance compare reasonably well with the literature in Table 7-2. Note that, the response time of our device is among the fastest photodetectors fabricated using a CVD-grown MoS_2 monolayer. Furthermore, this work shows, for the first time, a fast detector on a flexible platform.

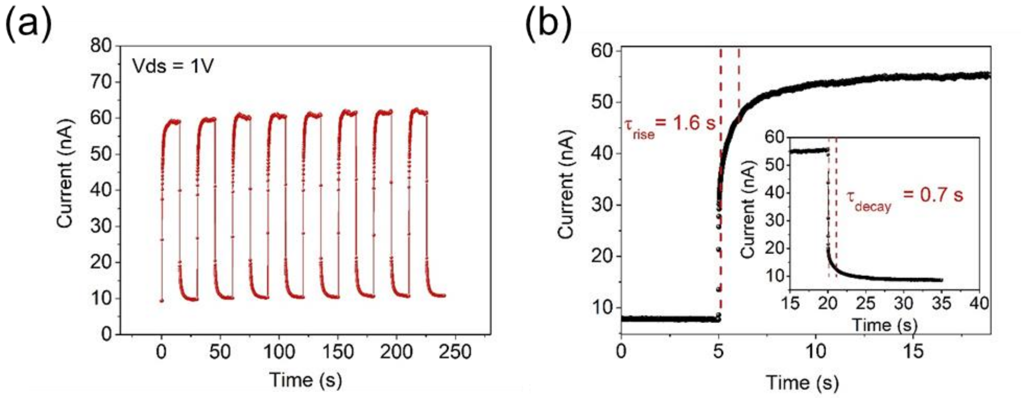

Figure 7-16. Time-dependent photocurrent measurement of ODTS-treated MoS_2 flexible device. a) Time-domain photocurrent measurements at V_{ds} = 1 V when the illumination time and off-time are repeated every 15 seconds. b) Response time acquired from the ODTS-treated MoS_2 flexible device. The inset shows the decay time.

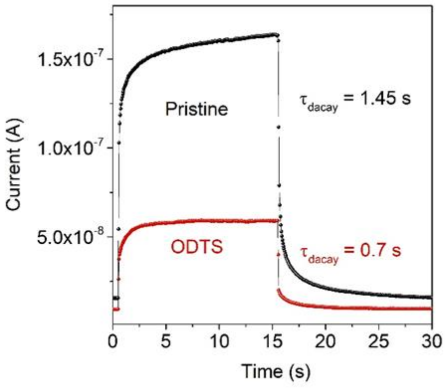

Figure 7-17. Time-dependent photocurrent measurements of a flexible MoS_2 photodetector before and after ODTS-functionalization.

Table 7-2. Summary and comparison of MoS_2 photodetectors.

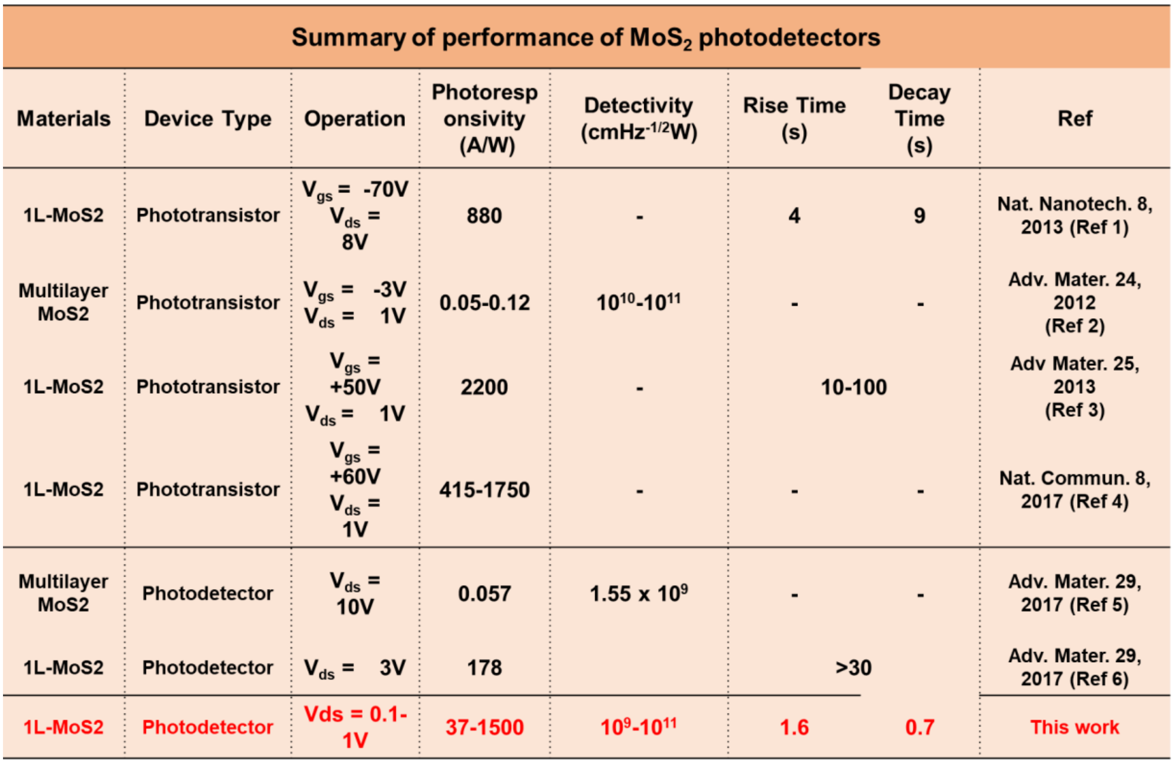

Summary of performance of MoS_2 photodetectors

Materials	Device Type	Operation	Photoresponsivity (A/W)	Detectivity (cmHz$^{-1/2}$W)	Rise Time (s)	Decay Time (s)	Ref
1L-MoS2	Phototransistor	V_{gs} = -70V V_{ds} = 8V	880	-	4	9	Nat. Nanotech. 8, 2013 (Ref 1)
Multilayer MoS2	Phototransistor	V_{gs} = -3V V_{ds} = 1V	0.05-0.12	10^{10}-10^{11}	-	-	Adv. Mater. 24, 2012 (Ref 2)
1L-MoS2	Phototransistor	V_{gs} = +50V V_{ds} = 1V	2200	-	10-100		Adv Mater. 25, 2013 (Ref 3)
1L-MoS2	Phototransistor	V_{gs} = +60V V_{ds} = 1V	415-1750	-	-	-	Nat. Commun. 8, 2017 (Ref 4)
Multilayer MoS2	Photodetector	V_{ds} = 10V	0.057	1.55 x 10^9	-	-	Adv. Mater. 29, 2017 (Ref 5)
1L-MoS2	Photodetector	V_{ds} = 3V	178		>30		Adv. Mater. 29, 2017 (Ref 6)
1L-MoS2	Photodetector	Vds = 0.1-1V	37-1500	10^9-10^{11}	1.6	0.7	This work

To investigate the mechanical stability of our MoS_2 flexible photodetector, the changes in the photocurrent and the relative values were monitored in terms of the bending radius and the number of bending cycles at an optimum bending radius, respectively, using our bespoke bending machine[18, 173] as shown in Figure 7-18. Upon bending up (tensile mode) to 2 mm of the bending radius, a photocurrent was generated with only a slight variation in the magnitude (less than 10%). Furthermore, the photocurrent generation was monitored for 1000 bending cycles at a 4 mm bending radius, and it was observed that there was less than a 20% degradation in the photocurrent for our flexible device. It should be noted that the degradation can be traced to the formation of cracks in the metal electrodes rather than a mechanical deformation in the MoS_2 monolayer because of its high Young's modulus.[106]

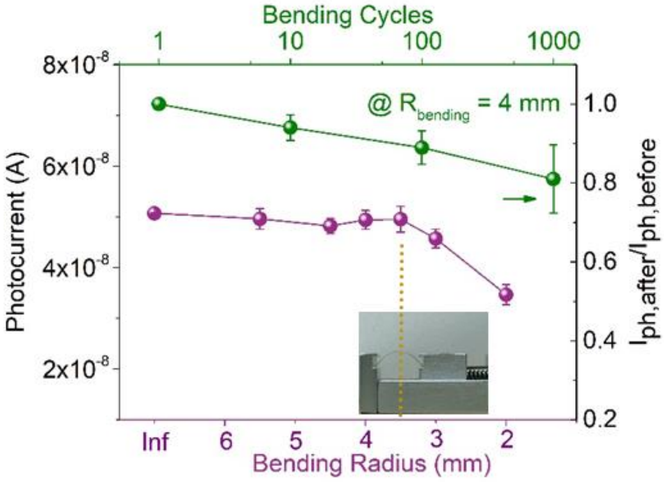

Figure 7-18. Mechanical stability test to monitor the photocurrent generation as a function of the bending radius (primary axis) and the photocurrent retention as a function of bending cycles up to 1000 at a 4 mm bending radius (secondary axis).

7.5. Concluding remarks

In this chapter, an application of an MoS_2 monolayer in an optoelectronic device application is considered. This work has demonstrated a high-performance MoS_2 photodetector using a combination of band alignment engineering and interface engineering. Firstly, a hybrid-structured phototransistor was investigated using an MoS_2 monolayer and PbS quantum dots.

This device structure can achieve high quantum efficiency by separating the roles of the light absorbing layer and charge transport layer. It has been shown that the built-in potential created within the QD layers can effectively enhance the photoresponsivity (5.4×10^4 A/W) and photoresponse time (950 μs). The enhancement in the efficient separation and transfer of photogenerated charges is due to the built-in potential. In particular, this work demonstrates an outstanding response time that is orders of magnitude shorter than that observed for previously reported 2D/QD detectors. By applying a gate field, a detectivity of the phototransistor as large as $D^* = 1 \times 10^{11}$ Jones could be obtained.

Secondly, a flexible MoS_2 device has been successfully fabricated. In this case, a fast decay time was achieved using the surface modification technique reported in Chapter 5. Moreover, this flexible device is found to be mechanically stable. The photocurrent of the device was found to be maintained up to a bending radius of 2 mm and bending cycles of 1000 at a 4 mm bending radius. The two strategies presented in this chapter offer potential routes in terms of designing high-performance MoS_2 photodetectors and flexible devices.

Chapter 8. Conclusions and future work

8.1. Conclusions

This thesis was focused on investigating semiconducting TMDC monolayers ranging from the synthesis of the materials to the characterisation/modulation of their electrical and optical properties, and to their integration in optoelectronic devices. In order to achieve these goals, I have focused on the following experiments: (1) synthesis of large-sized TMDC monolayers and their heterostructures that are grown under thermodynamically stable conditions, which are achieved through a lowering of the amount of precursors; (2) modulation of the fundamental properties through a self-assembled monolayer technique that alters the free charge carriers and through strain-engineering which can modulate the electronic band structure; (3) examples of optoelectronic device applications including a 2D/QD hybrid-structured phototransistor and an MoS_2 flexible photodetector.

The synthesis of large-sized monolayers and heterostructures was performed by loading an extremely small amount of transition metal oxide precursors. This enabled a dramatic reduction in the nucleation density of MoS_2 to be achieved, ensuring that the growth process is carried out under a thermodynamically stable environment. The TMDC monolayers grown using this method are found to exhibit large-crystal sizes and clean monolayer films, which were confirmed through direct observation using optical microscopy, PL and Raman spectroscopy, transmission electron microscopy, and atomic force microscopy. This work was extended to synthesise MoS_2/WS_2 heterostructures using a one-step growth procedure. The employment of an extremely small amount of the MoO_3 precursor led to the full consumption of the MoO_3 precursor before the WO_3 precursor begins to evaporate, resulting in the prevention of the precursor mixing as well as a clean inner MoS_2 layer and an outer WS_2 layer with a sharp interface.

Two methods have been proposed for the modulation of the fundamental properties in semiconducting TMDC layers. Firstly, a self-assembled monolayer approach has been employed to increase and decrease the charge carrier density of an MoS_2 monolayer. This was confirmed through shifts in the Raman A_{1g} mode, an increase/decrease in the PL intensity, and changes in the threshold voltages of the FETs when using an MoS_2 channel. Having confirmed the modulation of the free carrier density, a systematic investigation was carried out of the carrier density-dependent photoresponse behaviour in a photodetector based on an MoS_2 monolayer. It is found that p-type doping induces higher detectivity and faster response times owing to a reduced dark current level and an enhanced electron-hole recombination, which is achieved through a modulation of the energy bands.

Secondly, a strain-mediated modulation of the electronic band structure in an epitaxially-grown MoS_2/WS_2 hetero-bilayer has been investigated, which was directly compared with the corresponding monolayers to confirm the effects of interlayer coupling and the excitonic behaviour in a hetero-bilayer. For the first time, strain-dependent photoluminescence properties were experimentally measured in an MoS_2/WS_2 hetero-bilayer. By carefully examining the strain-dependent changes in the WS_2 to MoS_2 photoluminescence intensity ratio of the hetero-bilayer and its corresponding monolayers, we observe that the excitonic behaviour is governed by a combined evolution of the band structure of the individual monolayers of MoS_2 and WS_2, which exhibit different dependencies on the applied strain.

Based on the synthetic approach and the understanding of the fundamental properties of TMDC monolayers, optoelectronic applications of these monolayers have been presented. First, a 2D/QD hybrid structured phototransistor was demonstrated using an MoS_2 monolayer and PbS QDs that act as the charge transporting layer and light absorbing layer, respectively. To enhance the optoelectronic properties of this device, a built-in potential was employed within the QD layers through surface modification of the QD layers that led to n-type and p-type PbS QDs. As a result, an enhanced photoresponsivity and photoresponse time were observed through this novel junction-controlled device. Furthermore, by applying gate voltages to this device, the detectivity was found to extend up to 1×10^{11} Jones.

Second, a two-terminal MoS_2 flexible photodetector was fabricated to test the mechanical stability of the device and photodetector performance with respect to the mechanical strain. The self-assembled monolayer technique that was demonstrated in Chapter 5 has been successfully applied to this device in order to further decrease the response time of the flexible photodetector. It was found that the photoresponse could be maintained up to a bending radius of 2 mm and up to repeated bending cycles of 10^3 at a bending radius of 4 mm. The results for the optoelectronic devices presented in this thesis represent a significant step toward developing future photodetector technologies based on TMDC monolayers.

8.2. Future work

In this thesis, the synthesis of TMDC monolayers, the modulation of their properties, and potential optoelectronic device applications have been demonstrated. However, the research on these TMDC monolayers is still at an early stage and considerable effort is needed in order to realise practical applications of TMDC monolayers in the near future.

In terms of synthesis, a novel strategy is needed to grow single-crystalline TMDC monolayers uniformly on a wafer-scale for commercial-level manufacturability of many devices. The uniform, single crystal growth with unidirectional alignment of the seeding layers has been reported for graphene; however, it has not been successfully demonstrated for TMDC monolayers. Therefore, it is highly desirable to increase the size of the single crystalline domains and orient the nucleation and seeding layers in a single uniform direction. In order to do so, the growth of TMDC monolayers on various single-crystalline substrates (e.g. sapphire (Al_2O_3) wafer) that have similar lattice constants needs to be extensively studied, and the growth mechanism, including the nucleation behaviour, needs to be clearly elucidated.

From the point of view of the manipulation of the physical properties, much more work is needed to practically dope TMDC materials rather than doping through surface chemical functionalisation approaches. Substitutional doping can be achieved during the synthesis (e.g. incorporation of Nb or Mn) or post-synthesis approaches (e.g. electron beam induced doping or spin-on-dopant method). The resulting device performance such as threshold voltage needs to be manipulated freely as intended so that devices such as inverters can be operated with low noise. Furthermore, strain effects on TMDC monolayers and hetero-bilayers should be further studied. As presented in this thesis, a small amount of strain imparted on the monolayers can strongly affect their fundamental properties. This means that strain can significantly change the device performance of transistors/photodetectors using TMDC channels. For example, it has been theoretically predicted that when MoS_2 channel is subject to tensile strain greater than 8%, a semiconductor-metal transition is predicted.[174] Therefore, it is highly desirable to fully understand the electrical and optoelectrical properties of an TMDC monolayer under strain.

Finally, in terms of optoelectronic device applications, considerable effort is still required in order to utilise the TMDC monolayers as building blocks (e.g. photodiode, phototransistor) for practical applications. One of the major problems is the photoresponse time of TMDC monolayers. A fast response time can be achieved by investigating the passivation layer such as 2D hexagonal boron nitride or p-n heterojunction architecture. As already demonstrated in Chapter 7, the employment of PbS QDs can also significantly decrease the response time. Further study on new device architectures or employment of various QDs in 2D/QD hybrid phototransistor can also significantly decrease the response time. Besides, the dangling-bond-free surface of TMDC monolayers will be able to interact with other low-dimensional materials (e.g. 0D, 1D, and 2D) through van der Waals forces, enabling various heterostructure and integration concepts that will be able to compete with conventional technologies.

References

[1] Q. H. Wang, K. Kalantar-Zadeh, A. Kis, J. N. Coleman, and M. S. Strano, "Electronics and optoelectronics of two-dimensional transition metal dichalcogenides," *Nature Nanotechnology,* vol. 7, pp. 699-712, 2012.

[2] F. Xia, H. Wang, D. Xiao, M. Dubey, and A. Ramasubramaniam, "Two-dimensional material nanophotonics," *Nature Photonics,* vol. 8, pp. 899-907, 2014.

[3] K. S. Novoselov, A. K. Geim, S. V. Morozov, D. Jiang, Y. Zhang, S. V. Dubonos, *et al.*, "Electric field effect in atomically thin carbon films," *Science,* vol. 306, pp. 666-669, 2004.

[4] K. S. Novoselov, V. I. Fal′ko, L. Colombo, P. R. Gellert, M. G. Schwab, and K. Kim, "A roadmap for graphene," *Nature,* vol. 490, pp. 192-200, 2012.

[5] J. H. Chen, C. Jang, S. Xiao, M. Ishigami, and M. S. Fuhrer, "Intrinsic and extrinsic performance limits of graphene devices on SiO2," *Nature Nanotechnology,* vol. 3, pp. 206-209, 2008.

[6] B. Radisavljevic, A. Radenovic, J. Brivio, V. Giacometti, and A. Kis, "Single-layer MoS2 transistors," *Nature Nanotechnology,* vol. 6, pp. 147-150, 2011.

[7] A. Splendiani, L. Sun, Y. Zhang, T. Li, J. Kim, C. Y. Chim, *et al.*, "Emerging photoluminescence in monolayer MoS2," *Nano Letters,* vol. 10, pp. 1271-1275, 2010.

[8] M. Chhowalla, H. S. Shin, G. Eda, L.-J. J. Li, K. P. Loh, and H. Zhang, "The chemistry of two-dimensional layered transition metal dichalcogenide nanosheets," *Nature Chemistry,* vol. 5, pp. 263-275, 2013.

[9] W. Choi, N. Choudhary, G. H. Han, J. Park, D. Akinwande, and Y. H. Lee, "Recent development of two-dimensional transition metal dichalcogenides and their applications," *Materials Today,* vol. 20, pp. 116-130, 2017.

[10] W. Zhang, J.-K. Huang, C.-H. Chen, Y.-H. Chang, Y.-J. Cheng, and L.-J. Li, "High-gain phototransistors based on a CVD MoS_2 monolayer," *Advanced Materials,* vol. 25, pp. 3456-3461, 2013.

[11] B. Radisavljevic and A. Kis, "Mobility engineering and a metal insulator transition in monolayer MoS2," *Nature Materials,* vol. 12, pp. 815-820, 2013.

[12] T. Edvinsson, "Optical quantum confinement and photocatalytic properties in two-, one- and zero-dimensional nanostructures," *Royal Society Open Science,* vol. 5, p. 180387, 2018.

[13] M. Buscema, J. O. Island, D. J. Groenendijk, S. I. Blanter, G. A. Steele, H. S. J. van der Zant, *et al.*, "Photocurrent generation with two-dimensional van der Waals semiconductors," *Chemical Society Reviews,* vol. 44, pp. 3691-3718, 2015.

[14] F. H. L. Koppens, T. Mueller, P. Avouris, A. C. Ferrari, M. S. Vitiello, and M. Polini, "Photodetectors based on graphene, other two-dimensional materials and hybrid systems," *Nature Nanotechnology,* vol. 9, pp. 780-793, 2014.

[15] X. Hong, J. Kim, S.-F. Shi, Y. Zhang, C. Jin, Y. Sun, *et al.*, "Ultrafast charge transfer in atomically thin MoS2/WS2 heterostructures," *Nature Nanotechnology,* vol. 9, pp. 682-686, 2014.

[16] M. Massicotte, P. Schmidt, F. Vialla, K. G. Schädler, A. Reserbat-Plantey, K. Watanabe, *et al.*, "Picosecond photoresponse in van der Waals heterostructures," *Nature Nanotechnology*, vol. 11, pp. 42-46, 2016.

[17] P. Rivera, J. R. Schaibley, A. M. Jones, J. S. Ross, S. Wu, G. Aivazian, *et al.*, "Observation of long-lived interlayer excitons in monolayer MoSe2–WSe2 heterostructures," *Nature Communications*, vol. 6, p. 6242, 2015.

[18] S. Pak, J. Lee, Y.-W. Lee, A.-R. Jang, S. Ahn, K. Y. Ma, *et al.*, "Strain-Mediated Interlayer Coupling Effects on the Excitonic Behaviors in an Epitaxially Grown MoS2/WS2 van der Waals Heterobilayer," *Nano Letters*, vol. 17, pp. 5634-5640, 2017.

[19] K. S. Novoselov, A. Mishchenko, A. Carvalho, and A. H. Castro Neto, "2D materials and van der Waals heterostructures," *Science*, vol. 353, p. aac9439, 2016.

[20] D. Jariwala, T. J. Marks, and M. C. Hersam, "Mixed-dimensional van der Waals heterostructures," *Nature Materials*, vol. 16, pp. 170-181, 2017.

[21] Y. Liu, N. O. Weiss, X. Duan, H.-C. Cheng, Y. Huang, and X. Duan, "Van der Waals heterostructures and devices," *Nature Reviews Materials*, vol. 1, p. 16042, 2016.

[22] X. Chia, A. Eng, A. Ambrosi, S. Tan, and M. Pumera, "Electrochemistry of Nanostructured Layered Transition-Metal Dichalcogenides," *Chemical Reviews*, vol. 115, pp. 11941-11966, 2015.

[23] R. J. Toh, Z. Sofer, J. Luxa, D. Sedmidubsky, and M. Pumera, "3R phase of MoS2 and WS2 outperforms the corresponding 2H phase for hydrogen evolution," *Chemical Communications*, vol. 53, pp. 3054-3057, 2017.

[24] G. Eda, T. Fujita, H. Yamaguchi, D. Voiry, M. Chen, and M. Chhowalla, "Coherent Atomic and Electronic Heterostructures of Single-Layer MoS2," *ACS Nano*, vol. 6, pp. 7311-7317, 2012.

[25] H. Huang, Y. Cui, Q. Li, C. Dun, W. Zhou, W. Huang, *et al.*, "Metallic 1T Phase MoS2 Nanosheets for High-Performance Thermoelectric Energy Harvesting," *Nano Energy*, vol. 26, pp. 172-179, 2016.

[26] Y. Guo, D. Sun, B. Ouyang, A. Raja, J. Song, T. F. Heinz, *et al.*, "Probing the Dynamics of the Metallic-to-Semiconducting Structural Phase Transformation in MoS2 Crystals," *Nano Letters*, vol. 15, pp. 5081-5088, 2015.

[27] R. Kappera, D. Voiry, S. E. Yalcin, W. Jen, M. Acerce, S. Torrel, *et al.*, "Metallic 1T phase source/drain electrodes for field effect transistors from chemical vapor deposited MoS2," *APL Materials*, vol. 2, p. 092516, 2014.

[28] A. Molina-Sánchez and L. Wirtz, "Phonons in single-layer and few-layer MoS2 and WS2," *Physical Review B*, vol. 84, p. 155413, 2011.

[29] H. Li, Q. Zhang, C. Yap, B. Tay, T. Edwin, A. Olivier, *et al.*, "From Bulk to Monolayer MoS2: Evolution of Raman Scattering," *Advanced Functional Materials*, vol. 22, pp. 1385-1390, 2012.

[30] X. Zhang, X. F. Qiao, W. Shi, J. B. Wu, D. S. Jiang, and P. H. Tan, "Phonon and Raman scattering of two-dimensional transition metal dichalcogenides from monolayer, multilayer to bulk material," *Chemical Society Reviews*, vol. 44, pp. 2757-2785, 2015.

[31] C. Lee, H. Yan, L. E. Brus, T. F. Heinz, J. Hone, and S. Ryu, "Anomalous lattice vibrations of single- and few-layer MoS2," *ACS Nano*, vol. 4, pp. 2695-2700, 2010.

[32] W. Zhao, Z. Ghorannevis, K. Amara, J. Pang, M. Toh, X. Zhang, *et al.*, "Lattice dynamics in mono- and few-layer sheets of WS2 and WSe2," *Nanoscale,* vol. 5, pp. 9677-9683, 2013.

[33] A. Berkdemir, H. R. Gutiérrez, A. R. Botello-Méndez, N. Perea-López, A. Elías, C.-I. Chia, *et al.*, "Identification of individual and few layers of WS2 using Raman Spectroscopy," *Scientific Reports,* vol. 3, p. 1755, 2013.

[34] A. Kuc and T. Heine, "The electronic structure calculations of two-dimensional transition-metal dichalcogenides in the presence of external electric and magnetic fields," *Chemical Society Reviews,* vol. 44, pp. 2603-2614, 2015.

[35] E. Scalise, M. Houssa, G. Pourtois, and V. V. Afanas, "First-principles study of strained 2D MoS 2," *First-principles study of strained 2D MoS 2,* 2014.

[36] W. Zhao, Z. Ghorannevis, L. Chu, M. Toh, C. Kloc, P.-H. Tan, *et al.*, "Evolution of Electronic Structure in Atomically Thin Sheets of WS2 and WSe2," *ACS Nano,* vol. 7, pp. 791-797, 2013.

[37] G. B. Liu, D. Xiao, Y. Yao, X. Xu, and W. Yao, "Electronic structures and theoretical modelling of two-dimensional group-VIB transition metal dichalcogenides," *Chemical Society Reviews,* vol. 44, pp. 2643-2663, 2015.

[38] A. Steinhoff, J. H. Kim, F. Jahnke, M. Rösner, D. S. Kim, C. Lee, *et al.*, "Efficient Excitonic Photoluminescence in Direct and Indirect Band Gap Monolayer MoS2," *Nano Letters,* vol. 15, pp. 6841-6847, 2015.

[39] C.-H. Chang, X. Fan, S.-H. Lin, and J.-L. Kuo, "Orbital analysis of electronic structure and phonon dispersion in MoS2, MoSe2, WS2, and WSe2 monolayers under strain," *Physical Review B,* vol. 88, p. 195420, 2013.

[40] K. F. Mak, C. Lee, J. Hone, J. Shan, and T. F. Heinz, "Atomically thin MoS2: a new direct-gap semiconductor," *Physical Review Letters,* vol. 105, p. 136805, 2010.

[41] H. P. Komsa and A. V. Krasheninnikov, "Effects of confinement and environment on the electronic structure and exciton binding energy of MoS2 from first principles," *Physical Review B,* vol. 86, 2012.

[42] J. Huang, T. B. Hoang, and M. H. Mikkelsen, "Probing the origin of excitonic states in monolayer WSe2," *Scientific Reports,* vol. 6, p. 22414, 2016.

[43] T. C. Berkelbach, M. S. Hybertsen, and D. R. Reichman, "Theory of neutral and charged excitons in monolayer transition metal dichalcogenides," *Physical Review B,* vol. 88, 2013.

[44] K. F. Mak, K. He, C. Lee, G. H. Lee, J. Hone, T. F. Heinz, *et al.*, "Tightly bound trions in monolayer MoS2," *Nature Materials,* vol. 12, pp. 207-211, 2013.

[45] S. Mouri, Y. Miyauchi, and K. Matsuda, "Tunable Photoluminescence of Monolayer MoS2 via Chemical Doping," *Nano Letters,* 2013.

[46] M. Buscema, G. A. Steele, H. S. J. van der Zant, and A. Castellanos-Gomez, "The effect of the substrate on the Raman and photoluminescence emission of single-layer MoS2," *Nano Research,* vol. 7, pp. 561-571, 2014.

[47] J. S. Ross, S. Wu, H. Yu, N. J. Ghimire, A. M. Jones, G. Aivazian, *et al.*, "Electrical control of neutral and charged excitons in a monolayer semiconductor," *Nature Communications,* vol. 4, p. 1474, 2013.

[48] H. Conley, B. Wang, J. Ziegler, R. Haglund, S. Pantelides, and K. Bolotin, "Bandgap engineering of strained monolayer and bilayer MoS2," *Nano Letters,* vol. 13, pp. 3626-3630, 2013.

[49] Z. Liu, M. Amani, S. Najmaei, Q. Xu, X. Zou, W. Zhou*, et al.*, "Strain and structure heterogeneity in MoS2 atomic layers grown by chemical vapour deposition," *Nature Communications,* vol. 5, p. 5246, 2014.

[50] L. F. Mattheiss, "Band Structures of Transition-Metal-Dichalcogenide Layer Compounds," *Physical Review B,* vol. 8, pp. 3719-3740, 1973.

[51] Y. Yoon, K. Ganapathi, and S. Salahuddin, "How good can monolayer MoS2 transistors be?," *Nano Letters,* vol. 11, pp. 3768-3773, 2011.

[52] L. T. Liu, S. B. Kumar, Y. Ouyang, and J. Guo, "Performance Limits of Monolayer Transition Metal Dichalcogenide Transistors," *IEEE Transactions on Electron Devices,* vol. 58, pp. 3042-3047, 2011.

[53] J. Zheng, X. Yan, Z. Lu, H. Qiu, G. Xu, X. Zhou*, et al.*, "High-Mobility Multilayered MoS2 Flakes with Low Contact Resistance Grown by Chemical Vapor Deposition," *Advanced Materials,* vol. 29, p. 1604540, 2017.

[54] S. Das, H. Y. Chen, A. V. Penumatcha, and J. Appenzeller, "High performance multilayer MoS2 transistors with scandium contacts," *Nano Letters,* vol. 13, pp. 100-105, 2013.

[55] H. Liu, M. Si, Y. Deng, A. T. Neal, Y. Du, S. Najmaei*, et al.*, "Switching mechanism in single-layer molybdenum disulfide transistors: an insight into current flow across Schottky barriers," *ACS Nano,* vol. 8, pp. 1031-1038, 2014.

[56] J. Wang, Q. Yao, C. W. Huang, X. Zou, L. Liao, S. Chen*, et al.*, "High Mobility MoS2 Transistor with Low Schottky Barrier Contact by Using Atomic Thick h-BN as a Tunneling Layer," *Advanced Materials,* vol. 28, pp. 8302-8308, 2016.

[57] S. McDonnell, R. Addou, C. Buie, R. M. Wallace, and C. L. Hinkle, "Defect-dominated doping and contact resistance in MoS2," *ACS nano,* vol. 8, pp. 2880-2888, 2014.

[58] X. Tong, E. Ashalley, F. Lin, H. Li, and Z. M. Wang, "Advances in MoS2-Based Field Effect Transistors (FETs)," *Nano-Micro Letters,* 2015.

[59] F. Withers, T. H. Bointon, D. C. Hudson, M. F. Craciun, and S. Russo, "Electron transport of WS2 transistors in a hexagonal boron nitride dielectric environment," *Scientific Reports,* vol. 4, p. 4967, 2014.

[60] Y. Illarionov, G. Rzepa, M. Waltl, T. Knobloch, A. Grill, M. M. Furchi*, et al.*, "The role of charge trapping in MoS2/SiO2 and MoS2/hBN field-effect transistors," *2D Materials,* vol. 3, p. 35004, 2016.

[61] J. Shu, G. Wu, Y. Guo, B. Liu, X. Wei, and Q. Chen, "The intrinsic origin of hysteresis in MoS2 field effect transistors," *Nanoscale,* vol. 8, pp. 3049-3056, 2016.

[62] M. Chen, H. Nam, S. Wi, G. Priessnitz, I. M. Gunawan, and X. Liang, "Multibit data storage states formed in plasma-treated MoS_2 transistors," *ACS nano,* vol. 8, pp. 4023-4032, 2014.

[63] D. J. Late, B. Liu, H. S. Matte, V. P. Dravid, and C. N. Rao, "Hysteresis in single-layer MoS2 field effect transistors," *ACS Nano,* vol. 6, pp. 5635-5641, 2012.

[64] D. Jariwala, V. K. Sangwan, L. J. Lauhon, T. J. Marks, and M. C. Hersam, "Emerging device applications for semiconducting two-dimensional transition metal dichalcogenides," *ACS Nano,* vol. 8, pp. 1102-1120, 2014.

[65] M. M. Furchi, D. K. Polyushkin, A. Pospischil, and T. Mueller, "Mechanisms of photoconductivity in atomically thin MoS2," *Nano Letters,* vol. 14, pp. 6165-6170, 2014.

[66] M. Buscema, M. Barkelid, V. Zwiller, H. S. van der Zant, G. A. Steele, and A. Castellanos-Gomez, "Large and tunable photothermoelectric effect in single-layer MoS2," *Nano Letters,* vol. 13, pp. 358-363, 2013.

[67] M. Fontana, T. Deppe, A. K. Boyd, M. Rinzan, A. Y. Liu, M. Paranjape, *et al.*, "Electron-hole transport and photovoltaic effect in gated MoS2 Schottky junctions," *Scientific Reports,* vol. 3, p. 1634, 2013.

[68] G. Konstantatos and E. H. Sargent, "Nanostructured materials for photon detection," *Nature Nanotechnology,* vol. 5, pp. 391-400, 2010.

[69] V. Klee, E. Preciado, D. Barroso, A. E. Nguyen, C. Lee, K. J. Erickson, *et al.*, "Superlinear composition-dependent photocurrent in CVD-grown monolayer MoS2(1-x)Se2x alloy devices," *Nano Letters,* vol. 15, pp. 2612-2619, 2015.

[70] X. Xu, N. M. Gabor, J. S. Alden, A. M. van der Zande, and P. L. McEuen, "Photo-Thermoelectric Effect at a Graphene Interface Junction," *Nano Letters,* vol. 10, pp. 562-566, 2010.

[71] O. Lopez-Sanchez, D. Lembke, M. Kayci, A. Radenovic, and A. Kis, "Ultrasensitive photodetectors based on monolayer MoS2," *Nature Nanotechnology,* vol. 8, pp. 497-501, 2013.

[72] W. Choi, M. Y. Cho, A. Konar, J. H. Lee, G. B. Cha, S. C. Hong, *et al.*, "High-detectivity multilayer MoS(2) phototransistors with spectral response from ultraviolet to infrared," *Advanced Materials,* vol. 24, pp. 5832-5836, 2012.

[73] D. Kufer and G. Konstantatos, "Highly Sensitive, Encapsulated MoS2 Photodetector with Gate Controllable Gain and Speed," *Nano Letters,* vol. 15, pp. 7307-7313, 2015.

[74] D. Zhou, H. Shu, C. Hu, L. Jiang, P. Liang, and X. Chen, "Unveiling the Growth Mechanism of MoS2 with Chemical Vapor Deposition: From Two-Dimensional Planar Nucleation to Self-Seeding Nucleation," *Crystal Growth & Design,* vol. 18, pp. 1012-1019, 2018.

[75] W. Wang, X. Wu, and J. Zhang, "Graphene and Other 2D Material Components Dynamic Characterization and Nanofabrication at Atomic Scale," *Journal of Nanomaterials,* vol. 2015, p. 198126, 2015.

[76] A. M. van der Zande, P. Y. Huang, D. A. Chenet, T. C. Berkelbach, Y. You, G. H. Lee, *et al.*, "Grains and grain boundaries in highly crystalline monolayer molybdenum disulphide," *Nature Materials,* vol. 12, pp. 554-561, 2013.

[77] H. Qiu, T. Xu, Z. Wang, W. Ren, H. Nan, Z. Ni, *et al.*, "Hopping transport through defect-induced localized states in molybdenum disulphide," *Nature Communications,* vol. 4, p. 2642, 2013.

[78] C. Ataca, H. Şahin, E. Aktürk, and S. Ciraci, "Mechanical and Electronic Properties of MoS2 Nanoribbons and Their Defects," *The Journal of Physical Chemistry C,* vol. 115, pp. 3934-3941, 2011.

[79] K. K. Liu, W. Zhang, Y. H. Lee, Y. C. Lin, M. T. Chang, C. Y. Su, *et al.*, "Growth of large-area and highly crystalline MoS2 thin layers on insulating substrates," *Nano Letters,* vol. 12, pp. 1538-1544, 2012.

[80] J. Yang, Y. Gu, E. Lee, H. Lee, S. H. Park, M. H. Cho, *et al.*, "Wafer-scale synthesis of thickness-controllable MoS2 films via solution-processing using a dimethylformamide/n-butylamine/2-aminoethanol solvent system," *Nanoscale,* vol. 7, pp. 9311-9319, 2015.

[81] M. I. Serna, S. H. Yoo, S. Moreno, Y. Xi, J. P. Oviedo, H. Choi, *et al.*, "Large-Area Deposition of MoS2 by Pulsed Laser Deposition With In Situ Thickness Control," *ACS Nano,* vol. 10, pp. 6054-6061, 2016.

[82] C. R. Serrao, A. M. Diamond, S. L. Hsu, L. You, S. Gadgil, J. Clarkson, *et al.*, "Highly crystalline MoS2 thin films grown by pulsed laser deposition," *Applied Physics Letters,* vol. 106, p. 052101, 2015.

[83] M. H. Heyne, D. Chiappe, J. Meersschaut, T. Nuytten, T. Conard, H. Bender, *et al.*, "Multilayer MoS2 growth by metal and metal oxide sulfurization," *Journal of Materials Chemistry C,* vol. 4, pp. 1295-1304, 2016.

[84] C. M. Orofeo, S. Suzuki, Y. Sekine, and H. Hibino, "Scalable synthesis of layer-controlled WS2 and MoS2 sheets by sulfurization of thin metal films," *Applied Physics Letters,* vol. 105, p. 083112 2014.

[85] Y. Rong, Y. Fan, A. Koh, A. W. Robertson, K. He, S. Wang, *et al.*, "Controlling sulphur precursor addition for large single crystal domains of WS 2," *Nanoscale,* vol. 6, pp. 12096-12103, 2014.

[86] Y. Gong, Z. Lin, G. Ye, G. Shi, S. Feng, Y. Lei, *et al.*, "Tellurium-Assisted Low-Temperature Synthesis of MoS2 and WS2 Monolayers," *ACS nano,* vol. 9, pp. 11658-11666, 2015.

[87] S. Najmaei, Z. Liu, W. Zhou, X. Zou, G. Shi, S. Lei, *et al.*, "Vapour phase growth and grain boundary structure of molybdenum disulphide atomic layers," *Nature Materials,* vol. 12, pp. 754-759, 2013.

[88] I. Bilgin, F. Z. Liu, A. Vargas, A. Winchester, M. K. L. Man, M. Upmanyu, *et al.*, "Chemical Vapor Deposition Synthesized Atomically Thin Molybdenum Disulfide with Optoelectronic-Grade Crystalline Quality," *ACS Nano,* vol. 9, pp. 8822-8832, 2015.

[89] S. S. Wang, Y. M. Rong, Y. Fan, M. Pacios, H. Bhaskaran, K. He, *et al.*, "Shape Evolution of Monolayer MoS2 Crystals Grown by Chemical Vapor Deposition," *Chemistry of Materials,* vol. 26, pp. 6371-6379, 2014.

[90] J. Y. Chen, W. Tang, B. B. Tian, B. Liu, X. X. Zhao, Y. P. Liu, *et al.*, "Chemical Vapor Deposition of High-Quality Large-Sized MoS2 Crystals on Silicon Dioxide Substrates," *Advanced Science,* vol. 3, p. 1600033, 2016.

[91] D. Dumcenco, D. Ovchinnikov, K. Marinov, P. Lazić, M. Gibertini, N. Marzari, *et al.*, "Large-Area Epitaxial Monolayer MoS2," *ACS Nano,* vol. 9, pp. 4611-4620, 2015.

[92] N. M. Hwang and D. Y. Yoon, "Thermodynamic approach to the chemical vapor deposition process," *Journal of Crystal Growth,* vol. 143, pp. 103-109, 1994.

[93] M. P. Moody and P. Attard, "Homogeneous nucleation of droplets from a supersaturated vapor phase," *Journal of Chemical Physics,* vol. 117, pp. 6705-6714, 2002.

[94] S. Xie, M. Xu, T. Liang, G. Huang, S. Wang, G. Xue, *et al.*, "A high-quality round-shaped monolayer MoS2 domain and its transformation," *Nanoscale,* vol. 8, pp. 219-225, 2015.

[95] Y. Xie, Z. Wang, Y. Zhan, P. Zhang, R. Wu, T. Jiang, *et al.*, "Controllable growth of monolayer MoS2 by chemical vapor deposition via close MoO2 precursor for electrical and optical applications," *Nanotechnology,* vol. 28, p. 084001, 2017.

[96] J. Lee, S. Pak, P. Giraud, Y.-W. Lee, Y. Cho, J. Hong, *et al.*, "Thermodynamically Stable Synthesis of Large-Scale and Highly Crystalline Transition Metal Dichalcogenide Monolayers and their Unipolar n-n Heterojunction Devices," *Advanced Materials,* vol. 29, p. 1702206, 2017.

[97] D. Sercombe, S. Schwarz, O. Del Pozo-Zamudio, F. Liu, B. J. Robinson, E. A. Chekhovich, *et al.*, "Optical investigation of the natural electron doping in thin MoS2 films deposited on dielectric substrates," *Scientific Reports,* vol. 3, p. 3489, 2013.

[98] Y. Gong, J. Lin, X. Wang, G. Shi, S. Lei, Z. Lin, *et al.*, "Vertical and in-plane heterostructures from WS2/MoS2 monolayers," *Nature Materials,* vol. 13, pp. 1135-1142, 2014.

[99] X.-Q. Zhang, C.-H. Lin, Y.-W. Tseng, K.-H. Huang, and Y.-H. Lee, "Synthesis of Lateral Heterostructures of Semiconducting Atomic Layers," *Nano Letters,* vol. 15, pp. 410-415, 2015.

[100] K. Chen, X. Wan, W. Xie, J. Wen, Z. Kang, X. Zeng, *et al.*, "Lateral Built-In Potential of Monolayer MoS2–WS2 In-Plane Heterostructures by a Shortcut Growth Strategy," *Advanced Materials,* vol. 27, pp. 6431-6437, 2015.

[101] H. Heo, J. H. Sung, G. Jin, J. H. Ahn, K. Kim, M. J. Lee, *et al.*, "Rotation-misfit-free heteroepitaxial stacking and stitching growth of hexagonal transition-metal dichalcogenide monolayers by nucleation kinetics controls," *Advanced Materials,* vol. 27, pp. 3803-3810, 2015.

[102] K. Bogaert, S. Liu, J. Chesin, D. Titow, S. Gradečak, and S. Garaj, "Diffusion-Mediated Synthesis of MoS2/WS2 Lateral Heterostructures," *Nano Letters,* vol. 16, pp. 5129-5134, 2016.

[103] Y. Gong, S. Lei, G. Ye, B. Li, Y. He, K. Keyshar, *et al.*, "Two-Step Growth of Two-Dimensional WSe2/MoSe2 Heterostructures," *Nano Letters,* vol. 15, pp. 6135-6141, 2015.

[104] M.-Y. Li, Y. Shi, C.-C. Cheng, L.-S. Lu, Y.-C. Lin, H.-L. Tang, *et al.*, "Epitaxial growth of a monolayer WSe2-MoS2 lateral p-n junction with an atomically sharp interface," *Science,* vol. 349, pp. 524-528, 2015.

[105] G. H. Han, N. J. Kybert, C. H. Naylor, B. S. Lee, J. Ping, J. H. Park, *et al.*, "Seeded growth of highly crystalline molybdenum disulphide monolayers at controlled locations," *Nature Communications,* vol. 6, p. 6128, 2015.

[106] S. Bertolazzi, J. Brivio, and A. Kis, "Stretching and Breaking of Ultrathin MoS2," *ACS Nano,* vol. 5, pp. 9703-9709, 2011.

[107] D. Lloyd, X. Liu, J. W. Christopher, L. Cantley, A. Wadehra, B. L. Kim, *et al.*, "Band Gap Engineering with Ultralarge Biaxial Strains in Suspended Monolayer MoS2," *Nano Letters,* vol. 16, pp. 5836-5841, 2016.

[108] S. Najmaei, X. Zou, D. Er, J. Li, Z. Jin, W. Gao, *et al.*, "Tailoring the Physical Properties of Molybdenum Disulfide Monolayers by Control of Interfacial Chemistry," *Nano Letters,* vol. 14, pp. 1354-1361, 2014.

[109] G. Fiori, F. Bonaccorso, G. Iannaccone, T. Palacios, D. Neumaier, A. Seabaugh, *et al.*, "Electronics based on two-dimensional materials," *Nature Nanotechnology,* vol. 9, pp. 768-779, 2014.

[110] J. Lee, S. Pak, Y.-W. Lee, Y. Cho, J. Hong, P. Giraud, *et al.*, "Monolayer optical memory cells based on artificial trap-mediated charge storage and release," *Nature Communications,* vol. 8, p. 14734, 2017.

[111] K. Cho, M. Min, T.-Y. Y. Kim, H. Jeong, J. Pak, J.-K. K. Kim, *et al.*, "Electrical and Optical Characterization of MoS2 with Sulfur Vacancy Passivation by Treatment with Alkanethiol Molecules," *ACS nano,* vol. 9, pp. 8044-8053, 2015.

[112] J. Hong, B. Hou, J. Lim, S. Pak, B. S. Kim, Y. Cho, *et al.*, "Enhanced charge carrier transport properties in colloidal quantum dot solar cells via organic and inorganic hybrid surface passivation," *J. Mater. Chem. A,* vol. 4, pp. 18769-18775, 2016.

[113] Y. Li, C.-Y. Y. Xu, P. Hu, and L. Zhen, "Carrier control of MoS2 nanoflakes by functional self-assembled monolayers," *ACS nano,* vol. 7, pp. 7795-7804, 2013.

[114] D. H. Kang, M. S. Kim, J. Shim, J. Jeon, H. Y. Park, W. S. Jung, *et al.*, "High-Performance Transition Metal Dichalcogenide Photodetectors Enhanced by Self-Assembled Monolayer Doping," *Advanced Functional Materials,* vol. 25, pp. 4219-4227, 2015.

[115] J. Park, W. H. Lee, S. Huh, S. H. Sim, S. B. Kim, K. Cho, *et al.*, "Work-Function Engineering of Graphene Electrodes by Self-Assembled Monolayers for High-Performance Organic Field-Effect Transistors," *Journal of Physical Chemistry Letters,* vol. 2, pp. 841-845, 2011.

[116] B. Chakraborty, A. Bera, D. V. S. Muthu, S. Bhowmick, U. V. Waghmare, and A. K. Sood, "Symmetry-dependent phonon renormalization in monolayer MoS2 transistor," *Physical Review B,* vol. 85, p. 161403, 2012.

[117] D. Y. Guo, Z. P. Wu, Y. H. An, X. C. Guo, X. L. Chu, C. L. Sun, *et al.*, "Oxygen vacancy tuned Ohmic-Schottky conversion for enhanced performance in beta-Ga2O3 solar-blind ultraviolet photodetectors," *Applied Physics Letters,* vol. 105, p. 023507, 2014.

[118] J. Zhou, Y. Gu, Y. Hu, W. Mai, P. H. Yeh, G. Bao, *et al.*, "Gigantic enhancement in response and reset time of ZnO UV nanosensor by utilizing Schottky contact and surface functionalization," *Applied Physics Letters,* vol. 94, p. 191103, 2009.

[119] N. S. Liu, G. J. Fang, W. Zeng, H. Zhou, F. Cheng, Q. A. Zheng, *et al.*, "Direct Growth of Lateral ZnO Nanorod UV Photodetectors with Schottky Contact by a Single-Step Hydrothermal Reaction," *ACS Applied Materials & Interfaces,* vol. 2, pp. 1973-1979, 2010.

[120] Y.-C. Wu, C.-H. Liu, S.-Y. Chen, F.-Y. Shih, P.-H. Ho, C.-W. Chen, *et al.*, "Extrinsic Origin of Persistent Photoconductivity in Monolayer MoS2 Field Effect Transistors," *Scientific Reports,* vol. 5, p. 11472, 2015.

[121] J. D. Prades, F. Hernandez-Ramirez, R. Jimenez-Diaz, M. Manzanares, T. Andreu, A. Cirera, *et al.*, "The effects of electron-hole separation on the photoconductivity of individual metal oxide nanowires," *Nanotechnology,* vol. 19, p. 465501, 2008.

[122] P. Lu, X. Wu, W. Guo, and X. Zeng, "Strain-dependent electronic and magnetic properties of MoS2 monolayer, bilayer, nanoribbons and nanotubes," *Physical Chemistry Chemical Physics,* vol. 14, pp. 13035-13040, 2012.

[123] B. Amin, T. P. Kaloni, and U. Schwingenschlögl, "Strain engineering of WS2 , WSe2 , and WTe2," *RSC Advances,* vol. 4, pp. 34561-34565, 2014.

[124] S. Tongay, J. Zhou, C. Ataca, K. Lo, T. S. Matthews, J. Li, *et al.*, "Thermally driven crossover from indirect toward direct bandgap in 2D semiconductors: MoSe2 versus MoS2," *Nano Letters,* vol. 12, pp. 5576-5580, 2012.

[125] S. B. Desai, G. Seol, J. Kang, H. Fang, C. Battaglia, R. Kapadia, *et al.*, "Strain-Induced Indirect to Direct Bandgap Transition in Multilayer WSe2," *Nano Letters,* vol. 14, pp. 4592-4597, 2014.

[126] Y. Hui, X. Liu, W. Jie, N. Chan, J. Hao, Y.-T. Hsu, *et al.*, "Exceptional Tunability of Band Energy in a Compressively Strained Trilayer MoS2 Sheet," *ACS Nano,* vol. 7, pp. 7126-7131, 2013.

[127] K. He, C. Poole, K. Mak, and J. Shan, "Experimental Demonstration of Continuous Electronic Structure Tuning via Strain in Atomically Thin MoS2," *Nano Letters,* vol. 13, pp. 2931-2936, 2013.

[128] Y. Wang, C. Cong, W. Yang, J. Shang, N. Peimyoo, Y. Chen, *et al.*, "Strain-induced direct–indirect bandgap transition and phonon modulation in monolayer WS2," *Nano Res.,* vol. 8, pp. 2562-2572, 2015.

[129] A. K. Geim and I. V. Grigorieva, "Van der Waals heterostructures," *Nature,* vol. 499, pp. 419-425, 2013.

[130] N. Mori and T. Ando, "Electron-optical-phonon interaction in single and double heterostructures," *Physical Review B,* vol. 40, pp. 6175-6188, 1989.

[131] M. C. Scharber, D. Mühlbacher, M. Koppe, P. Denk, C. Waldauf, A. J. Heeger, *et al.*, "Design Rules for Donors in Bulk-Heterojunction Solar Cells—Towards 10 % Energy-Conversion Efficiency," *Advanced Materials,* vol. 18, pp. 789-794, 2006.

[132] H. Kroemer, "Heterostructure bipolar transistors and integrated circuits," *Proceedings of the IEEE,* vol. 70, pp. 13-25, 1982.

[133] B.-S. Kim, D. C. J. Neo, B. Hou, J. Park, Y. Cho, N. Zhang, *et al.*, "High Performance PbS Quantum Dot/Graphene Hybrid Solar Cell with Efficient Charge Extraction," *ACS Applied Materials & Interfaces,* vol. 8, pp. 13902-13908, 2016.

[134] T. Mimura, S. Hiyamizu, and T. Fujii, "A new field-effect transistor with selectively doped GaAs/n-AlxGa1-xAs heterojunctions," *Japanese journal of Applied Physics,* vol. 19, pp. 225-227, 1980.

[135] Z. I. Alferov, "The history and future of semiconductor heterostructures," *Semiconductors,* vol. 32, pp. 1-14, 1998.

[136] F. Schwierz, "Graphene transistors," *Nature Nanotechnology,* vol. 5, pp. 487-496, 2010.

[137] A. R. Jang, S. Hong, C. Hyun, S. Yoon, G. Kim, H. Jeong, *et al.*, "Wafer-Scale and Wrinkle-Free Epitaxial Growth of Single-Orientated Multilayer Hexagonal Boron Nitride on Sapphire," *Nano Letters,* vol. 16, pp. 3360-3366, 2016.

[138] C. R. Dean, A. F. Young, I. Meric, C. Lee, L. Wang, S. Sorgenfrei, *et al.*, "Boron nitride substrates for high-quality graphene electronics," *Nature Nanotechnology,* vol. 5, pp. 722-726, 2010.

[139] G. Kim, A. R. Jang, H. Jeong, Z. Lee, D. Kang, and H. Shin, "Growth of high-crystalline, single-layer hexagonal boron nitride on recyclable platinum foil," *Nano LEtters,* vol. 13, pp. 1834-1839, 2013.

[140] X. Duan, C. Wang, A. Pan, R. Yu, and X. Duan, "Two-dimensional transition metal dichalcogenides as atomically thin semiconductors: opportunities and challenges," *Chemical Society Reviews,* vol. 44, pp. 8859-8876, 2015.

[141] Y. Xue, Y. Zhang, Y. Liu, H. Liu, J. Song, J. Sophia*, et al.*, "Scalable Production of a Few-Layer MoS2/WS2 Vertical Heterojunction Array and Its Application for Photodetectors," *ACS Nano,* vol. 10, pp. 573-580, 2016.

[142] J. Zhang, J. Wang, P. Chen, Y. Sun, S. Wu, Z. Jia*, et al.*, "Observation of Strong Interlayer Coupling in MoS2/WS2 Heterostructures," *Advanced Materials,* vol. 28, pp. 1950-1956, 2016.

[143] M.-H. Chiu, C. Zhang, H.-W. Shiu, C.-P. Chuu, C.-H. Chen, C.-Y. S. Chang*, et al.*, "Determination of band alignment in the single-layer MoS2/WSe2 heterojunction," *Nature Communications,* vol. 6, p. 7666, 2015.

[144] H. Fang, C. Battaglia, C. Carraro, S. Nemsak, B. Ozdol, J. Kang*, et al.*, "Strong interlayer coupling in van der Waals heterostructures built from single-layer chalcogenides," *Proceedings of the National Academy of Sciences of the United States of America,* vol. 111, pp. 6198-6202, 2014.

[145] R. Cheng, D. Li, H. Zhou, C. Wang, A. Yin, S. Jiang*, et al.*, "Electroluminescence and Photocurrent Generation from Atomically Sharp WSe2/MoS2 Heterojunction p–n Diodes," *Nano Letters,* vol. 14, pp. 5590-5597, 2014.

[146] Y. He, Y. Yang, Z. Zhang, Y. Gong, W. Zhou, Z. Hu*, et al.*, "Strain-Induced Electronic Structure Changes in Stacked van der Waals Heterostructures," *Nano Letters,* vol. 16, pp. 3314-3320, 2016.

[147] X. Duan, C. Wang, J. C. Shaw, R. Cheng, Y. Chen, H. Li*, et al.*, "Lateral epitaxial growth of two-dimensional layered semiconductor heterojunctions," *Nature Nanotechnology,* vol. 9, pp. 1024-1030, 2014.

[148] K. Roy, M. Padmanabhan, S. Goswami, P. T. Sai, G. Ramalingam, S. Raghavan*, et al.*, "Graphene-MoS2 hybrid structures for multifunctional photoresponsive memory devices," *Nature Nanotechnology,* vol. 8, pp. 826-830, 2013.

[149] H. Peelaers and V. C. G. de Walle, "Effects of strain on band structure and effective masses in MoS2," *Physical Review B,* vol. 86, 2012.

[150] M. Xia, B. Li, K. Yin, G. Capellini, G. Niu, Y. Gong*, et al.*, "Spectroscopic Signatures of AA' and AB Stacking of Chemical Vapor Deposited Bilayer MoS2," *ACS Nano,* vol. 9, pp. 12246-12254, 2015.

[151] K. Liu, L. Zhang, T. Cao, C. Jin, D. Qiu, Q. Zhou*, et al.*, "Evolution of interlayer coupling in twisted molybdenum disulfide bilayers," *Nature Communications,* vol. 5, p. 4966, 2014.

[152] F. Wang, I. A. Kinloch, D. Wolverson, R. Tenne, A. Zak, E. O'Connell*, et al.*, "Strain-induced phonon shifts in tungsten disulfide nanoplatelets and nanotubes," *2D Materials,* vol. 4, p. 15007, 2016.

[153] E. M. Alexeev, A. Catanzaro, O. Skrypka, P. Nayak, S. Ahn, S. Pak*, et al.*, "Imaging of interlayer coupling in van der Waals heterostructures using a bright-field optical microscope," *Nano Letters,* vol. DOI: 10.1021/acs.nanolett.7b01763, 2017.

[154] B. R. Carvalho, L. M. Malard, J. M. Alves, C. Fantini, and M. A. Pimenta, "Symmetry-dependent exciton-phonon coupling in 2D and bulk MoS2 observed by resonance Raman scattering," *Physical Review Letters,* vol. 114, p. 136403, 2015.

[155] A. P. S. Gaur, S. Sahoo, J. F. Scott, and R. S. Katiyar, "Electron–Phonon Interaction and Double-Resonance Raman Studies in Monolayer WS2," *The Journal of Physical Chemistry C,* vol. 119, pp. 5146-5151, 2015.

[156] G. Konstantatos, M. Badioli, L. Gaudreau, J. Osmond, M. Bernechea, G. F. P. de Arquer, *et al.*, "Hybrid graphene-quantum dot phototransistors with ultrahigh gain," *Nature nanotechnology,* vol. 7, pp. 363-368, 2012.

[157] X. Chen, X. Liu, B. Wu, H. Nan, H. Guo, Z. Ni, *et al.*, "Improving the Performance of Graphene Phototransistors Using a Heterostructure as the Light-Absorbing Layer," *Nano Letters,* vol. 17, pp. 6391-6396, 2017.

[158] I. Nikitskiy, S. Goossens, D. Kufer, T. Lasanta, G. Navickaite, F. H. Koppens, *et al.*, "Integrating an electrically active colloidal quantum dot photodiode with a graphene phototransistor," *Nature Communications,* vol. 7, p. 11954, 2016.

[159] D. Kufer, T. Lasanta, M. Bernechea, F. H. L. Koppens, and G. Konstantatos, "Interface Engineering in Hybrid Quantum Dot–2D Phototransistors," *ACS Photonics,* vol. 3, pp. 1324-1330, 2016.

[160] D. Kufer, I. Nikitskiy, T. Lasanta, G. Navickaite, F. H. Koppens, and G. Konstantatos, "Hybrid 2D-0D MoS2 -PbS quantum dot photodetectors," *Advanced Materials,* vol. 27, pp. 176-180, 2015.

[161] N. Huo, S. Gupta, and G. Konstantatos, "MoS_2–HgTe Quantum Dot Hybrid Photodetectors beyond 2 µm," *Advanced Materials,* vol. 29, p. 1606576, 2017.

[162] C.-H. M. H. Chuang, P. R. Brown, V. Bulović, and M. G. Bawendi, "Improved performance and stability in quantum dot solar cells through band alignment engineering," *Nature Materials,* vol. 13, pp. 796-801, 2014.

[163] B. Hou, Y. Cho, B. S. Kim, J. Hong, J. B. Park, S. J. Ahn, *et al.*, "Highly Monodispersed PbS Quantum Dots for Outstanding Cascaded-Junction Solar Cells," *ACS Energy Letters,* vol. 1, pp. 834-839, 2016.

[164] Y. Cho, B. Hou, J. Lim, S. Lee, S. Pak, J. Hong, *et al.*, "Balancing Charge Carrier Transport in a Quantum Dot P-N Junction toward Hysteresis-Free High-Performance Solar Cells," *ACS Energy Letters,* vol. 3, pp. 1036-1043, 2018.

[165] P. H. Rekemeyer, C. H. M. Chuang, M. G. Bawendi, and S. Gradecak, "Minority Carrier Transport in Lead Sulfide Quantum Dot Photovoltaics," *Nano Letters,* vol. 17, pp. 6221-6227, 2017.

[166] Z. Ren, J. Sun, H. Li, P. Mao, Y. Wei, X. Zhong, *et al.*, "Bilayer PbS Quantum Dots for High-Performance Photodetectors," *Advanced Materials,* vol. 29, p. 1702055, 2017.

[167] J. P. Clifford, G. Konstantatos, K. W. Johnston, S. Hoogland, L. Levina, and E. H. Sargent, "Fast, sensitive and spectrally tuneable colloidal-quantum-dot photodetectors," *Nature Nanotechnology,* vol. 4, pp. 40-44, 2008.

[168] W. Zhang, M. H. Chiu, C. H. Chen, W. Chen, L. J. Li, and A. T. S. Wee, "Role of Metal Contacts in High-Performance Phototransistors Based on WSe2 Monolayers," *ACS Nano,* vol. 8, pp. 8653-8661, 2014.

[169] D. De Fazio, I. Goykhman, D. Yoon, M. Bruna, A. Eiden, S. Milana, *et al.*, "High Responsivity, Large-Area Graphene/MoS2 Flexible Photodetectors," *ACS Nano,* vol. 10, pp. 8252-8262, 2016.

[170] G. H. Lee, Y. J. Yu, X. Cui, N. Petrone, C. H. Lee, M. S. Choi, *et al.*, "Flexible and transparent MoS2 field-effect transistors on hexagonal boron nitride-graphene heterostructures," *ACS Nano,* vol. 7, pp. 7931-7936, 2013.

[171] H. Y. Chang, S. Yang, J. Lee, L. Tao, W. S. Hwang, D. Jena, *et al.*, "High-performance, highly bendable MoS2 transistors with high-k dielectrics for flexible low-power systems," *ACS Nano,* vol. 7, pp. 5446-5452, 2013.

[172] J. Pu, Y. Yomogida, K.-K. K. Liu, L.-J. J. Li, Y. Iwasa, and T. Takenobu, "Highly flexible MoS2 thin-film transistors with ion gel dielectrics," *Nano Letters,* vol. 12, pp. 4013-4017, 2012.

[173] Y. Cho, P. Giraud, B. Hou, Y.-W. Lee, J. Hong, S. Lee, *et al.*, "Charge Transport Modulation of a Flexible Quantum Dot Solar Cell Using a Piezoelectric Effect," *Advanced Energy Materials,* vol. 8, p. 1700809, 2017.

[174] E. Scalise, M. Houssa, G. Pourtois, V. Afanas’ev, and A. Stesmans, "Strain-induced semiconductor to metal transition in the two-dimensional honeycomb structure of MoS2," *Nano Research,* vol. 5, pp. 43-48, 2012.

List of publications & presentation

Thesis publications

Chapter 4

1) J. Lee, **S. Pak**, P. Giraud, Y. -W. Lee, Y. Cho, J. Hong, A. -R. Jang, H. -S. Chung, H. Y. Jeong, H. S. Shin, L. G. Occhipinti, S. M. Morris, S. Cha*, J. I. Sohn*, J. M. Kim, **“**Thermodynamically Stable Synthesis of Large-Scale and Highly-Crystalline Transition Metal Dichalcogenide Monolayers and Their Unipolar n-n Heterojunction Devices", ***Advanced Materials*** 2017, 29, 1702206. (**Front Cover**)

Chapter 5

2) **S. Pak**,[†] A. -R. Jang,[†] J. Lee, J. Hong, Y. -W. Lee, Y. Cho, P. Giraud, S. Lee, H. S. Shin, S. M. Morris, S. Cha,* J. I. Sohn,* J. M. Kim, “Surface functionalization-induced photoresponse characteristics of monolayer MoS_2 for fast flexible photodetectors”, ***Nanoscale*** (under revision).

Chapter 6

3) **S. Pak**, J. Lee, Y. -W. Lee, A. -R. Jang, S. Ahn, K. Y. Ma, Y. Cho, J. Hong, S. Lee, H. Y. Jeong, H. Im, H. S. Shin, S. M. Morris, S. Cha*, J. I. Sohn*, J. M. Kim, "Strain-mediated interlayer coupling effects on the excitonic behaviors in an epitaxially-grown MoS_2/WS_2 van der Waals heterobilayer", ***Nano Letters*** 2017, 17, 5634-5640.

Chapter 7

4) **S. Pak**,[†] Y. Cho,[†] J. Hong, J. Lee, S. Lee, B. Hou, G. -H. An, Y. -W. Lee, J. E. Jang, H. Im, S. M. Morris, J. I. Sohn,* S. Cha,* J. M. Kim, “High-Performance MoS_2/Quantum Dot Hybrid Phototransistors through Engineered Band Alignment”, ***ACS Applied Materials & Interfaces*** 2018, 10, 38264-38271. (**Front Cover**)

Other Publications

5) B. Kim,*[, †] **S. Pak,**[†] H. W. Choi, Y. Choi, A. -R. Jang , J. Lee, Y. T. Chun, S. Cha, J. I. Sohn,* “Complementary Inverters Based on Low-Dimensional Semiconductors Prepared by Scalable Methods”, ***2D Materials*** 2018, 6, 025017.

6) J. Lee, **S. Pak,** Y. -W. Lee, J. Hong, P. Giraud, H. S. Shin, S. M. Morris, J. I. Sohn*, S. Cha*, J. M. Kim, “Monolayer Optical Memory Cells based on Artificial Trap-Mediated Charge Storage and Release”, ***Nature Communications*** 2017, 8, 14734.

[†] Equally Contributed

7) J. Lee, **S. Pak**, Y. -W. Lee, Y. Park, A. -R. Jang, J. Hong, Y. Cho, B. Hou, S. Lee, H. Y. Jeong, H. S. Shin, S. M. Morris, S. Cha,* J. I. Sohn,* J. M. Kim, “One-pot controlled synthesis of lateral MoS2/WS2 heterostructured and alloyed monolayers”, (submitted).

8) E, M. Alexeev, A. Catanzaro, O. V. Skrypka, P. K. Nayak, S. Ahn, **S. Pak**, J. Lee, J. I. Sohn, K. S. Novoselov, H. S. Shin, A. I. Tartakovskii,* “Imaging of Interlayer Coupling in van der Waals Heterostructures Using a Bright-Field Optical Microscope”, ***Nano Letters*** 2017, 17, 5342-5349.

9) E. M. Alexeev, D. A. Ruiz-Tijerina, M. Danovich, P. K. Nayak, S. Ahn, **S. Pak**, J. Lee, J. I. Sohn, K. S. Novoselov, H. S. Shin, V. I. Fal’ko, A. I. Tartakovskii,* “Exciton hybridization in twisted two-dimensional van der Waals heterostructures”, ***Nature*** (Accepted).

10) Y. Cho, P. Giraud, B. Hou, Y. -W. Lee, J. Hong, S. Lee, **S. Pak**, J. Lee, J. E. Jang, S. M. Morris, J. I. Sohn*, S. Cha*, and J. M. Kim, "Charge Transport Modulation of a Flexible Quantum Dot Solar Cell using a Piezoelectric Effect", ***Advanced Energy Materials*** 2018, 8, 1700809.

11) Y. Cho,† S. Lee,† J. Hong, **S. Pak**, B. Hou, Y. -W. Lee, J. E. Jang, H. Im, J. I. Sohn,* S. Cha,* J. M. Kim, “Sustainable hybrid energy harvester based on air stable quantum dot solar cells and triboelectric generator”, ***Journal of Material Chemistry A*** 2018, 6, 12440-12446.

12) Y. Cho, B. Hou, J. Lim, S. Lee, **S. Pak**, J. Hong, P. Giraud, A. -R. Jang, Y. -W. Lee, J. Lee, J. E. Jang, H. J. Snaith, S. M. Morris, J. I. Sohn,* S. Cha,* J. M. Kim, "Balancing Charge Carrier Transport in a Quantum Dot P-N Junction toward Hysteresis-Free High Performance Solar Cells", ***ACS Energy Letters*** 2018, 3, 1036-1043.

13) A. -R. Jang, Y. -W. Lee, S. -S. Lee, J. Hong, S.-H. Beak, **S. Pak**, J. Lee, H. S. Shin, D. Ahn, W. -K. Hong, S. Cha, J. I. Sohn,* and I. -K. Park*, “Electrochemical and electrocatalytic reaction characteristics of boron-incorporated graphene via a simple spin-on dopant process”, ***Journal of Material Chemistry A*** 2018, 6, 7351-7356.

14) P. Giraud, B. Hou, **S. Pak**, J. I. Sohn, S. M. Morris, S. Cha, J. M. Kim, “Field effect transistors and phototransistors based upon p-type solution-processed PbS nanowires”, ***Nanotechnology*** 2018, 29, 075202.

15) Y. -W. Lee,† J. Hong,† G. -H. An, **S. Pak**, J. Lee, Y. Cho, S. Lee, S. Cha,* J. I. Sohn,* J. M. Kim, “Synergetic Effects of Engineered Spinel Hetero-Metallic Cobaltities on Electrochemical Pseudo-Capacitive Behaviors”, ***Journal of Material Chemistry A*** 2018, 6, 15033-15039.

16) J. Hong,† Y. -W. Lee,† D. Ahn, **S. Pak**, J. Lee, A. -R. Jang, S. Lee, B. Hou, Y. Cho, S. M. Morris, H. S. Shin*, S. Cha, J. I. Sohn*, J. M. Kim, "Highly Stable 3D Porous Heterostructures with Hierarchically-Coordinated Octahedral Transition Metals for Enhanced Performance Supercapacitors", ***Nano Energy*** 2017, 39, 337-345.

17) Y. -W. Lee, B. -S. Kim, J. Hong, H. Choi, H. -S. Jang, B. Hou, **S. Pak**, J. Lee, S. Lee, S. M. Morris, D. Whang, J. Hong, H. S. Shin, S. Cha*, J. I. Sohn*, J. M. Kim, “Hierarchically Assembled Tubular Shell-Core-Shell Heterostructure of Hybrid Transition Metal Chalcogenides for High-Performance Supercapacitors with Ultrahigh Cyclability”, ***Nano Energy*** 2017, 37, 15-23.

18) J. Hong, Y. -W. Lee, B. Hou, W. Ko, J. Lee, **S. Pak**, J. Hong, S. M. Morris, S. Cha*, J. I. Sohn*, J. M. Kim, “Solubility-Dependent $NiMoO_4$ Nanoarchitectures: Direct Correlation between Rationally Designed Structure and Electrochemical Pseudo-Kinetics”**, *ACS Applied Materials & Interfaces*** 2016, 8 (51), 35227-35234.

19) J. Hong, B. Hou, J. Lim, **S. Pak,** B. -S. Kim, Y. Cho, J. Lee, Y. -W. Lee, P. Giraud, S. Lee, J. B. Park, S. M. Morris, H. J. Snaith, J. I. Sohn*, S. Cha*, J. M. Kim, “Enhanced Charge Carrier Transport Properties in Colloidal Quantum Dots Solar Cells via Organic and Inorganic Hybrid Surface Passivation”, ***Journal of Material Chemistry A*** 2016, 4 (48), 18769-18775. **(*Back Cover*)**

20) Y. Cho, D. Ahn, J. B. Park**, S. Pak**, S. Lee, B. O. Jun, J. Hong, S. Y. Lee, J. E. Jang, J. Hong, S. M. Morris, J. I. Sohn*, S. Cha*, and J. M. Kim, “Enhanced ferroelectric property of P(VDF-TrFE-CTFE) film using room temperature crystallisation for high performance ferroelectric device applications”, ***Advanced Electronic Materials*** 2016, 2, 1600225 (**Front Cover**).

21) Y. -W. Lee,† G. -H. An,† B. -S. Kim, J. Hong, **S. Pak**, E. -H. Lee, Y. Cho, J. Lee, P. Giraud, S. Cha, H.-J. Ahn,* J. I. Sohn,* J. M. Kim, “Synergistic Effects of a Multi-Functional Graphene Based Interlayer on Electrochemical Behavior and Structural Stability”, ***ACS Applied Materials & Interfaces*** 2016, 8 (27), 17651-17658.

22) B. -S. Kim, D. C. J. Neo, B. Hou, J. B. Park, Y. Cho, N. Zhang, J. Hong, **S. Pak**, S. Lee, J. I. Sohn, H. E. Assender, A. R. Watt*, S. Cha*, J. M. Kim, "High Performance PbS Quantum Dot/Graphene Hybrid Solar Cell with Efficient Charge Extraction”, ***ACS Applied Materials & Interfaces*** 2016, 8, 13902-13908.

23) Y. -W. Lee,† B. -S. Kim,† J. Hong, J. Lee, **S. Pak**, H. -S. Jang, D. Whang, S. N. Cha,* J. I. Sohn,* J. M. Kim, “A Pseudo-Capacitive Chalcogenide-based Electrode with Dense 1-Dimensional Nanoarrays for Enhanced Energy Density in Asymmetric Supercapacitors”, ***Journal of Material Chemistry A*** 2016, 4 (26), 10084-10090. (***Front Cover & 2016 Hot Paper***)

24) J. Hong, B. -S. Kim, S. -M. Yang, A. -R. Jang, Y. -W. Lee, **S. Pak**, S. Lee, Y. Cho, G. Ahn, D. -W. Kang, H. S. Shin, J. -P. Hong, S. M. Morris, S. Cha,* J. I. Sohn,* J. M. Kim, “Strategic Chalcogenide Solution-Mediated Activation Protocal for Scalable Room-Temperature, and Ultrafast Synthesis of Single-Crystalline 1-D Copper Sulfide”, ***Journal of Material Chemistry A*** 2019, 7 (6), 2529-2535.

25) Y. -W. Lee, J. Hong, J. Lee, W. B. Park, D. Ahn, J. B. Park, **S. Pak**, J. Baik, S. M. Morris, S. Cha, K. -S. Sohn, J. I. Sohn,* J. M. Kim, “Multiple Faradaic charge storing reactions enabled by an Ni-S-O compound system with active binary anions”, (Submitted).

26) J. Hong, B. -S. Kim, B. Hou, Y. Cho, S. Lee, **S. Pak**, S. M. Morris, J. I. Sohn, S. Cha, J. M. Kim, “Harnessing Dual-Plasmonic Effects for High-Performance Quantum Dot Solar Cells”, (Submitted).

Paper Presentation in Conferences

UK Semiconductors 2017 (The University of Sheffield, United Kingdom)

Sangyeon Pak et al. "Monolayer optical memory cells based on artificial trap-mediated charge storage and release"

Sangyeon Pak et al**.** "Strain-dependent coupled photoluminescence behaviors in epitaxially-grown MoS_2-WS_2 van der Waals heterobilayers"

EKC 2017 (Stockholm, Sweden)

Sangyeon Pak et al. "2D layered materials for future flexible optoelectronic nanodevices" (Best Poster Award)

Oxford Photonics Day 2018 (Oxford, United Kingdom)

Sangyeon Pak et al. "Strain effects on the excitonic behaviors in an epitaxially-grown van der Waals heterobilayer"